CO_2 Cooling Studies for the ATLAS Upgrade

Author:
Gijs Heemink, BSc
Univ. of Twente/NIKHEF
Faculty of Science and Technology
Applied Physics, ATLAS group

Internship at:

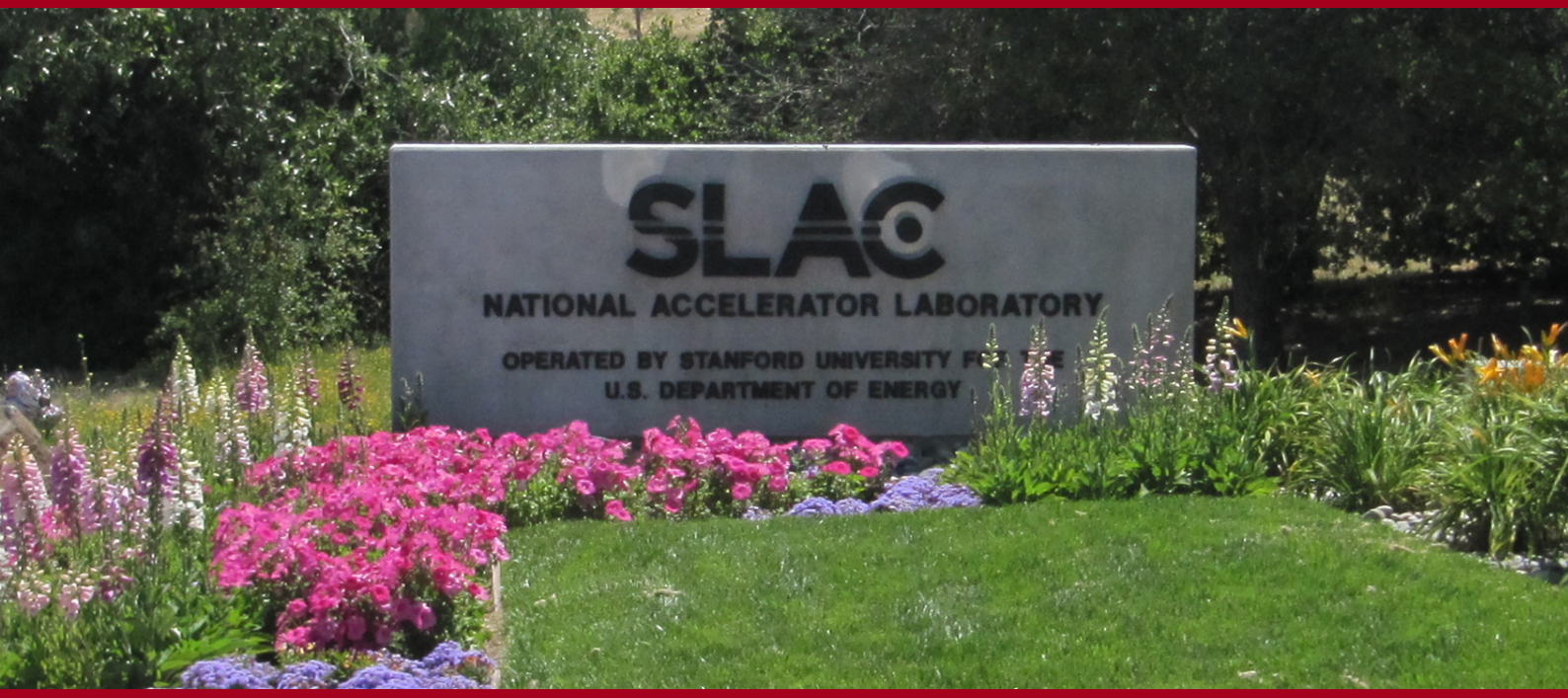

Direct Supervisor:

Marco Oriunno, Dr. Ing.
SLAC National Accelerator Laboratory
Particle Physics and Astrophysic Directorate

Supervisor University of Twente:

Bob van Eijk, Prof. Dr. Ing.
NIKHEF National Institute for Subatomic Physics
ATLAS department

July, 2010

Abstract

This thesis focusses on the advanced cooling issues for the ATLAS upgrade, describing the thermal measurements done to assess the possible use of evaporative carbon dioxide as refrigerant. It has been investigated how CO_2 behaves inside small diameter tubes under different evaporation temperatures and different mass fluxes, centralized around the design properties of the phased upgrade for ATLAS and focussed on the heat transfer coefficient of CO_2. Furthermore, the thermal impedance of the first prototype stave for the IBL upgrade has been determined. To accomplish these goals, the blown system and corresponding data acquisition system at SLAC National Laboratory have been improved to increase the reliability, handle the data better, and make it work faster. Results show that the thermal impedance of the first IBl prototype stave is 11.62 $°Kcm^2/W$, which is twice the value calculated with finite element analysis. The measured heat transfer coefficient of CO_2 shows a clear agreement with the available analytical models. Furthermore, it is concluded that CO_2 would be an excellent coolant for the ATLAS phase I upgrade. However, for the phase II upgrade, CO_2 would be used at its upper limit, and sufficient cooling cannot be guaranteed under the now known design characteristics. It is recommended that a larger database concerning the CO_2 heat transfer coefficient is generated, and that research will also focus on the dry-out point and flow of CO_2 in small diameter tubes. If possible this should be done with a closed loop CO_2 system. Furthermore, it would be wise to analyze more prototype staves to investigate thermal impedances and to check the quality of the used Carbon Foam.

Acknowledgement

On the 14^{th} of February 2010 I flew from an ice cold Holland to a pleasant climate in California, USA to start my traineeship for my master Applied Physics. More than four months I did research concerning CO_2 cooling for the ATLAS upgrades at the Stanford Linear Accelerator Laboratory, now better known as SLAC National Accelerator Laboratory, under supervision of Marco Oriunno.

I want to thank Marco for a lot of things, most of all for giving me the opportunity to work on my own project by giving me the space to develop my own strategies and ideas. Furthermore, I would like to thank him for showing me his sight on California by bringing me to all the interesting places like San Francisco and the headquarters of Apple, Google, Facebook and more, all the sportive games, and especially for giving me and Simone the possibility to have a splendid tour through California. I will never forget my first lesson in parasailing and I still enjoy the memory of our bike trip where San francisco went from visible to completely covered in fog (within 30 minutes). Marco, I hope that you will visit Holland soon and that we will meet again.

I want to thank some more people for giving me an extremely pleasant stay at SLAC. Jim for helping my whenever there where problems in the lab, Dave Nelson for all the help and the 'just pass by' visits, Angelo for the nice walks, Lupe and her crew for all the hard work, and Bob for the humor and stories he always brought with him. Then finally I want to thank Josh Culgan and Traci Kawakami. Traci, without you it never would have been such a great experience! First of all thank you for all the kindness (including the bike, movie festival and the ride to the airport!), the nice diners and trips with Josh, and most of all the superb climb in Yosemite National Park! I hope we meet again and that the three of us can have some great time in the Netherlands or maybe somewhere else.

Credits for the corrections of my work are going to Marco Oriunno and Simone Steuns. They helped me to revise my work by giving me advise about the contents and helping me find all those errors I could not discover.

Two persons I also want to thank are Bob van Eijk and Bart Verlaat: they brought me in contact with Marco and made it possible for me to go to SLAC National Accelerator Laboratory. For me this has been a great working experience that I really enjoyed.

Gijs Hemink
July 31^{th} 2010

Contents

1 Introduction

1.1 Large Hadron Collider

The Large Hadron Collider (LHC) is the world's largest and highest-energy particle accelerator. It is built by the European Organization for Nuclear Research (CERN) to collide opposing proton particle beams at an energy of 7 trillion electron volts (TeV) to test various predictions of high-energy physics. This includes the existence of the hypothesized Higgs boson, and of the large family of new particles predicted by supersymmetry.

LHC is a truly large scale project, lying in a 27 kilometer circumference circular tunnel, as much as 175 meter beneath the Franco-Swiss border near Geneva, Switzerland. It is being funded by, and built in collaboration with over 10,000 scientists and engineers from over 100 countries as well as hundreds of universities and laboratories [1]. The LHC operation started on September 2008 with low energy beams of 450 GeV and in 2010 the beams where finally ramped up to 3.5 TeV; half its designed energy. There the first collision took place, surpassing the world record of 1.18 TeV previously held by the Tevatron at Fermilab [2, 3].

Six particle detectors have been constructed at the LHC to observe the particles produced at the four collision points. Two of them, A Toroidal LHC ApparatuS, better known as ATLAS, and the Compact Muon Solenoid (CMS), are large, general purpose particle detectors. A Large Ion Collider Experiment (ALICE) and LHCb have more specific roles. The last two, TOTEM and LHCf, are smaller and constructed for specialized research.

1.2 ATLAS Detector

ATLAS is the largest detector ever built at a particle collider. Its purpose is to probe the Standard Model by detecting and studying the decay of the particles produced at the interaction point. One of the most important goals of ATLAS is to investigate a missing piece of the Standard Model, the Higgs boson, which would eventually be highlighted by the decay of a specific combination of quarks and leptons. Furthermore, it is investigating CP violation and super symmetry [4].

Dedicated sub-detectors with a large variety of technologies, as is depicted in Figure 1.1, are embedded in magnetic fields to measure charge, energy, mass and momentum of decay products. ATLAS contains six sub-detectors with two superconductive magnetic systems: a two Tesla solenoid surrounding the inner detector, and a set of eight large toroids all situated outside the calorimeters and within the muon system.

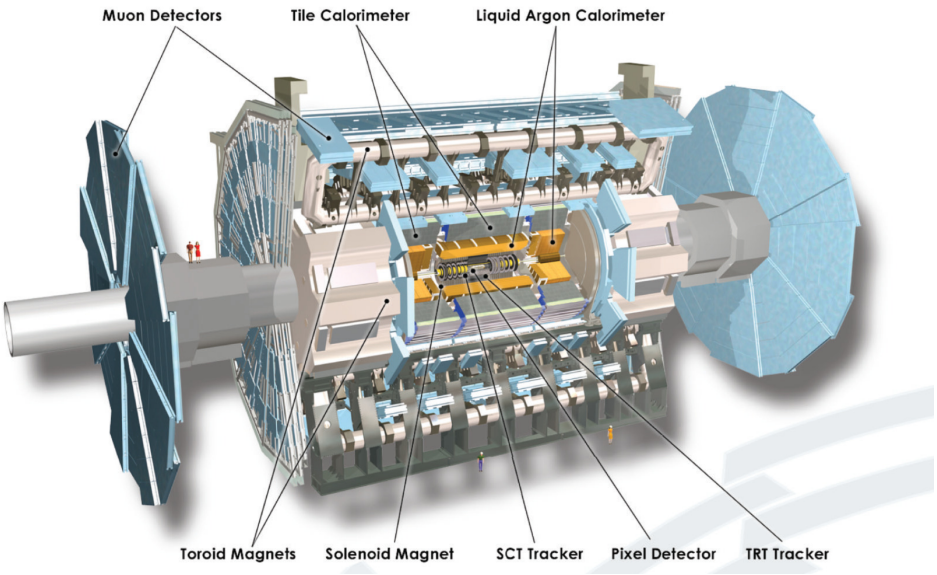

Figure 1.1: *ATLAS experiment with the main detectors. From beam to the outside: vertex detector, SCT tracker, TRT tracker, Liquid Argon Calorimeter, Tile Calorimeter and the Muon detectors. (courtesy of "The ATLAS experiment at CERN, http://atlas.ch")*

Inner detector

Closest to the beam pipe are the Vertex (pixel detector), the Inner Detector (SCT) and the Transition Radiation Tracker (TRT), with planar silicon pixels, silicon strip and gas drift tube technology respectively. They measure the charge and momentum by the bending of the particle tracks in the two Tesla magnetic field.

Calorimeters

The energy of leptons and hadrons is measured with the Electromagnetic and the Hadronic calorimeters, respectively. The Electromagnetic calorimeter is inside a cryostat and cooled with liquid Argon at 87 $^{\circ}K$; lead and stainless steel are used as sampling material. The Hadronic calorimeter operates at room temperature detecting hadrons, mesons, and other particles that interact through the strong force. The sampling material consists of stainless steel and scintillating tiles are used as detecting elements. This results in a high energy resolution.

Muon detectors

Finally, the heavy brother of the electron, the muon is detected at the larger radius in the muon detector. The detector is made of gas resistive plate chambers and placed inside the outer toroidal magnetic field system. Eight

large air-core superconducting barrel loops and two end-cap modules produces a 25.3 meter long and a 20.1 meter in diameter wide magnetic field, storing 1.08 giga joules of energy [4]. The muon's low interaction with the previous described sub-detectors means that it would leave the detector unnoticed if these detectors would be absent. This would compromise the measurement of the total deposited energy. Furthermore, the muon plays a roll in a number of interesting physical processes (e.g. $H \rightarrow ZZ^* \rightarrow l^+ l^- l^+ l^-$ where a Higgs bosons decays to two Z bosons, which will subsequently decay to $e^- e^+$ or $\mu^- \mu^+$ [4]).

Measurements

Measurements of one of the first collisions in ATLAS at 3.5 TeV provides a clear view of how the complete sub-detectors work together to reconstruct an event. This is shown in Figure 1.2.

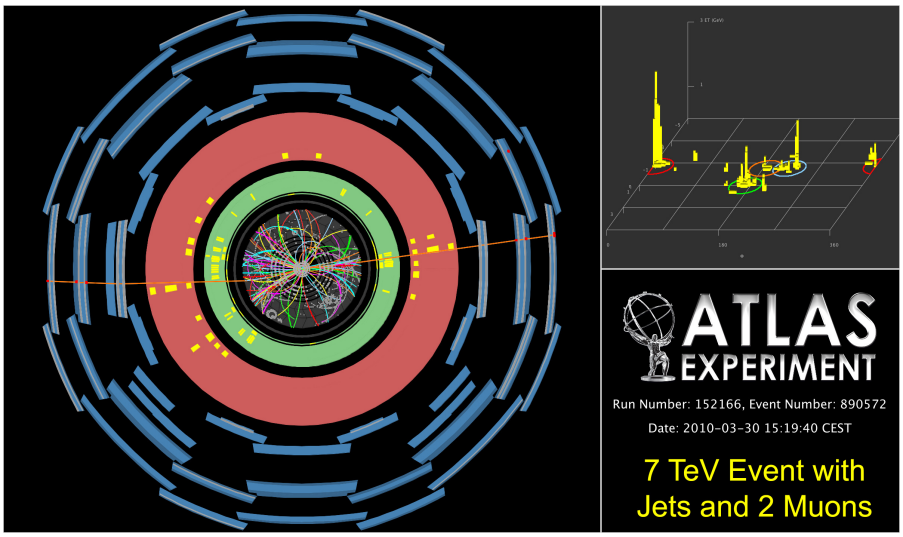

Figure 1.2: *Candidate Z decays to leptons at 7 TeV centre-of-mass energy in the ATLAS detector: 2010-03-30. (courtesy of "The ATLAS experiment at CERN, http://atlas.ch")*

In the middle of Figure 1.2 a lot of colorful curved lines are visible, these are the formed charged particles. Most of them deposit their energies (yellow) in the two calorimeters (green and red, respectively). The two muons that are formed are detected in the muon detectors (blue). By combining the information from the separate detectors the trail of the muons can be traced (the two red lines).

1.3 Phased Upgrades

Development of technology continues, so while the LHC has started, there are already plans for phased upgrades of the machine hardware. The goal is to increase, in steps, the luminosity and consequently the potential of scientific discovery. The proton density will be higher and more collisions will take place. The sub-detectors closest to the collision point will be required to stand higher radiation doses, and have to be constructed with low density materials to be effective in the higher particle background.

Phase I

For the Phase I upgrade, ATLAS has the goal to restore the tracking efficiency that is lost by the detectors getting irradiated once the machine reaches the luminosity of 10^{34} cm^{-2} s^{-1} [4]. This can be accomplished by adding a new layer of pixel sensors mounted on a reduced (29 → 25 mm [5]) beam pipe [6].

Phase II

For the Phase II upgrade the full Inner Tracker needs to be replaced to stand the even more demanding environment due to the high luminosity of 10^{35} cm^{-2} s^{-1}.

R&D

For both phases, research area where intense R&D programs have started are: radiation hard pixels, lightweight local supports and advanced cooling.

1.3.1 Radiation hard Pixel sensors

Three options for the sensors are proposed: planar silicon, diamond and 3D silicon [6]. The first is used in the current pixel detector, has well understood manufacturing sources, offers a high yield at a relatively low cost, but operates at high voltage and degenerates rapidly due to radiation in comparison with the other two options.

Diamond could be a better option, because it needs the least cooling and has low noise while operating. However, manufacturing them with high yield for a low cost has yet to be shown.

3D silicon sensors also seem to be a good alternative, if it can be shown possible to make them with high yield and good uniformity. However, studies for all three sensors are still in progress and decisions still have to be made [6].

1.3.2 Local supports

Lightweight local support with low density, high stability and high thermal conductivity for the pixel sensors is required to minimize the amount of material that can create multiple scattering, providing at the same time adequate cooling performances. New materials like carbon foams are studied with interests and some full scale prototypes are being produced and tested [7].

1.3.3 Advanced cooling

The heat load produced by the front end electronics and the increased leakage current on the sensor due to the high irradiation, require high thermal efficiency and lower temperature to prevent thermal runaway. Moreover, reducing materials, low pressure drop and temperature uniformity along sensors must also be guaranteed.

The present ATLAS Tracker detector is refrigerated by an evaporative flow of octafluoropropane (R218, C_3F_8). Such fluid has generally shown good performance for similar applications [8, 9]. However, it has limitations for use in future detectors because of the low or even sub-atmospheric saturation pressure at the temperatures of interest (-40 °C, -35 °C), and the high pressure drops in small diameter tubes. This limits the potential mass reductions of the structures. Therefore, ATLAS is looking for an alternative refrigerant able to provide low evaporation temperatures around -30 °C [7]. This is especially important for innermost Pixel layers, which have the highest risk of thermal runaway.

1.4 Coolant

Among the refrigerants under consideration is Carbon Dioxide (R744, CO_2), which shows excellent properties, in addition to being a cheap and a natural gas. Besides the great advantage of negligible Global Warming Potential and impact on the ozone layer, it is a dielectric fluid that is not toxic, not flammable and not corrosive [10]. Moreover, it has a high chemical stability under irradiation, which is a necessity for applications involving particle accelerators.

The two-phase flow characteristics of CO2 are quite different from those of other refrigerants, because of the high pressure in operation, the higher vapor density, the lower surface tension, the lower liquid viscosity and the higher vapor viscosity. High pressures and low surface tensions are responsible for the clear dominance of nucleate boiling heat transfer, with values higher than those of conventional refrigerants at the same saturation temperature. In addition, at high mass velocities, dry out may occur at moderate vapor quality. Of special interest for applications requiring

mass reduction, such as the phased upgrade of ATLAS, is the possibility to combine the effects of high pressure and higher heat transfer coefficient. This will reduce the diameter – hence, mass – of the cooling channel and the refrigerants volume.

CO2 has already been used with success to refrigerate scientific instruments, like the space experiment AMS [11], where reliability and low mass requirements are crucial; and for the vertex detector VELO [12] at LHC, in a vacuum vessel at few millimeters from the interaction point, where radiation hardness must also be considered.

The main characteristics of CO2 are:

1. Abundant in nature/cheap
2. Not toxic
3. Not flammable
4. Low triple point at high pressure (–56 °C, 5.6 bar)
5. Low critical point at high pressure (31 °C, 76 bar)
6. High vapor pressure curve (4 to 10 times C_3F_8)
7. Low temperature drop due to low pressure drop at the saturation temperatures
8. Low viscosity
9. High latent heat
10. High heat transfer coefficient

Among all the other properties, those which make carbon dioxide especially attractive for the ATLAS Inner Detector cooling system are its low triple point at still high pressure and the high refrigeration capacity. The first allows to reach the required lower evaporation temperatures. The high refrigeration capacity means an efficient heat absorption by using smaller tubes, thus reducing materials. The high pressure in the pipes (ranging between 10 to 60 bar), provides advantages like an easier achievement of lower temperatures. Furthermore, the low viscosities of the gas and liquid phase mean for two-phase flow a small pressure drop along tubes; resulting in a low temperature gradient along the pixel sensors.

CO_2 Research

Although the study on CO_2 increases, still much should be investigated and documented. There especially is a lack of information concerning the heat transfer coefficient in micro-channels and small diameter tubes at evaporation temperatures below 0 °C. This information is vital to determine if CO_2 can be used as coolant, because the fluid has to be capable of evacuating more than 6 kW/m^2 of produced heat.

1.5 Focus

This thesis focusses therefore on the advanced cooling issues for the ATLAS upgrade describing the thermal measurements done to assess the possible use of evaporative carbon dioxide as refrigerant. It will investigate how CO_2 behaves inside small diameter tubes under different evaporation temperatures and different mass fluxes, centralized around the design properties of the phased upgrade for ATLAS and focussed on the heat transfer coefficient of CO_2. Furthermore, the thermal impedance of the first prototypes staves for the insertable B-layer (IBL) upgrade will be determined. To accomplish these goals, the blown system and corresponding data acquisition system at SLAC National Laboratory have to be improved to make it work faster, handle data better, and increase reliability.

1.6 Thesis Outline

In chapter 2 more details for the detector upgrades are presented followed by theoretical models of heat convection. The experimental setup and the blown systems improvements that have been designed and constructed will be explained in chapter 3. It also presents the renewed data acquisition system, which contains a Labview program that is responsible for data taking and a Matlab program that is capable of processing the data, calculating all the needed quantities, and eventually compares the results with the available theoretical models [13, 14] for CO_2. Subsequently, the results concerning the thermal impedance of the protype stave and the heat transfer coeffcient of CO_2 are presented in chapter 4. In chapter 5 simulation for the phase I & II upgrade based on the analytical models for CO_2 are presented. Finally, the deduced conclusions are presented in chapter 6, followed by some remarks and details about further investigation.

2.1 Cooling Requirements

2.1.1 Thermal runaway

Semiconductor based detectors, particularly pixels, need to be cooled to evacuate the heat produced by the front end electronics to reduce the noise due to leakage current and to provide stable operation conditions against the so called thermal runaway.

The power Q_{Si} $[W]$ dissipated by a silicon detector itself is given by the product of bias voltage U_{bias} $[V]$ and leakage current I_{leak} $[A]$[15].

$$Q_{Si} = U_{bias} \cdot I_{leak} \tag{2.1}$$

The bias voltage has to be much higher than the depletion voltage U_{dep} to guarantee satisfactory detector operation. This may reach over hundreds of volts after a few years of LHC operation due to type inversion and reverse annealing. Fortunately, the latter can be avoided if the silicon detectors are always kept below 0 $°C$: this sets the first upper limit for cooling. This requirement also has to be ensured when the experiment is shutdown for repair work. The leakage current increases with radiation dose because of radiation damage formed mostly due to bulk damage in silicon. The total power dissipation of a radiated silicon sensor can be approximated by using Boltzmann statistics, as presented in Equation 2.2 [15].

$$Q_{Si}(T, U_{bias}) \approx U_{bias} \cdot \kappa \cdot \Phi \cdot V \cdot T^2 \cdot \exp \frac{-7020.7K}{T} \tag{2.2}$$

Here κ is the leakage current damage constant $[A/m]$ ($\kappa \approx 3.5 \cdot 10^{-15} A/m$ at 20 $°C$ [15]), Φ is the particle fluence $[1/m^2]$ to which the detector has been irradiated, V is the silicon sensor volume, and T the temperature of the silicon $[°K]$. In the temperature range of interest this means that the leakage current doubles every 7 $°C$ [15].

The temperature gradient between the sensor and the fluid can be formulated introducing the thermal impedance parameter R as:

$$(T_s - T_w) = \frac{Q_{Si}\,(T_{Si}, U_{bias})}{R} = \frac{Q_{Si}\,(T_{Si}, U_{bias})}{R_f + R_k} \tag{2.3}$$

Where R $[°Km^2/W]$ includes the global effect of the convection of the coolant R_f and of the conduction of the stack of material between the tube and the sensor R_k. Equation 2.3 describes a dynamic system with positive nonlinear feedback system: an increase in the silicon temperature leads to

an increased power dissipation, which in turn causes an increase in temperature. This vicious process that is crucial to avoid at all times is called thermal runaway, and it imposes the strongest requirements: it calls for low power dissipation, and low thermal impedance of R_f and R_k. Low values of R_f are achievable with high values of heat transfer coefficients, which is an characteristic of evaporative cooling, especially with CO_2. Low values of R_k are achievable with high thermal conductivity material like carbon graphite. The power dissipation depends on the sensor technology. For the ATLAS IBL Project are Planer, 3D and Diamond sensors under consideration.

Planar sensors

The planar technology for Pixel is well known and is used succesfully in many High Energy Physics (HEP) experiments. The drawback is a higher sensitivity to the radiation damage that in the case of the IBL will require operation voltage $\sim 1000\ V$ with higher risk of the thermal runaway. The temperature requirement for the sensors is set to $< -15\ ^{\circ}C$, which in turn means a refrigerant of $-30\ ^{\circ}C$ to guarantee long term operation [16] and sufficient protection against the thermal runaway.

3D pixel sensors

3D Pixels are more radiation hard than Planar, therefore having less cooling constraints. Furthermore, the depletion voltage is a factor of four lower and the collection time is faster. This is due to its unique design, as is depicted in Figure 2.1.

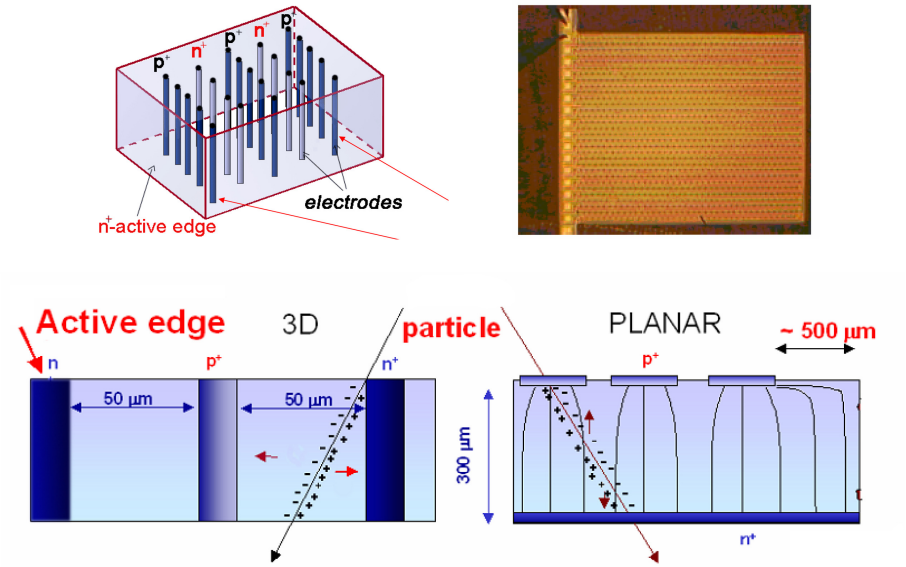

Figure 2.1: *3D silicon sensors have a much smaller distance between its n and p doped parts resulting in desirable characteristics. (courtesy of [17])*

The differences are due to the distance between the *n* and *p* doped parts, which is sensationally smaller (300 μm to 50 μm). To achieve the same electric field a lower voltage can be applied, and the ionized charges have to travel less. This results in faster read-out time, and furthermore, decreases the chance that the charges interfere with damage lattices inside the silicon. The effective radiation hardness of the sensors is thereby increased [17]. Especially the lower depletion voltage is interesting, as it results in lower requirements for the cooling system. Although the most power is dissipated in the read-out chips of the sensors, and therefore is the same for planar, 3D and diamond sensors, after years of operation the increase in depletion voltage cannot be neglected. A reduction is therefore a considerable step.

The limitation of 3D pixels is the production yield and the capacity to produce them in sufficient amounts for HEP experiments.

Diamond

Diamond sensors become more popular due to the extreme radiation hardness and leakage currents less than 10 nA/cm^2 [7]. The power consumption of the sensors themselves is small, reducing the cooling and support structure.

Thermal design

The planar sensors are an available technology and present the most challenging requirements for the cooling, therefore the thermal design of the IBL is done to meet their goals, nominally keeping local sensors at $-15\ ^{\circ}C$ with a refrigerant at $-30\ ^{\circ}C$ [10].

2.1.2 Thermal impedance of the local supports

The local supports must be made of materials with low density to reduce multiple scattering, high thermal conductivity to reduce the temperature gradient, and low coefficient of thermal expansion to provide mechanical stability stress release. Carbon based materials like TPG have been largely adopted in the present ATLAS Pixel [18]. Carbon Foams are new materials which show even better properties, and for that reason are preferred for the IBL local support [7]. The thermal impedance of the local support can be defined as the ratio of the temperature gradient between the sensor and tube wall, and the heat density applied. It depends only on the material properties and in analogy with electricity is a measure of the thermal resistance of the passage of heat through the stack of materials.

$$R = \frac{\Delta T_{s,w}}{q} \tag{2.4}$$

In Equation 2.4 [19], R is the thermal impedance $[^{\circ}Km^2/W]$, ΔT is the temperature difference between the sensor and the wall surrounding the cooling fluid and q is the power density $[W/m^2]$.

2.1.3 Upgrade design

Specific local support design are under development for the upgrade phase I and phase II, respectively.

Phase I IBL stave

A cross-section of the IBL stave is depicted in Figure 2.2. The stave will be 840 millimeters long and 18 mm width. The sensors are glued on carbon foam that is stiffened by a carbon fiber sheet with an *Omega* shape [7].

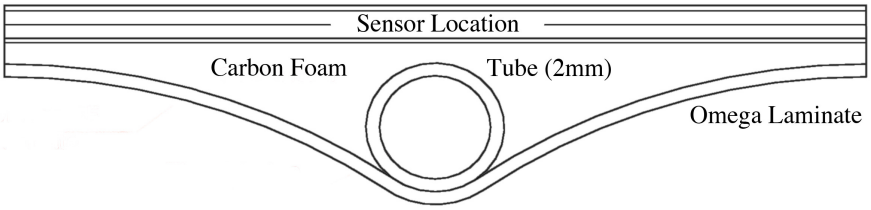

Figure 2.2: *Front view of IBL prototype stave, with on top the sensors, supported by carbon foam and the coolant tube which is sandwiched between the Omega laminate and the carbon foam.*

The cooling tube embedded in the Carbon foam will be in titanium because of its low density and low coefficient of thermal expansion. The aimed inner diameter falls in the range of 1.5 and 2 mm with a wall thickness of ~ 0.1 mm. The nominal power that has to be transferred to the coolant is 76 W or 0.6 W/cm^2, applying a safety factor of 1.5 this becomes ~ 120 W, or 1.0 W/cm^2. For an inner diameter of 2 mm this would mean that the heat flux on the tube is 22.7 kW/m^2 [7].

Phase II sLHC

The local support stave for sLHC Outer Pixel has a mechanical design similar to the IBL with carbon foam sandwich between carbon fiber sheets. However, the detectors will be mounted on both faces. The total length will be ~ 1500 mm and the width ~ 4 cm [17]. The nominal power dissipation is higher than the IBL, and is estimated at 200 W, or 300 W with a safety factor of 1.5. The heat flux seen by the tube will be 31.8 kW/m^2.

2.2 Thermal Impedance of the Fluid

The high heat transfer coefficients, required to get low thermal impedance in the tube, are achieved by means of the forced convection of the coolant. This usually happens in liquid mono-phase or evaporative (boiling) regime. The boiling regime shows the highest values, but the design and the operation of the cooling system is more challenging than the liquid mono-phase.

In this section the fundamental relationships of the heat transfer by forced convection for both regimes used in this study are briefly recalled. Heat transfer by forced convection of fluids in tubes is a efficient way to remove heat by electronic equipments and finally particle detectors. The heat transfer coefficient, h, is the main parameter describing the process and, in analogy with the definition of the thermal conductivity in the Fourier equation, is defined as the amount of heat transferred by conduction through the laminar stream lines in the boundary layer at the tube-fluid interface.

$$Q = h \cdot \left(\pi D_i l \Delta T_{w,f}\right) \tag{2.5}$$

Here Q is the applied power $[W]$, h is the heat transfer coefficient $[W/m^2\ ^\circ K]$, D_i the inner diameter $[m]$ of the tube, l the length $[m]$ of the tube and ΔT the temperature difference $[^\circ K]$ between the tube's inside wall and the coolant.

Forced convection can happen in mono-phase (gas or liquid) or two-phase (liquid and gas) regime with a large variation of the heat transfer coefficient. In the gas mono-phase regime h is lower than in the liquid mono-phase, because of the lower thermal conductivity. Once the heat is transferred to the fluid, the temperature increases accordingly to the so called heat capacity and mass flow:

$$\Delta T = \frac{Q}{C_p \dot{m}} \tag{2.6}$$

Here ΔT is the total temperature increase $[^\circ C]$ of the fluid between the inlet and outlet of the tube, C_p the heat capacity $[J/kg\ ^\circ K]$, and $\dot{m}$ the mass flow $[g/s]$.

In the two-phase regime (boiling or condensation) the inherent change of fluid phase (nucleation) allows to exchange a larger amount of heat with heat transfer coefficients an order of magnitude larger than in the case of mono-phase. Moreover, in two-phase flow the fluid temperature stays constant.

2.2.1 Mono-phase flow

Liquid mono-phase fluids can be excellent coolants, one example of such is water, which in liquid form has a high heat transfer coefficient and thus can be used in a large temperature scale.

Several theoretical models exist for the heat transfer coefficient in mono-phase regime, based on the Nusselt numbers, as is presented in Equation 2.7 [19].

$$h = \frac{Nu_D k}{D_i} \tag{2.7}$$

Here Nu_D is the dimensionless Nusselt number, which provides a measure of the heat transfer convection occurring at the surface between fluid and wall, given by the Dittus-Boelter equation for cooling in Equation 2.8 or by the Gnielinski equation as shown in Equation 2.9 [19]. k is the thermal conductivity $W/m^\circ K$.

$$Nu_D = \frac{0.23 Re_D^{0.8} Pr^{0.3} k}{D_i} \tag{2.8}$$

$$Nu_D = \frac{(f/8)(Re_D - 1000)Pr^{0.3}}{1 + 12.7(f/8)^{1/2}(Pr^{2/3} - 1)} \tag{2.9}$$

Here Re_D is the Reynolds number presented in Equation 2.11, Pr the Prandtl number presented in Equation 2.12 and f the friction factor as shown in Equation 2.13—if the Gnielinski equation is valid—; the latter can also be obtained from the Moody diagram [19]. Equation 2.8 and Equation 2.9 are valid in the following conditions:

$$\begin{bmatrix} 0.7 < Pr < 16,700 \\ Re_D > 10,000 \\ \frac{l}{D} > 10 \end{bmatrix} \tag{2.10}$$

Although in textbooks [19, 20] the transition region is also given, e.g. the Reynolds number is valid if $Re_D > 2300$, caution should be exercised when applying this correlation to turbulent flow, because it can easily result in wrong approximations.

$$Re = \frac{4\dot{m}}{\pi \mu D_i} \tag{2.11}$$

The Reynolds number represents a criterion to distinguish between laminar and turbulent flow, where μ is the dynamic viscosity $[Pa \cdot s]$.

$$Pr = \frac{C_P \mu}{k} \tag{2.12}$$

The Prandtl number approximated the ratio of kinematic viscosity and thermal diffusivity inside a tube, thereby giving information how heat is transported perpendicular to the mass flow of the fluid.

$$f = (0.790 \ln Re_D - 1.64)^{-2} \tag{2.13}$$

The friction factor relates the roughness of the tube inner wall to fluids, which is one of the major causes of pressure drops along tubes [20].

Pressure drop

The pressure drop for mono-phase flow can be calculated with Equation 2.14 [15]. Beside calculating the theoretical pressure drop over a tube, this formula, which is shown in Equation 2.15, can also be used to calculate the mass flow if a good indication for the Reynolds number exists and the pressure drop is known [15].

$$\Delta P = \Omega \cdot l \cdot f^2 \text{ with } \Omega = \begin{cases} \frac{0.31}{Rey^{0.25}} \frac{8\rho}{\pi^2 D_i^5} & \text{if } Rey > 2300 \\ \frac{100}{Rey} \frac{8\rho}{\pi^2 D_i^5} & \text{otherwise} \end{cases} \tag{2.14}$$

$$\dot{m} = \begin{cases} \left(\frac{\pi^2 \rho D_i^5 \Delta P}{0.31 \cdot 8 \cdot l} \left(\frac{4}{\pi \mu D_i} \right)^{\frac{1}{4}} \right)^{\frac{4}{7}} & \text{if } Rey > 2300 \\ \sqrt{\left(\frac{\pi D_i^4 \Delta P}{200 \cdot \rho \mu} \right)} & \text{otherwise} \end{cases} \tag{2.15}$$

ΔP is the pressure drop $[Pa]$ over a certain length l of cylindrical tube with inner diameter D_i, f is the volume flow $[m^3/s]$ ($f = \dot{m}/\rho$), ρ the density of the fluid $[kg/m^3]$, and Rey the Reynolds number as in Equation 2.11.

2.2.2 Two-phase flow

Two-phase flow is of particular interest for cooling applications, because it provides the highest heat transfer coefficient. It is, however, also the most difficult situation to describe and there is a lack in literature of reliable theoretical models. Moreover, the models are tuned for specific fluid and specific temperature range. Databases are available in literature for the heat transfer coefficient of many fluids of interest like Ammonia, R134a, R402A, R404A, R502, R123 and Carbon Dioxide. [21, 22, 23, 24, 13, 14]. In the specific case of CO_2 there is a lack of data at low evaporating temperatures and small diameter tubes.

Boiling processes

The boiling process occurs in several steps, thereby transformig liquid into vapor. Assuming a tube where the fluid is entering in liquid form—vapor quality is zero – forced convection is dominant, see Figure 2.3. Secondly, when the vapor quality increases, small bubbles will nucleate, grow and depart from the heated surface carrying more heat away. This is referred to as nucleate boiling, shown in Figure 2.4. Subsequently, when even more heat is applied the bubbles will become larger, and a transition region arises, after which a stable layer of vapor will form around the wall. This so called dry-out reduces the heat transfer [25].

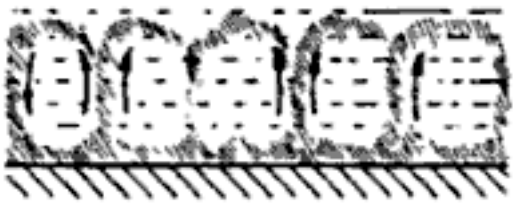

Figure 2.3: *Heat from the bottom is exchanged with a fluid by means of natural convection. (courtesy of [25])*

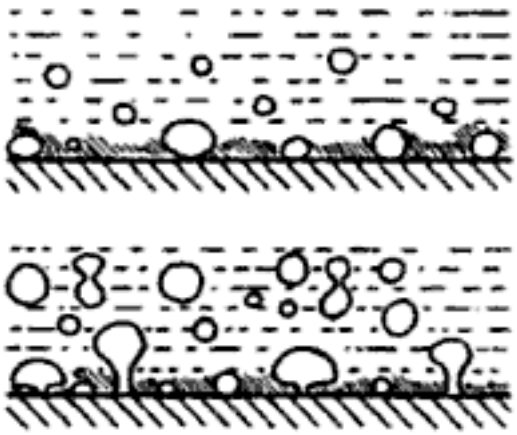

Figure 2.4: *Heat from the bottom is exchanged with a fluid by means of nucleate boiling. In the upper picture a low heat flux is applied while in the bottom picture a higher heat flux is applied. (courtesy of [25])*

The behavior of the fluid under evaporation in tubes is visualized in Figure 2.5. Interesting flow regions for refrigeration are; intermittent flow (which is the collection of bubble to slug flow), and annular flow. The dry-out/mist flow, which is the part where the tube wall is covered by vapor instead of liquid is less interesting for refrigeration because the heat transfer reduces,. However, it is therefore of outermost importance to know when it will happen.

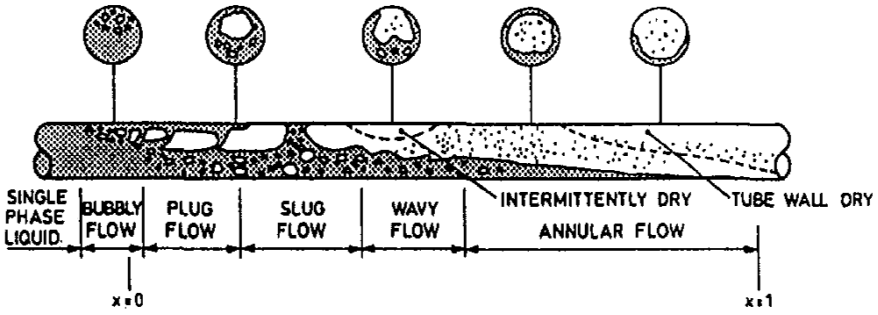

Figure 2.5: *Boiling pattern of two-phase flow inside horizontal circular tube. As soon as the wall is not completely covered with liquid the heat transfer coefficients reduces. On the left the vapor quality $\chi = 0$ and on the right $\chi = 1$.*

At the same vapor quality it is possible to have different kinds of flow because also the coolant's mass flux has an influence. This can be depicted in a flow pattern map as is done in Figure 2.6, which are flow pattern maps for R-22 under different heat loads.

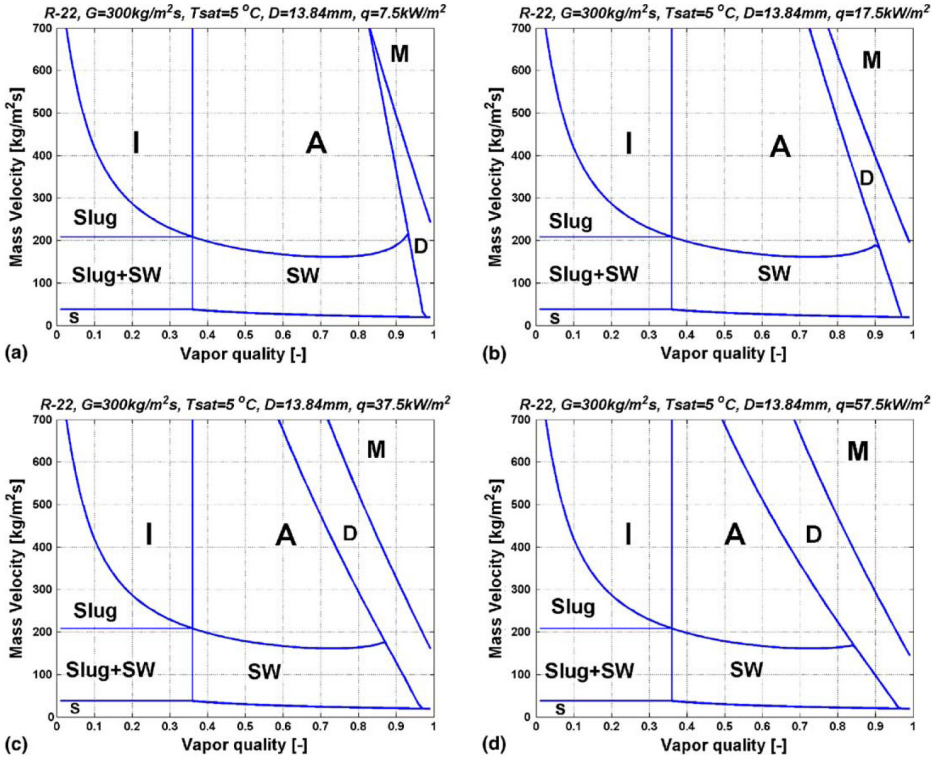

Figure 2.6: *Flow pattern maps of R-22 for D_i = 13.84 mm, G = 300 Kg/m^2s and different heat loads. I stands for intermittent, A for Annular, D for Dry-out, M for mist and SW for stratified wavy. (courtesy of [26])*

Intermittent flow

Intermittent flow is the region at low vapor quality and represents the part where forced convective boiling is mostly dominant. The tube wall is fully surrounded by liquid and the heat transfer is large.

Annular flow

Annular flow is represented by flow that is in contact with the heated surface. Due to the forced flow, nucleating bubbles that arise will be transported away quickly resulting in an increasing heat transfer when the bubbles become larger, as long as there is contact between the wall and liquid.

Dry-out

In the dry-out regime there is no direct contact between the heated surface and the liquid inside the tube, instead it is in contact with vapor which has a much lower heat transfer. Depending on the coolant characteristics, this

results in a sharp decline in heat transfer. This marks the point where most evaporative fluids lose there cooling capabilities.

Mist flow

When the liquid bubbles in the dry-out flow decline mist flow arises. This flow contains mostly gas and therefore has a low but stable heat transfer.

2.2.3 Boiling characteristics CO_2

The high operating characteristics of CO_2 result in high vapor densities, low surface tensions, high vapor viscosities and low liquid viscosities. The low surface tensions in combination with the high pressures have major effects on nucleate boiling heat transfer characteristics. Clear dominance of the nucleate boiling over forced convective boiling result in much higher heat transfer coefficients. Furthermore, it has been shown that significant deviations between general and CO_2 flow pattern maps exist: dry-out in evaporative CO_2 occurs at moderate vapor quality and heat transfer is declining rapid, or even steep. Specific CO_2 models have been under development [13, 14], but are too extended to summarize here. They try to describe two-phase CO_2 completely, including predictions of heat transfer coefficient, flow pattern maps and pressure drop models.

3.1 CO_2 Blown System

A versatile, scalable and cheap cooling test stand, called Blown System, has been developed at SLAC to characterize the heat transfer properties of CO_2. Liquid CO_2 is spilled out from a CO_2 bottle to the experimental setup where it passes through a flow meter that measures the flow rate and temperature of the fluid. Subsequently, the fluid flows through an absolute pressure sensor and the first heat exchanger. Here an external chiller cools the CO_2 down to 10 $°C$ using water, and -10 $°C$ if a water glycol mixture is used.

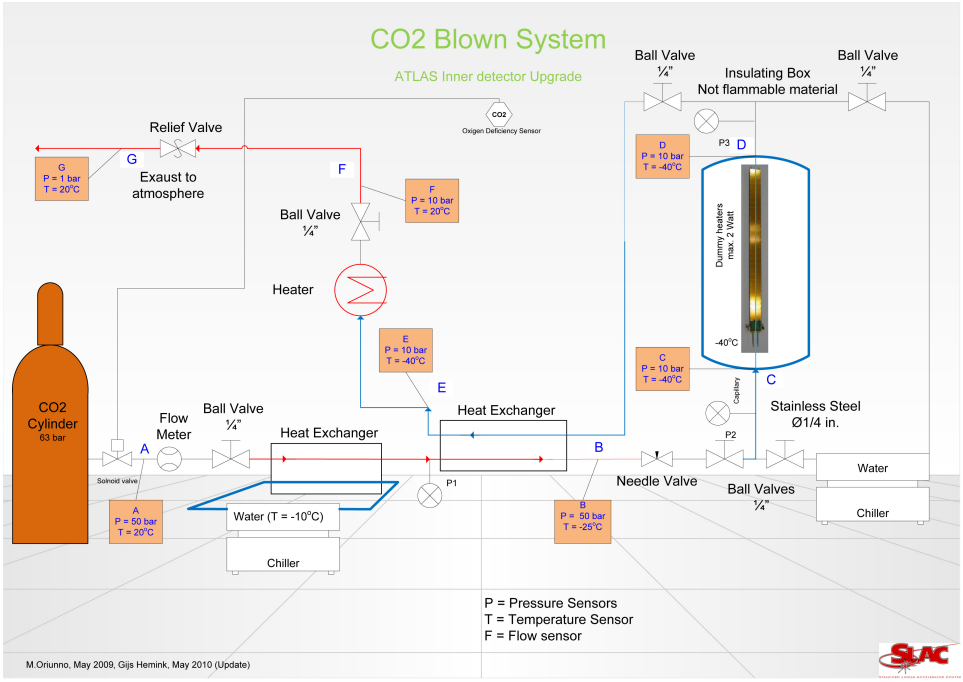

Figure 3.1: *Improved CO_2 blown system, with an additional heat exchanger and a decouple system to switch to water measurements.*

The fluid then passes through a second heat exchanger where cold CO_2 flows in counterflow, thereby bringing down the temperature of the CO_2 even more. After this pre-cooling area, the fluid passes a needle valve: here the pressure is decreased, and consequently the temperature drops.

Subsequently, the CO_2, which is now at the desired temperature, will enter the test area where it first flows through a gauge pressure sensor, and then enters the test tube. A second gauge pressure sensor is placed at the end of the tube, thus allowing the of the pressure drop over the test tube to

be measured. Before the fluid is heated up to room temperature and blown in open air, it first flows through the (second) heat exchanger: the still cold fluid is used to bring down the temperature of the entering CO_2. A pressure regulator valve is placed after the heater to control the pressure – hence, the coolants temperature that enters the test area. The implementation of two ball valves before and two after the test area allows for a smooth switch between the usage of CO_2 or water as refrigerant. The blown system can be disconnected from the test area and the connected (water) chiller can then be used. At the end of the system a relief valve (opens at 40 bar) is placed in case pressure inside the system builds up too high. Finally, an Oxygen Deficiency Sensor is placed above the setup: in case of low oxygen it shuts down the outside placed bottle by means of a solenoid valve.

Further details about the used hardware and sensors is summarized in subsection 3.3.1.

3.2 Improvements made to CO_2 Blown System

The knowledge of the blown systems functioning as described in section 3.1 was at the start of this thesis inadequate. One of major challenges before measurements could commence was to fully understand the system and to improve the deficiencies. In this section the main issues and applied or proposed solutions are shortly explained.

3.2.1 Mass flow regulator

The first main issues concerns the mass flow rate, or mass velocity ($G = 4\dot{m}/\pi D_i^2$). The mass flow is regulated by the needle valve and is placed after the pre-cooling of the entering CO_2. The pressure drop over the needle valve, regulated by the pressure valve placed after the test area, causes the transition from vapor flow to the desired two-fase flow. Unfortunately, the result is an inconstant flow rate, as depicted in Figure 3.2.

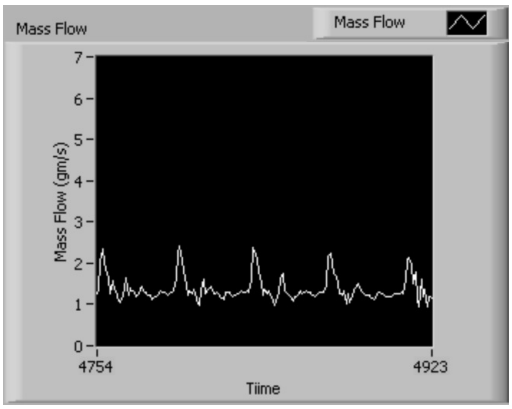

Figure 3.2: *Measurement of the mass flow, although it should give a constant flow rate, deviations of more than* 100% *are visible.*

Consequently, the mass flow increases and the pressure rises, thereby increasing the saturation temperature. The result is a vicious cycle, while a equilibrium is necessary, making it impossible to do repeatable measurements.

This problem arises because the needle valve is used at its lower limit creating an already unstable situation for the mass flow. However, it works acceptable in most cases. Two additional reasons have been found: a pressure wave inside the system, and the rapid pressure decline of the CO_2 bottle. The former is caused by an unnecessary tube connected to an old pressure sensor still attached to the system, after the needle valve, but before the test area. Removing this piece solved the first problem. The solution to the second problem is to change the bottle, if running at flow rates of 1 g/s is a necessity. Another option is to increase the flow rate to above 2 g/s. The applied changes result in a stable mass flow.

3.2.2 Temperature sensors

The used temperature sensors should have a deviation of $\pm 0.2\ ^\circ C$ at most, however deviations up to $\pm 1.0\ ^\circ C$ have been measured between sensors. This can be explained by the thermal impedance of the tube and used glue. This is solved by using a different glue technique as is shown in Figure 3.3. Moreover, calculations show that the wires to the sensors have to be connected to the tube, otherwise they will transport the ambient temperature to the sensors, thereby influencing the measurement.

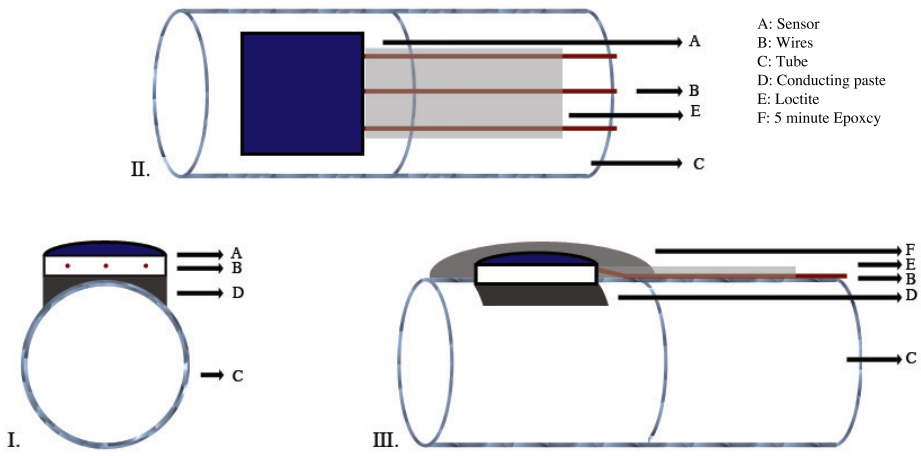

Figure 3.3: *The three steps in the glueing process. First the sensor is firmly attached with conducting paste to the tube. Subsequently, the wires are glued as firmly as possible to the tube with Loctite. The final step is to cover the sensor with epoxy to make sure no heat from around the tube comes in contact with the sensors. Furthermore, it also protects the sensor to slip off in case of shocks.*

However, this glueing process does not solve the large deviations that have been found with the two sensors implemented inside the pressure sensors: they are not glued to anything, but are in direct contact with the refrigerant. It is possible that the temperature gradients during the start up of the CO_2 blown system damages these sensors. They are essential for the calculation of the heat transfer coefficient – the slope of the fluid is calculated from these two values – therefore, a calibration is necessary. For water measurements the chiller's temperature can be used as a reference. This is not possible for CO_2. Here the properties of the two-phase flow can be exploited, because the temperature equals a certain pressure. Hence, if the pressure is known at the inlet of the tube – which is, with a smaller error relative to the temperature sensors – the corresponding temperature is know.

3.2.3 Second heat exchanger

Due to safety reasons the CO_2 bottles are located outside the building. The implications are that the sun shines on the bottle for a good part of the day, thereby heating up the bottle and consequently increasing the flow temperature and pressure. This effect has significant influence on the measurements, making it difficult to reproduce stable circumstances.

The solution was to create a second heat exchanger that pre-cools the CO_2 from the bottle to a temperature independent of the sunshine. This is achieved by putting the chiller, which is not used for CO_2 measurements,

on this heat exchanger. The temperature can be set as low as 10 °C if the cooling fluid is water, and even lower (−10 °C) if a water (50%) glycol (50%) mixture is used.

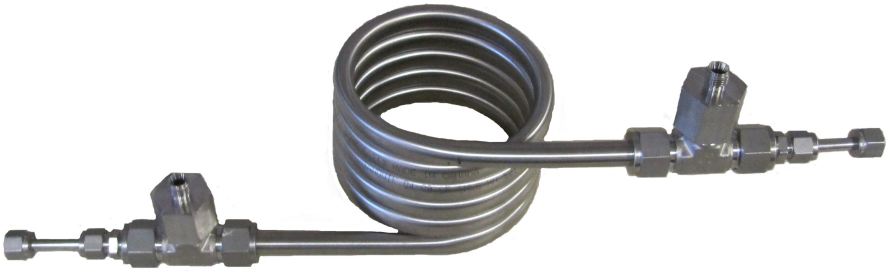

Figure 3.4: *Second heat exchanger that is placed after the mass flow meter but before the original heat exchanger.*

The heat exchanger is shown in Figure 3.4 and is directly placed after the mass flow meter in Figure 3.1. This improvement not only made the system independent of the sunshine on the bottle, but in combination with the original heat exchanger it also lowers the vapor quality: for −30 °C the vapor quality is now almost zero. This makes it possible to do a more thorough study of the tubes.

3.2.4 Water versus CO_2 measurements

When a new tube has to be analyzed, first a water measurement is done. However, letting water into the system results in problems when the switch to CO_2 is made. Getting the water out of the blown system, especially out of the mass flow meter and the needle valve, results in freezing phenomena when CO_2 is switched on if this is not done properly. A needle valve blocked with ice crystals interrupts the flow of CO_2, thereby ruining the measurement. Furthermore, CO_2 reacts with water to form H_2CO_3 (Carbonic acid), which can deposit itself onto the wall of the test tube influencing all the measurements.

A solid solution to this problem has been made by implementing two ball valves before the inlet pressure sensor and two ball valves after the outlet pressure sensor: this makes it possible to switch between two different fluids. A much smaller part now has to be flushed with N_2 gas to lower the humidity, decreasing the chance of ice inside the blown systems critical parts, without modifying the system.

3.2.5 Electronics

The used electronic read-out system was confusing. Wires from the Labview blocks had to be connected to the right sensor two meters away. Furthermore, the distribution of power to the pressure sensors was not clear; cables could not be changed when broken and the distance of the test area to the blown system was limited. National Instruments equipment makes it difficult to disconnect sensors, therefore a plug and play system for the temperature sensors has been designed, which consists of a box with 27 connections. This box is always connected to the National Instruments blocks (NI 9217), however, the sensors can be disconnected quickly. For the other used sensors a connector has been placed directly on the National Instrument block (NI 9205) also making them changeable. The distribution of power has been modified to a boxed version, the same applying for the common ground: these boxes are depicted in Figure 3.5.

(a) The voltage distribution box: it has five output connectors and one input connector.

(b) The voltage and ground box is shown: it has three grounds, two output connectors and one input connector.

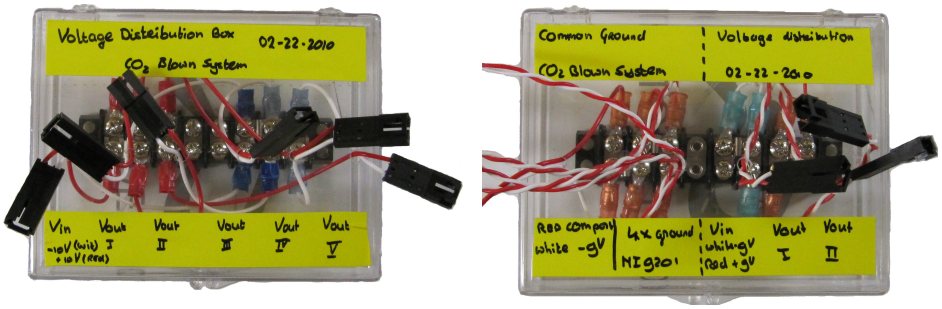

Figure 3.5: *Voltage (3.5a) and ground distribution (3.5b) boxes that have been made to increase the comprehensiveness of connection between the power and ground to sensors.*

The system is now transformed to a plug and play system where sensors can easily be connected: broken cables can be taken out fast and changed by new ones; the distance between the test area can be made as long as needed; and most of all, it is now clear where and how each sensor has to be connected.

3.2.6 Power safety box

A stronger power supply was needed due to the decrease of overall resistance in different tubes. In operating mode it was found that the power supplies safety system had shortcomings. Therefore, a hardware based safety system has been design. It consists of two independent switches

placed in series, which are temperature triggered, (seeFigure 3.7), and are mounted inside a box placed between the wall and power supply. The electrical scheme is depicted in Figure 3.6.

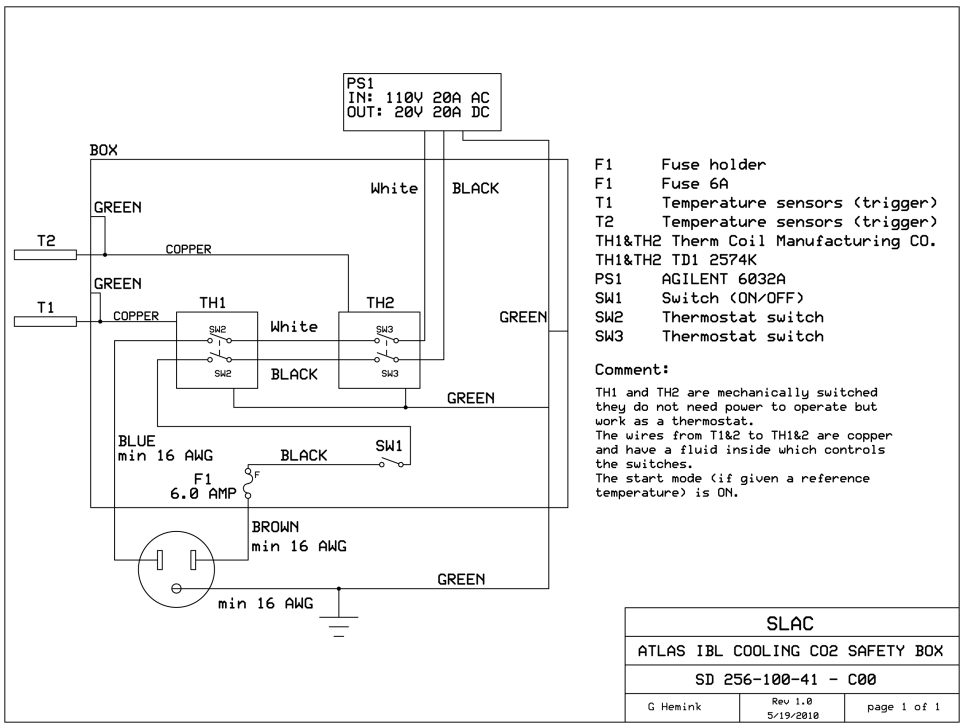

Figure 3.6: *Electric scheme of the power supply safety box, consisting of two switches placed in series. The temperature sensors, T1 and T2, are placed inside the isolation box of the tubes and are then set to a reference value. If this value is reached at one of the sensors it breaks the circuit and the power supply is shut down. Also, a fuse and on/off switch are implemented conform SLAC safety rules.*

Figure 3.7: *Temperature sensor from the power safety box attached to the tube, an electrical isolation layer, is placed in between to prevent a short circuit.*

The box has been approved by the SLAC EEIP department and prevents the prototype from overheating.

Power connections

The connection of the wires from the power supply to the tube have also been improved. This is visualized in Figure 3.8 where to copper blocks are cramped over the tube allowing fast changeability to other tubes and without creating additional resistance in the system. They have been made for all test tubes diameters.

3.2.7 Thermal isolating box

There was no appropriate isolation box available, therefore a new one has been designed and built: with a length of 1.70 by 0.15 meter, it is able to contain both test tubes for the phase I and phase II upgrades. It is filled with non-flammable isolation material and can be closed by two latches. The box is depicted in Figure 3.10.

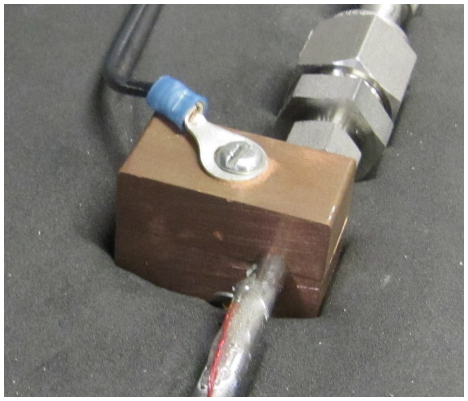

Figure 3.8: *Two copper blocks cramped around the tube distributing the current along the tube. They are connected to a power supply.*

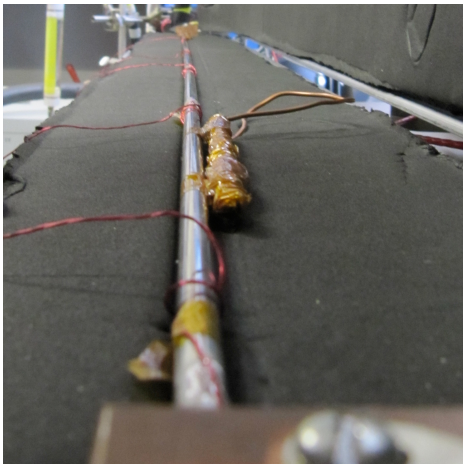

Figure 3.9: *Tube placed inside the isolation box. Visible are the temperature sensors wires leaving the box and a safety temperature sensor.*

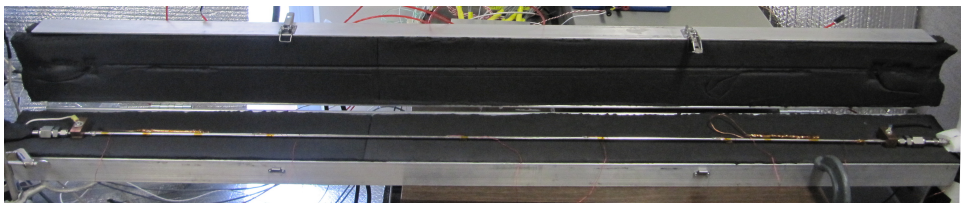

Figure 3.10: *New isolation box with a length of* 1.70 *meter, it is capable of running tests for the IBL and sLHC pixel upgrades.*

3.3 Data acquisition system

The data acquisition system (DAQ) of this setup consists of three parts: hardware (subsection 3.3.1), read-out system (subsection 3.3.2), and a data analyzing program (subsection 3.3.3).

3.3.1 Hardware

Various sensors are used to determine the necessary data and supply power, they are summarized in Table 3.1, including model and operating range.

Sensors	Model	Range
Absolute pressure sensors	PTX 7200	0 → 1400 bar
Chiller (max. 2.9 kW)	PolyScience 6561T	−10 → 35 °C
CO_2 bottle	Airgas	50 lb
Flow meter	Rheonik RHM 015	0.004 → 0.6 kg/min
Gauge pressure sensors	Druck DPI 104	0 → 690 bar
Humidity sensors	Apollo HIH series	0 → 100% RH
Labview DAQ	NI c-DAG 9172	9 block places
Labview blocks	NI 9205 & NI9217	1 & 8 blocks, resp.
Power supply (applied heat)	Agilent 6032A	20V, 50A
Power supply (electronics)	BK precision 1786A	0 → 30V
Safety sensors	Therm Coil TD1 2754K	60 → 250 °F
Temperature sensors	OmegaFilm Pt Class A	−50 → 450 °C

Table 3.1: *Overview of used electronic device and sensors.*

The DAQ of the RTD temperature is operated by the specialized Labview block, NI9217. The value of the pressure sensors can be deduced from the current used to operate the sensor. The NI9205 however measures only the voltage drop, therefore a resistor is placed over each pressure sensor. This allows Labview to determine the current used by the sensors. The humidity sensors, the mass flow value and the fluid temperature are also read out in this way. The latter is also measured by the mass flow meter. In Figure 3.11 the two different electrical schemes that determine the used current by the sensors are shown.

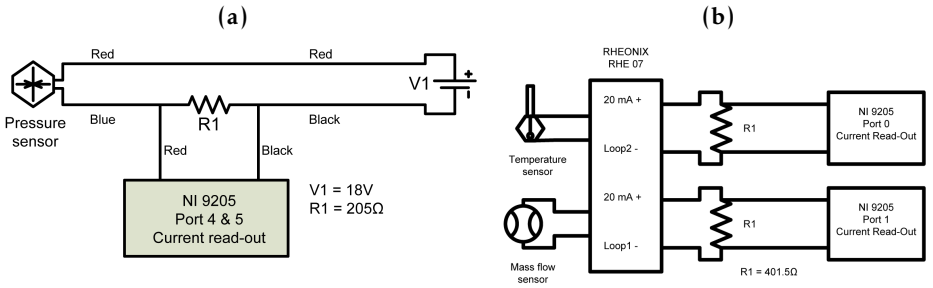

Figure 3.11: *Electrical schemes to read out the pressure (3.11a) and the RHEONIX flow temperature and mass flow (3.11b).*

3.3.2 Labview

A Labview read-out program has been developed from the basic program that existed. Upgrades that have been made are the new user lay-out, which besides showing a diagram of the blown system with the appropriate sensors on the right spot, also has five graphs that show in real time the temperature of the sensors attached to the tube, the other temperature sensors, the mass flow and the pressure sensors. Colors indicate if a temperature sensor is working (green/red), furthermore the system detects and displays if a CO_2 bottle is used (gray in CO_2 bottle turns green), if a fluid is flowing in the system (the balk between temperature sensors turns blue) and an indicator glows when a current is applied over the tube. A general overview of the front panel interface is depicted in Figure 3.12.

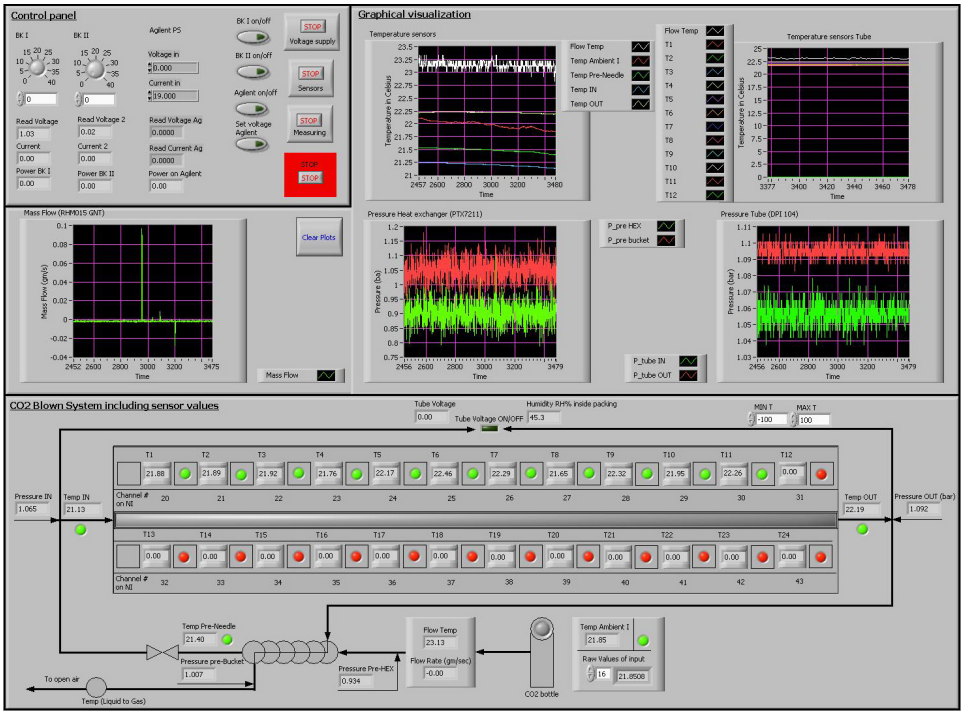

Figure 3.12: *Labview front panel interface with on the upper right the power supply controls, adjacently graphs are placed. At the bottom a schematic view of the blown system including sensors values is visible.*

A special control program for the Agilent power supply has been written. Besides giving control over the device, it also includes safety software: if one of the sensors measures a temperature above 80 $°C$ it shuts the power down. Furthermore, when the applied power becomes higher than 80 W an approval has to be given by the user. Finally, a lot of minor improvements have been made, e.g. better structure, more sensors, safety indicators and writing the acquired data to a file.

3.3.3 Matlab

A Matlab program has been written to analyze the data taken by Labview. The heat transfer coefficient and thermal impedance are calculated for tubes and prototypes stave, respectively, using the calculations as presented in section 3.4. Furthermore, the program compares the calculated heat transfer coefficient with the CO_2 prediction models of *Thome et al.* [13, 14], and the pressure drop with the pressure drop models. It also determines the flow pattern maps and calculates relevant points in the pressure enthalpy diagram. Finally, it saves all the related graphs to the computer. A short manual to add a new measurement to the program and to analyze that file can be found in Appendix E.

Simulation program

A tunable simulation program based on the models by *Thome et al.* has been constructed during the programming of the DAQ Matlab program. A Matlab GUI that allows easy access to the simulation models has been developed, and is depicted in Figure 3.13.

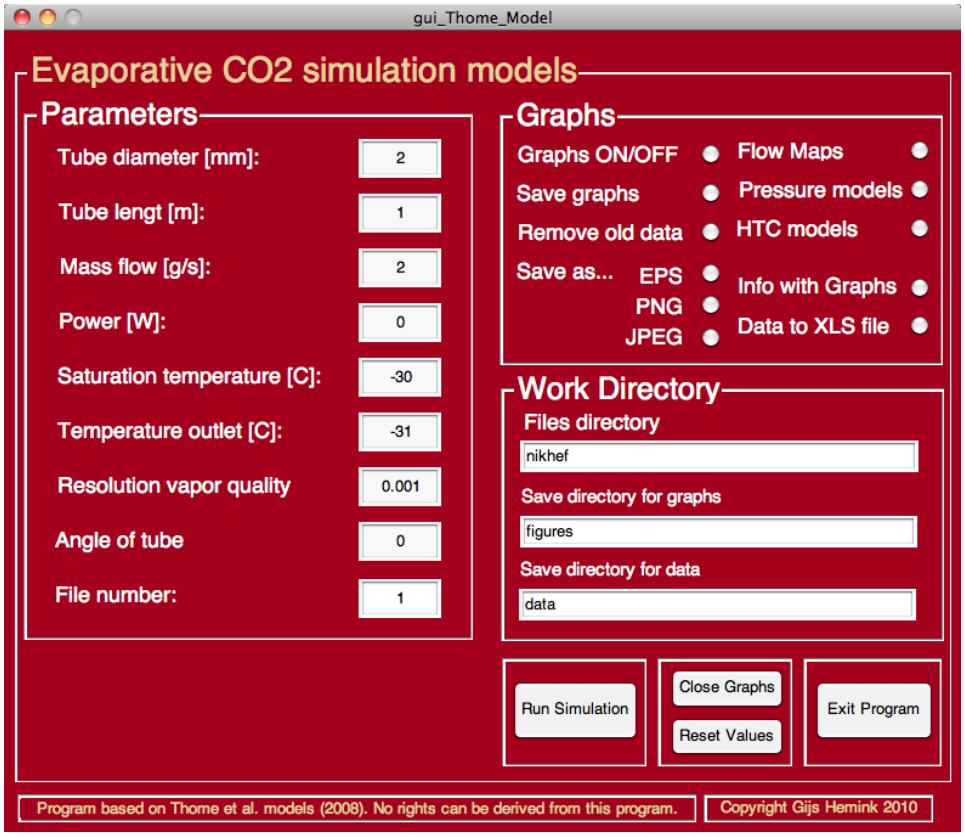

Figure 3.13: *GUI: Based on vaporative CO_2 simulation models. It allows the simulation of a tube with specific inner diameter and length which is cooled by evaporative CO_2.*

On the left side of the GUI it possible to fill in all the simulation characteristics of real experiments . On the right side optional choices are possible concerning presenting the data in graphs, save the graphs (up to three different formats), and save the raw data to files on the hard drive. The save directories can easily be altered in the box *Work Directory*, and at the bottom it is possible to reset the values, close the graphs, close the program, and most of all start the simulation. The version presented in Figure 3.13 is MAC based, but also a windows version has been created, which has the same possibilities.

3.4 Measurements Approach

The final goal of this work is to measure the thermal impedance of the stave and verify if the present design is compatible with the thermal runaway requirement. To reduce the errors it has been decided to measure independently the thermal impedance of the conductive part of the stave with water at room temperature, while the heat transfer coefficients of boiling CO_2 have been measured by means of bare tubes of different diameter. To validate the DAQ system and the algorithm for the bare tubes, measurements of the heat transfers coefficients of water at room temperature have been performed and compared with the analytical relationship available in literature.

3.4.1 Measuring the heat transfer coefficient of CO_2

Control measurement

Before the heat transfer coefficient of CO_2 is measured, a control measurement for every tube, using water at various temperatures (15, 20 25 °C), takes place. By applying different heat fluxes the heat transfer coefficient is determined in the same way as will be explained in the description of the CO_2 measurement. Subsequently, this is compared with the theoretical heat transfer coefficient prediction of water to see if it agrees. If so, CO_2 measurements can commence.

CO_2 measurement

When Equation 2.5 is used to calculate the heat transfer coefficient of CO_2, the temperature difference between the coolant and inner tube wall has to be measured under various heat fluxes, coolant temperatures and mass velocities. Multiple temperature sensors are therefore attached along the test tube to measure the outside wall temperature.

The tubes' wall works as a resistor around the coolant creating a temperature difference between the two wall sides of the tube, as is depicted in Figure 3.14.

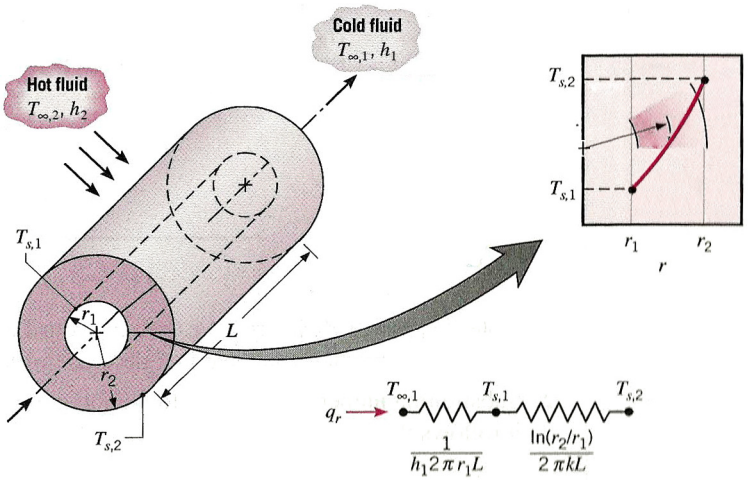

Figure 3.14: *Hollow cylinder with convective surface conditions. Here a cold fluid flows through the tube, thereby absorbing heat that is applied on the outside wall of the tube by a warmer fluid. (Courtesy of [19]).*

The temperature on the inside of the tube is lower, as can be seen on the top right. A simple view on this situation is the analogue with an electric circuit as is done on the lower right of Figure 3.14: here heat represents the transported current; temperature difference, the voltage; and the tube's wall, the resistor. In experiments a current I is applied on the outside wall of the tube. This wall works as a resistor creating a temperature gradient perpendicular through the tube's wall, as is described in Equation 3.1 were the gradient is calculated [19].

$$\Delta T_w = \frac{Q \ln(r_o/r_i)}{2\pi k l} \tag{3.1}$$

With r_o and r_i the outer and inner radius $[m]$ of the tube.

Subtracting the value calculated with Equation 3.1 from the measured temperature results in the inner wall temperature. Measuring the pressure at the inlet and the outlet of the test area enables the calculation of the fluids temperature along the tube by linear interpolation between the two measured values. This is possible because evaporating fluids maintain a specific pressure at a given temperature, as is shown in Figure 3.15.

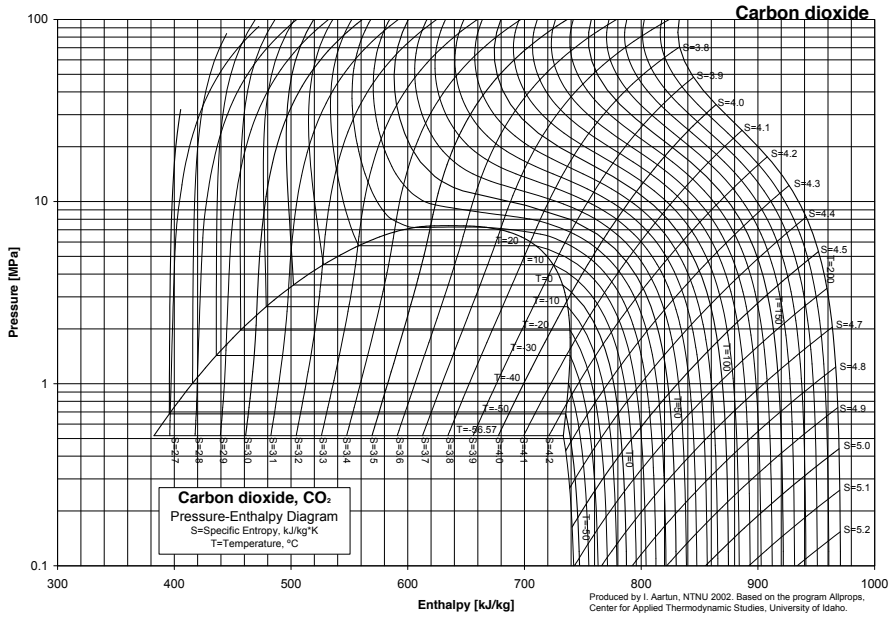

Figure 3.15: *Pressure-Enthalpy diagram with correlation between pressure and temperature inside the parabola: fixed pressure equals fixed temperature.*

The effective power, Q Equation 3.2, applied over the test tube can be determined by reading out the current and multiplying the square product of I with the temperature correct resistance, which can be calculated with Equation 3.3.

$$Q = I^2 \cdot R(T) \tag{3.2}$$

Here I is the current $[A]$ and $R(T)$ the temperature dependent resistance $[\Omega]$ as represented in Equation 3.3,

$$R(T) = R_{ref}\left[1 + \alpha \cdot \left(T - T_{ref}\right)\right] \tag{3.3}$$

which is deduced from the *Bloch-Grüneisen* formula [27] for a resistances R at temperature T with a reference resistance R_{ref} at T_{ref} and α a material constant $[°K^{-1}]$.

3.4.2 Measuring the thermal impedance

The thermal impedance of a prototype stave is determined with Equation 2.4, using water as coolant. The effective power Q can be determined in the same way as done in subsection 3.4.1, but now has to be divided by the surface area ($A = \pi \cdot D_i \cdot l$) to calculate the power density q. The temperature difference between a sensor and the outer tube wall cannot be

measured directly. Equation 3.4 approaches this another way using Equation 2.5, making it possible to calculate $\Delta T_{s,w}$, and subsequently, the thermal impedance.

$$\Delta T_{s,w} = \Delta T_{s,f} - \Delta T_{w,f} = \Delta T_{s,f} - \frac{Q}{\pi D_i h_{water} l} \tag{3.4}$$

Temperature sensors are placed on top of the prototype pixel sensors to measure their temperature on various places along the stave. The fluid temperature is determined by linear interpolation of the temperature between two temperature sensors that are placed inside the pressure sensors (they are in direct contact with the coolant). From a theoretical point of view Equation 2.6 can also be used, because the coolant temperature at the inlet of the stave is known from the chiller. The pressure sensors cannot be exploited in this case because a mono phased fluid is used. A correction for the wall thickness has to be made, as is presented in subsection 3.4.1 using Equation 3.1: this is done to calculate the outer wall temperature from the inner wall temperature otherwise the thermal impedance of the tube is included with the thermal impedance of the Carbon Foam. Finally, h_{water} can be determined as is described in subsection 2.2.1 using the characteristics of water (based on NIST database [28]) at the local fluid temperature.

3.4.3 Measuring the heat transfer coefficient of CO_2 using staves

The heat transfer coefficient of CO_2 inside tubes can also be determined using the prototype stave when the thermal impedance of the foam is known. Rewriting Equation 3.4 using Equation 2.4 results in Equation 3.5. This makes it possible to subtract interfering variables, thereby reducing the situation as if the sensors where placed on the outer wall of the tube inside the prototype stave.

$$\Delta T_{w,f} = \Delta T_{s,f} - R_{CF} \cdot q \tag{3.5}$$

Here $\Delta T_{s,f}$ can be measured experimentally as explained in the previous section. This can then be implemented in the general formula for the cylindrical heat transfer coefficient, this then results in Equation 3.6.

$$h_{CO_2} = \frac{Q}{\pi D_i l \left(T_{s,f} - R_{CF} \cdot q \right)} \tag{3.6}$$

In this chapter the results of the measurements done on the IBL stave with water and on the bare tubes with evaporative CO_2 are described. In Appendix C an overview of the tubes properties and the taken measurements can be found; the main results are presented in the following paragraphs.

4.1 Thermal Impedance

4.1.1 Thermal impedance IBL pixel prototype stave

The thermal impedance has been measured as described in subsection 3.4.2, by ten temperature sensors attached along the pixel prototype stave. Using water at temperatures of 15, 20 and 25 °C while applying a power around 0, 32, 48, 64 or 80 W, the thermal impedance under 20 different experimental conditions has been determined. The result of two single measurements are shown in Figure 4.1 and in Figure 4.2 a graph combining four measurements is presented.

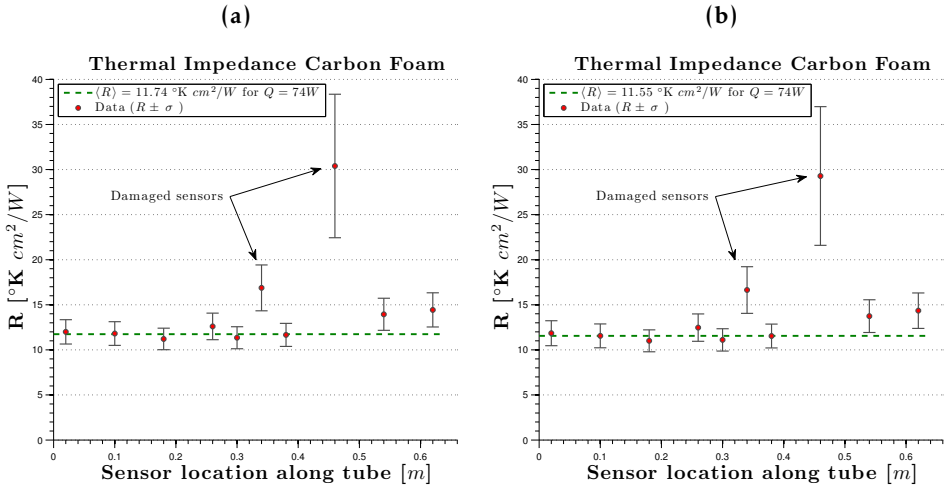

Figure 4.1: *Thermal impedance of IBL prototype stave, measured with ten temperature sensors along the tube at two different temperatures, $T = 10$ °C (4.1a), 20 °C (4.1a). In both measurements the sensors dissipated 74 W. The green line indicates the average value based on sensors 1 to 5 and sensor 7. The other sensors are found to be damaged or influenced by the damaged sensor. The data points and corresponding errors are plotted in red and black, respectively.*

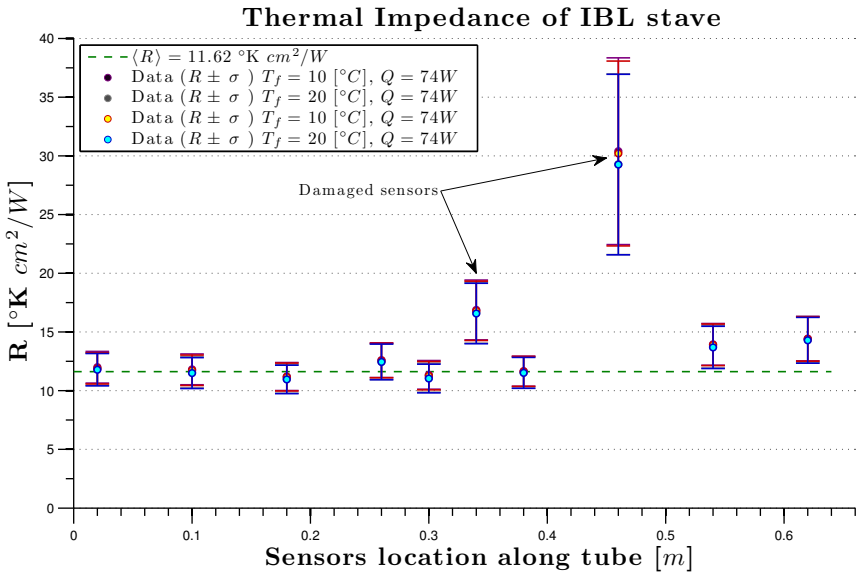

Figure 4.2: *Measurement of the thermal impedance of the Carbon Foam used in the IBL pixel prototype stave. In the four measurements the sensors all dissipated 74W while the fluid temperature differed. The average value, $R = 11.62\ °Kcm^2/W$, is represented by the green line. In this calculation the damaged sensors are not taken into account.*

The thermal impedance measured at the positions of the damaged sensors is not taken into account to evaluate the average R along the stave.

The calculated average value is $R = 11.62\ °Kcm^2/W$ while the theoretical value calculated with finite element analysis is $R = 5\ °Kcm^2/W$. The discrepancy can be explained mainly by the defects introduced by the gluing process at the various interfaces tube-foam and foam-sensor.

4.1.2 Carbon Foam – Tube Interface

A small portion of a few millimeters along the stave length has been cut away with the purpose to visually inspect the cross section. Two photographs (see Figure 4.3) show a large hole below the tube. The contact between foam and tube is there reduced, thus increasing thermal impedance. It has been noted in addition that the fraction of the tube in contact with foam presents imperfections and voids, which make the thermal contact ineffective and far from the ideal condition normally simulated with finite element models.

(a) Front view of Carbon Foam with 2 *mm* tube sticking out.

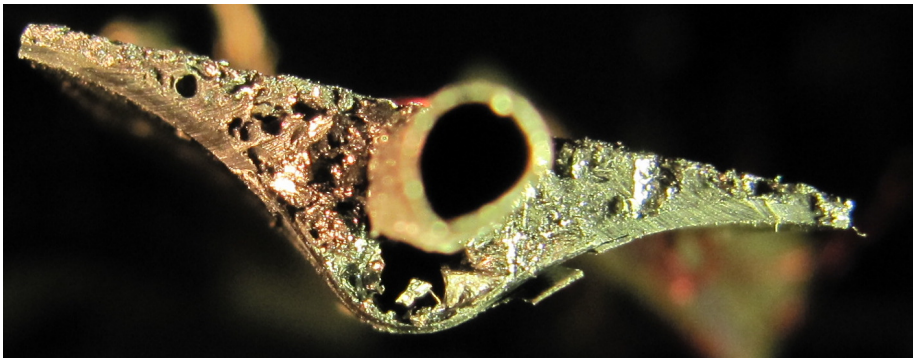

(b) Front view at an angle of 45 ° on the damaged area (stave is placed upside down).

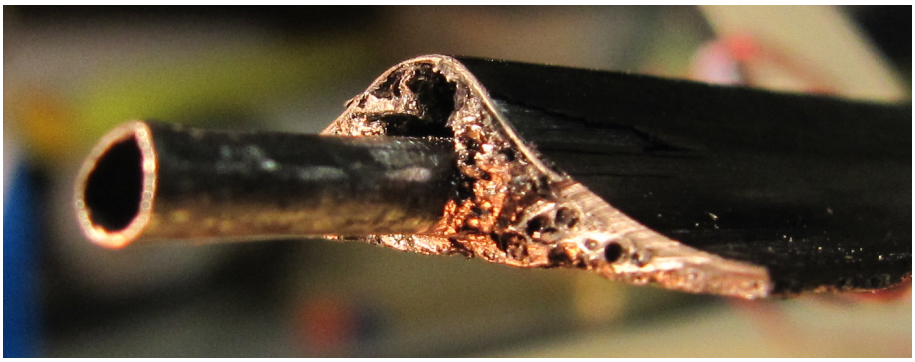

Figure 4.3: *Cross-section of the IBL prototype stave while it was under repair. In both graphs a hole in the Carbon Foam is visible around the tube, which reduced the contact between the tube and foam, therefore increases the thermal resistance from the sensor to tube.*

Besides the bad contact between tube and foam also two heaters were found to be de-attached. The thermal impedance on those places is higher because additional thermal resistors influence the measurements. This results in a increase of the local thermal impedance without changing the material properties of the Carbon Foam, therefore the damaged sensors are not taken into account in subsection 4.1.1.

4.2 Heat Transfer Coefficients of Evaporative CO_2

The heat transfer coefficient of CO_2 has been determined for four different tubes. Before these measurements could commence, first the heat transfer coefficient of water has been measured using these tubes to see if the theoretical prediction for the heat transfer coefficient of water could be reproduced. This has also been done to see if the data acquisition system

worked accurately. These results are presented first, then the results concerning evaporative CO_2 and the ATLAS phased upgrades are shown.

4.2.1 Introduction

Four different tubes, all with a length around 1500 mm, are used to measure the heat transfer coefficient of both water and CO_2. Three are made of Stainless Steel (SS) but differ in inner diameter and wall thickness. 6 sensors are attached along each of these tubes to measure the outer wall temperature when a heat flux is applied. The fourth tube is made out of Titanium (Ti) and has 10 temperature sensors connected along the tube. Titanium is the material used in the prototype staves, but is difficult to handle in experiments, therefore stainless steel has been used. In the next section the tubes are called SS RW-12, SS RW-14, SS Swagelok an Ti RW-14, with inner diameters of $D_i = 2.16\ mm$, $D_i = 1.6\ mm$, $D_i = 4.57\ mm$ and $D_i = 1.6\ mm$, respectively. More characteristics of the tubes can be found in Appendix C.

4.2.2 Water

The heat transfer coefficient of water has been determined using water at different temperatures while applying different heat fluxes on the tubes. For each fluid temperature (15, 20, 25 $°C$) an effective power between 0 and 300 W has been dissipated in the tube. The mass flow has been kept constants per tube because this was regulated by the used chiller, and thus dependent on the tubes diameter. The results of these measurements are presented below.

In Figure 4.4 the results for the SS RW-12 tube are presented, followed by the measurements taken with the SS RW-14 tube in Figure 4.5, and the SS Swagelok tube (Figure 4.6). Finally, in Figure 4.7 measurement taken with the Ti RW-14 tube are presented.

In all the graphs the heat transfer coefficient is plotted versus the position of the temperature sensors along the tube. The green dotted line is the theoretical prediction made with the Gnielinski equation as is explained in subsection 2.2.1. The red dots are the measured values including, in black, the measurement errors.

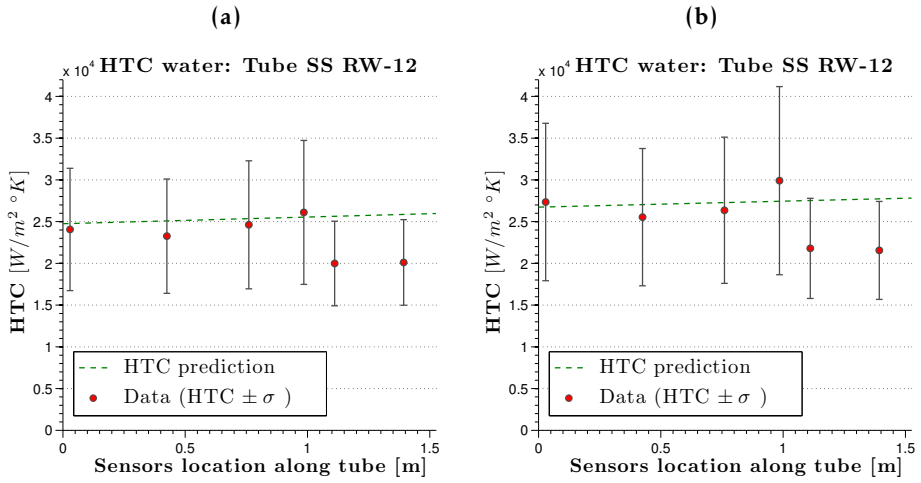

Figure 4.4: *Heat transfer coefficient results for water taken with the SS RW-12 tube of* $D_i = 2.16$ *mm. In 4.4a* $T_{fluid} = 15\,°C$ *and* $Q_{eff} = 171$ *W, in 4.4b* $T_{fluid} = 20\,°C$ *and* $Q_{eff} = 172$ *W. For both graphs* $\dot{m} = 21$ *g/s. Large errors arise due to the temperature sensors used. The results show that an indication for the heat transfer coefficient of water can be made.*

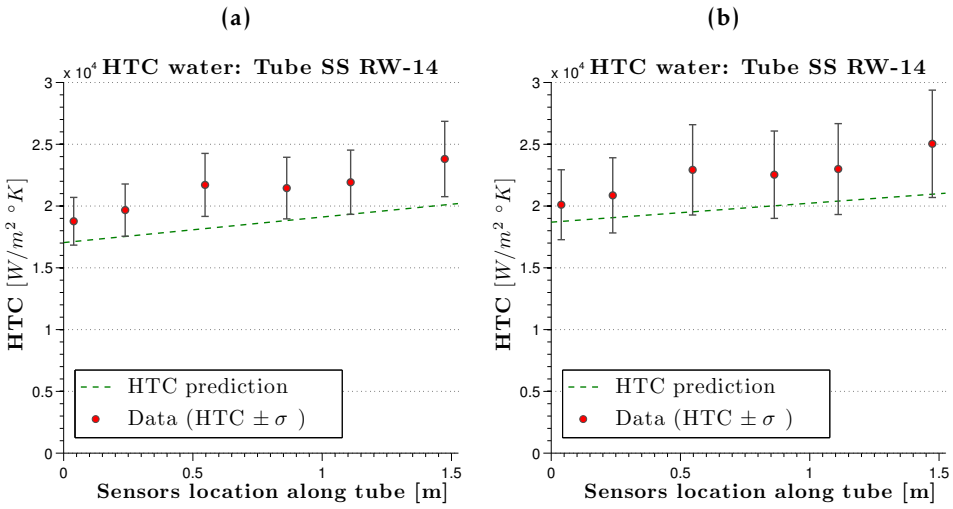

Figure 4.5: *Heat transfer coefficient results for water taken with the SS RW-14 tube of* $D_i = 1.6$ *mm. In 4.5a* $T_{fluid} = 15\,°C$ *and* $Q_{eff} = 307$ *W, in 4.5b* $T_{fluid} = 20\,°C$ *and* $Q_{eff} = 235$ *W. For both graphs* $\dot{m} = 7.75$ *g/s. The results again show that an indication for the heat transfer coefficient of water can be made.*

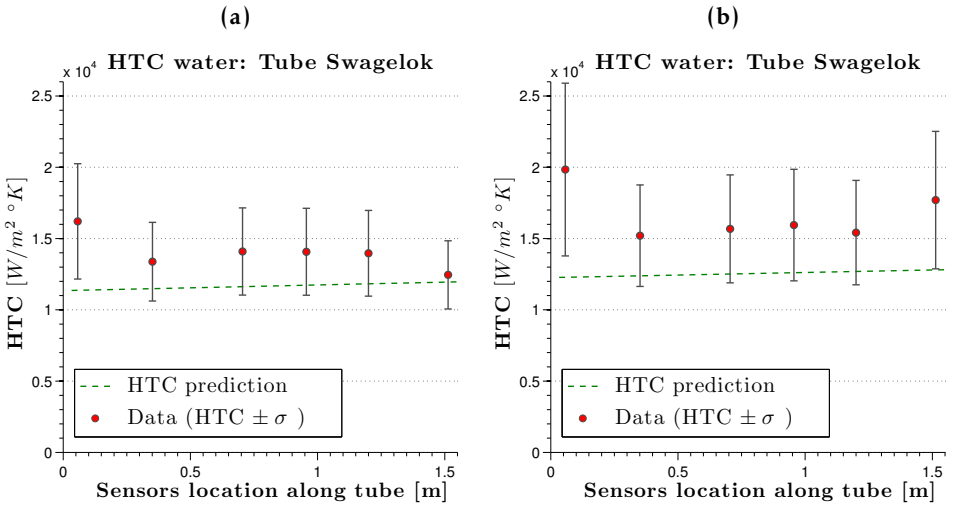

Figure 4.6: *Heat transfer coefficient results for water taken with the SS Swagelok tube of D_i = 4.57 mm. In 4.5a T_{fluid} = 15 °C and Q_{eff} = 297 W, in 4.5b T_{fluid} = 20 °C and Q_{eff} = 297 W. For both graphs $\dot{m}$ = 43 g/s. The results again show that an indication for the heat transfer coefficient of water can be made.*

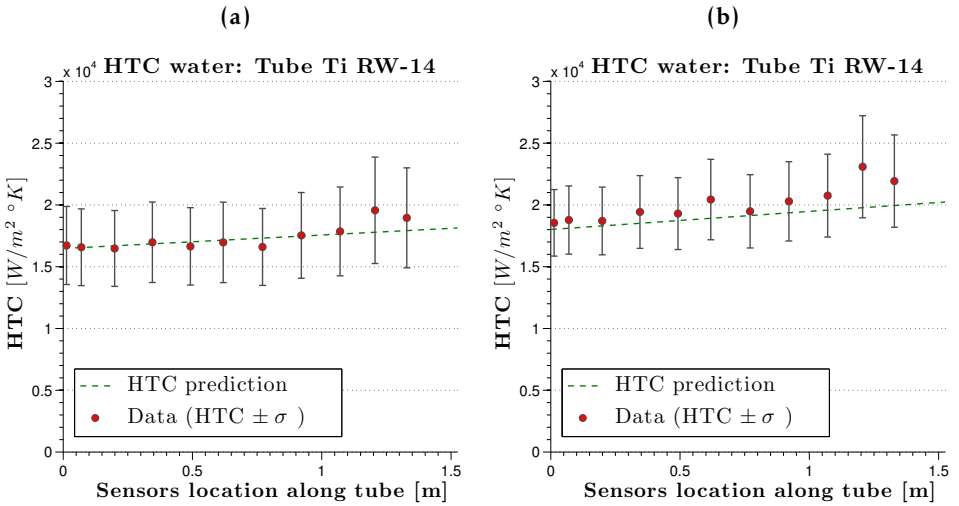

Figure 4.7: *Heat transfer coefficient results for water taken with the Ti RW-14 tube of D_i = 1.6 mm. In 4.5a T_{fluid} = 15 °C and Q_{eff} = 143 W, in 4.5b T_{fluid} = 20 °C and Q_{eff} = 208 W. In both graphs $\dot{m}$ = 7.5 g/s. The results show that an indication for the heat transfer coefficient of water can be made, and thus that the experimental set-up functions appropriately.*

Summary

The results are in agreement with the theoretical prediction of the heat transfer coefficient of water. The accuracy of the blown system has been designed for the use of CO_2, therefore reproducing these water results has not been done with high precision. However, even with this low accuracy, the results fall within an order of magnitude, repeating a measurement is possible. This shows that the blown system and DAQ systems function appropriately.

4.2.3 CO_2

Measuring the CO_2 heat transfer coefficient is carried out in the same way as with water. Besides varying the heat flux and fluid temperature, the influence of the mass flow (between 1 and 5 g/s) is now also investigated. This creates multiple variables, therefore the strategy is to fix a certain mass flow with the needle valve and use the pressure regulator to set the fluid temperature (between -45 and -15 $°C$). If this is succeeded, a heat flux over the tube is applied. Then, when the cooling system reaches an equilibrium, a higher heat flux is applied. This is repeated until dry-out is reached. As can be found in Appendix C, the heat transfer coefficient has been determined for a total of 110 different situations. This is more data that can be presented here, therefore only the most interesting results and data concerning the ATLAS phased upgrade is presented in the following paragraphs.

In Figure 4.8 to Figure 4.11 the results for the SS RW-12 tube are presented. In Figure 4.12 to Figure 4.14 the results for the SS RW-14 tube can be found and the Swagelok tube data is presented in Figure 4.16 to Figure 4.17. Finally the data taken with the Ti RW-14 tube is presented in Figure 4.19 to Figure 4.22.

In all graphs the heat transfer coefficient is plotted against the vapor quality of the fluid. The green line is the theoretical prediction based on the model of *Thome et al.* [13, 14]. This model predicts the heat transfer coefficient with an accuracy of 30%. The measured data is plotted with red dots surrounded with black error bars.

Data SS RW-12

The presented results concerning the SS RW-12 tube, in Figure 4.8 to Figure 4.11, compare the influence of the applied heat flux: the left picture has a low power density, while the right picture has a high power density applied to the tube. The temperature and mass velocity are kept constant per set of graphs.

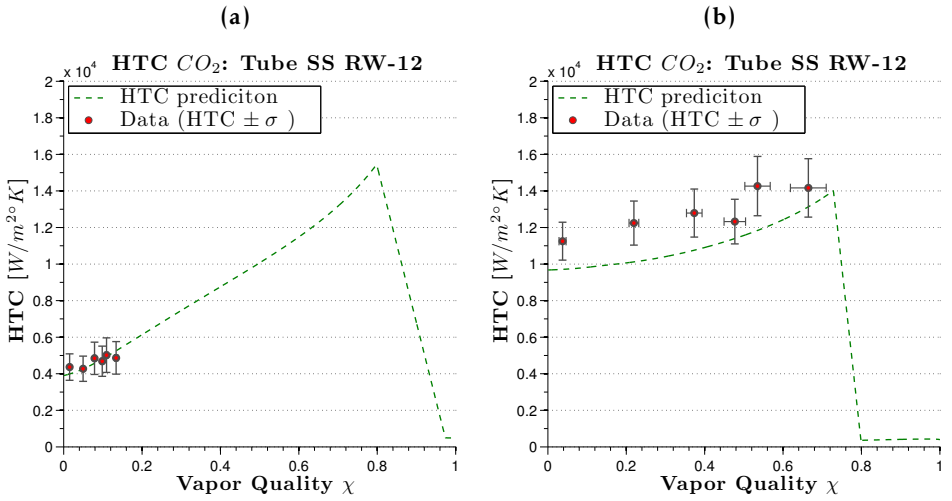

Figure 4.8: *Comparison of the predicted Heat Transfer Coefficients to the experimental data taken with the SS RW-12 tube of $D_i = 2.16$ mm at low and high applied heat fluxes. In 4.8a $G = 382.4\ kg/m^2s$, $q = 5.07\ kW/m^2$ and $T_{sat} = -19.8\ °C$. In 4.8b $G = 353.6\ kg/m^2s$) and $T_{sat} = -18.7\ °C$. Only the applied heat flux differs from 4.8a, which is a factor of 5 higher, $q = 24.5\ kW/m^2$, in 4.8b. This results in a higher average and more flat heat transfer coefficient in the region before dry-out. But, the vapor quality at which dry-out start decreases from 0.8 to 0.725, furthermore the highest value in 4.8b is lower then in 4.8a. The data points follow the theoretical prediction adequately.*

In Figure 4.8 the influence of the applied heat flux is evidently noticeable. The heat transfer coefficient is more flat at a higher heat flux, this results in a better and more stable heat transfer. Furthermore, especially at low vapor quality the increase is enormous (factor of 2.5), while the maximum heat transfer coefficient remains the same. In Figure 4.9 the same measurement has been repeated only now at a lower saturation temperature.

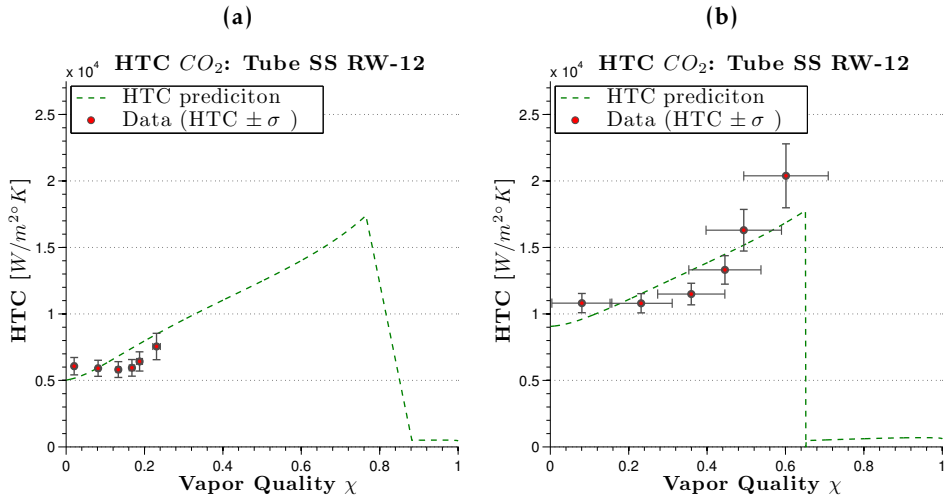

Figure 4.9: *Comparison of the predicted Heat Transfer Coefficients to the experimental data taken with the SS RW-12 tube of D_i = 2.16 mm at low and high applied heat fluxes. In 4.9a $G = 400.6\ kg/m^2s$, $q = 10.3\ kW/m^2$ and $T_{sat} = -32.3\ °C$, simulation the refrigerating properties of the phased upgrade. In 4.9b $G = 468.7\ kg/m^2s$ and $T_{sat} = -35.1\ °C$. Hence, the values are the same as in 4.9a, with only the heat flux a factor of 3 higher, $q = 30.3\ kW/m^2$. The data points again follow the theoretical prediction adequately.*

The graphs in Figure 4.9 again show that the model predicts the heat transfer coefficient adequately. The same changes in the heat transfer coefficient that are noticed in Figure 4.8 due to an increasing heat flux are visible. There is a higher average heat transfer coefficient in the region before dry-out, and a heat transfer coefficient increase of a factor of 2 at low vapor quality is also noticeable. The vapor quality at which dry-out starts decreases with the same amount as in Figure 4.8, from 0.725 to 0.65. Finally, the decline of the heat transfer coefficient at point of dry-out becomes faster at higher heat fluxes. This can be explained when the corresponding flow maps are compared, as is done in Figure 4.10.

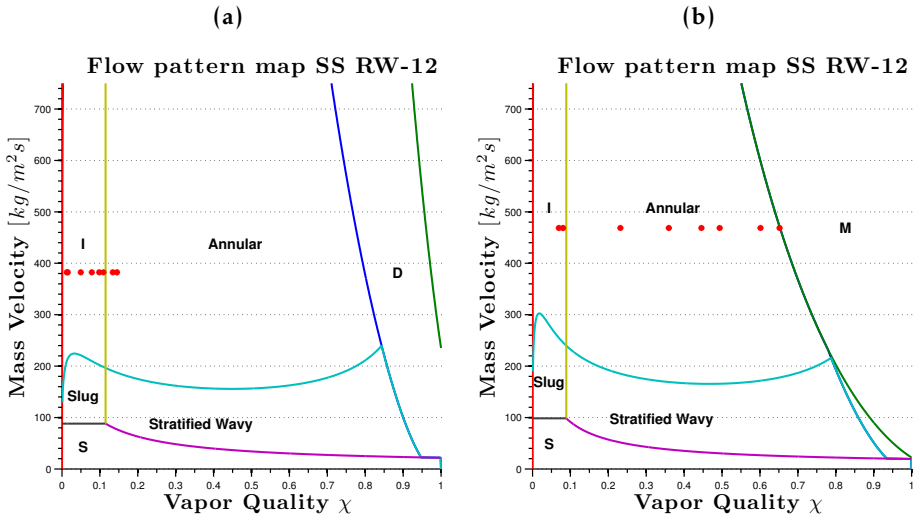

Figure 4.10: *Comparison of the flow maps corresponding, with 4.8a in the left graphs, and 4.8b in the right graph. I is the Intermittent flow, D is the Dry-out region and M is Mist flow.*

In 4.10a a low heat flux is applied at a saturation temperature of $-15\ ^{\circ}C$. Although the vapor quality only just reaches a value corresponding with annular flow it is visible that at high vapor quality (which would have been reached if the tube would have been much longer) first dry-out and then mist flow arises. In 4.10b a large heat flux is applied at a saturation temperature of $-35\ ^{\circ}C$, where the vapor quality reached is just at the border between annular and mist flow. This time there is no dry-out region due to the high heat flux. In the heat transfer coefficient graphs this is noticeable by the steep decline of the coefficient.

Figure 4.9 corresponds with the application circumstances for the Outer Pixel characteristics. It seems to be that it may not be possible to use CO_2 as coolant for this phased upgrade under the now know design properties. The heat flux in 4.9b is lower than the maximum heat flux that will be applied on the stave, while dry-out point is now already reached.

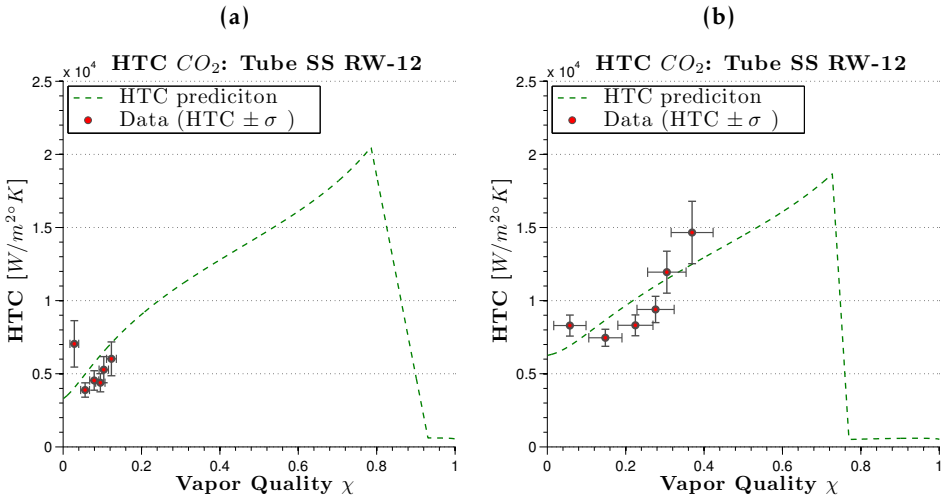

Figure 4.11: *Comparison of the predicted Heat Transfer Coefficients to the experimental data taken with the SS RW-12 tube of D_i = 2.16 mm at low and high applied heat fluxes. In 4.11a G = 439.5 kg/m^2s, q = 5.3 kW/m^2 and T_{sat} = −39.6 °C. In 4.11b G = 432 kg/m^2s and T_{sat} = −39.3 °C). They are the same as in 4.11a, but the heat flux is a factor 3 higher, q = 17.1 kW/m^2. Again an increase in the average heat transfer coefficient in the region before dry-out is visible. The data points again follow the theoretical prediction adequately.*

In Figure 4.11, an even colder temperature is reached and the same increase in average heat transfer coefficient before the dry-out point is visible as with the two previous graphs. Although this increase is less than at higher temperatures. In all three sets of data, higher heat fluxes do not result in higher heat transfer coefficients at dry-point. Furthermore, if the three left graphs of Figure 4.8 to Figure 4.11 are compared, it is visible that when the saturation temperate declines the heat transfer coefficient at dry-out point increases. Although, this also could be explained by the variations of mass velocities.

Data SS RW-14

For the SS RW-14 tube the same comparison is first made as is done with the data of the SS RW-12 tube. When this is in agreement with the previous section conclusions about the influence of the heat flux on the heat transfer coefficient can be deduced.

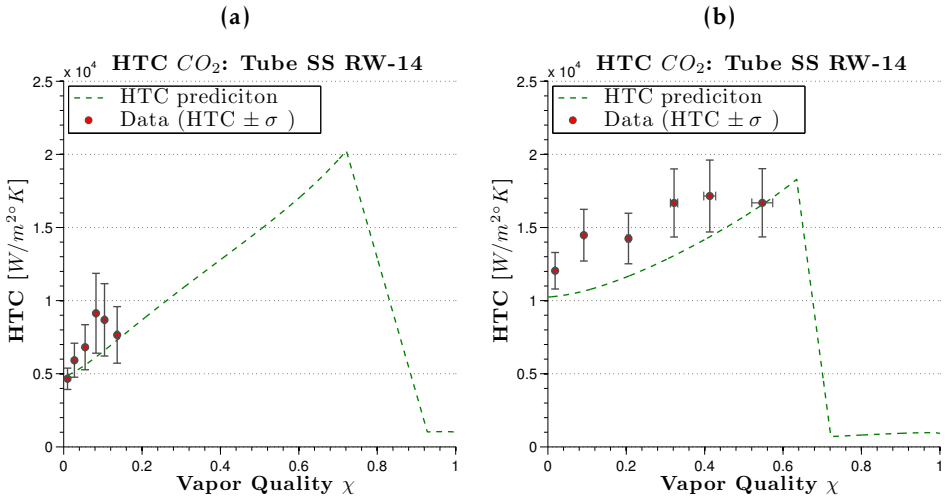

Figure 4.12: *Comparison of the predicted Heat Transfer Coefficients to the experimental data taken with the SS RW-14 tube of D_i = 1.6 mm for low and high applied heat flux. In 4.12a G = 632.7 kg/m^2s, q = 6 kW/m^2 and T_{sat} = −14 °C. In 4.12b G = 610.1 kg/m^2s and T_{sat} = −14 °C. The heat flux is a factor 4 higher, q = 24.1 kW/m^2. The same behavior as with the SS RW-12 tube is visible: the average heat transfer coefficient at low vapor quality increases a factor of 2. Furthermore, considering that the green line has a 30% variation, the data points again follow the theoretical prediction adequately.*

Figure 4.12 shows the same behavior as in Figure 4.8 to Figure 4.11: a higher average and more flat heat transfer coefficient in the region before dry-out and a decrease in the maximum coefficient when a higher heat flux is applied. Hence, the model predicts the influence of the heat flux on the heat transfer coefficient accurately.

In Figure 4.13 two different measurements made with the same experimental set up values are presented to show the repeatability of the experiments. Although this is the only coinciding data that has been produced during the CO_2 experiments, the consistency is noteworthy. In Figure 4.14 the influence of the mass velocity is investigated while keeping the saturation temperature and heat flux the same.

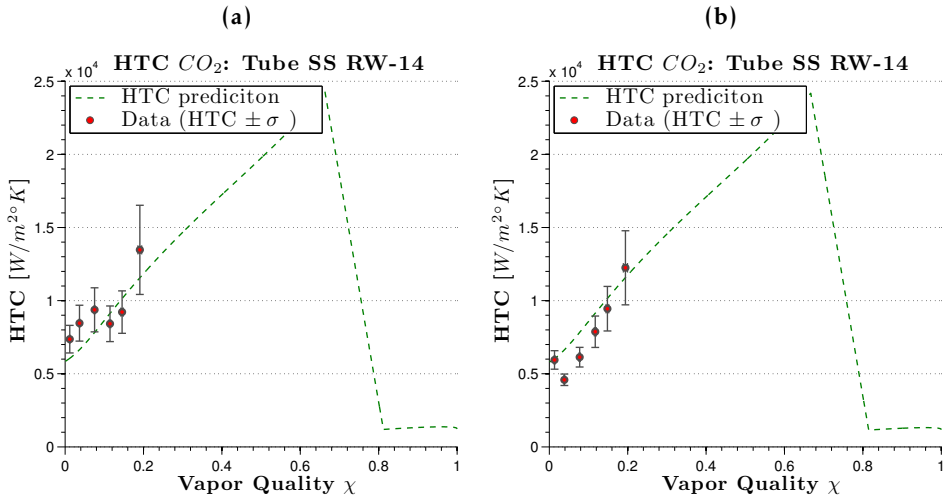

Figure 4.13: *Comparison of the predicted Heat Transfer Coefficients to the experimental data taken with the SS RW-14 tube of $D_i = 1.6$ mm for two different measurements at the same experimental settings. In 4.13a $G = 754.5$ kg/m^2s, $q = 11$ kW/m^2 and $T_{sat} = -24.5$ °C. In 4.13b $G = 739.6$ kg/m^2s, $q = 10.9$ kW/m^2 and $T_{sat} = -24.9$ °C. The experimental set up values are the same, and corresponds excellent each with other.*

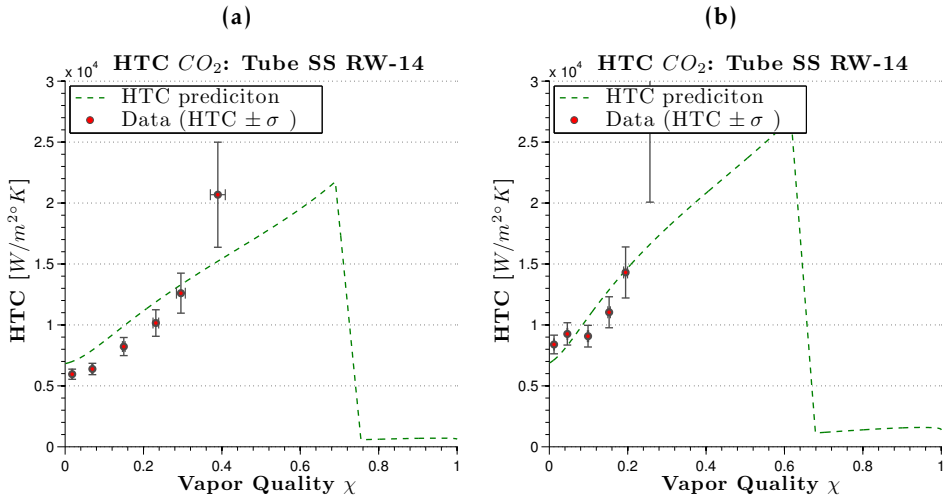

Figure 4.14: *Comparison of the predicted Heat Transfer Coefficients to the experimental data taken with the SS RW-14 tube of $D_i = 1.6$ mm, while variating the mass velocity. In 4.14a $G = 546.4$ kg/m^2s, $q = 17.5$ kW/m^2 and $T_{sat} = -32.5$ °C. In 4.14b $G = 824.4$ kg/m^2s, $q = 17.4$ kW/m^2 and $T_{sat} = -33$ °C. The influence of the increasing mass velocity is dominant. The maximum heat transfer coefficient increases from 22000 to 27000 $W/m^{2\circ}K$ while the vapor quality of the data points at the same saturation temperature and the same applied heat flux decreases.*

The influence of the mass velocity is clearly visualized in Figure 4.14: the maximum heat transfer coefficient increases and the vapor quality at the outlet of the tube declines. This implies that at a higher mass velocity the applied heat flux can be increased without reaching dry-out, if taken into account that dry-out is reached at a lower vapor quality.

Data SS Swagelok

The SS Swagelok tube with an inner diameter of $D_i = 4.57\ mm$ has only been measured with low mass velocities. This is because the blown system is not capable of providing mass flows higher than 5 g/s. Therefore, the fluid in the tube is stratified instead of annular flow. As a result, only the bottom of the tube is in contact with liquid, while the top of the tube is in contact with vapor (when the vapor quality is larger then zero). The temperature sensors are placed at the bottom of the tube to measure the maximum heat transfer coefficient. Hence, this means that the measured value should be higher than the predicted coefficient because the bottom side of the tubes stays covered with liquid.

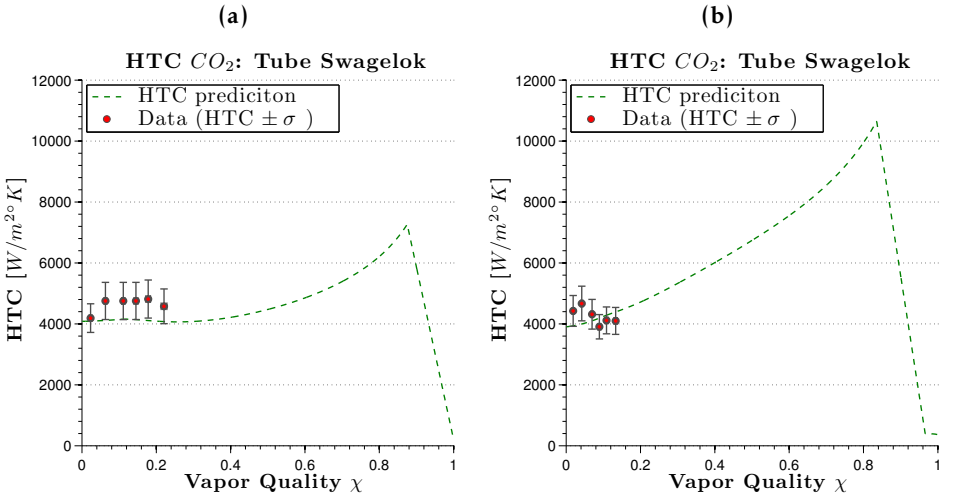

Figure 4.15: *Comparison of the predicted Heat Transfer Coefficients to the experimental data taken with the SS swagelok of $D_i = 4.57\ mm$ for low applied heat flux while varying the mass velocity and saturation temperature. In 4.16a $G = 144.3\ kg/m^2s$, $q = 6.68\ kW/m^2$ and $T_{sat} = -27.7\ °C$. In 4.16b $G = 243.9\ kg/m^2s$, $q = 6.75\ kW/m^2$ and $T_{sat} = -32.5\ °C$. The data corresponds with the analytical models.*

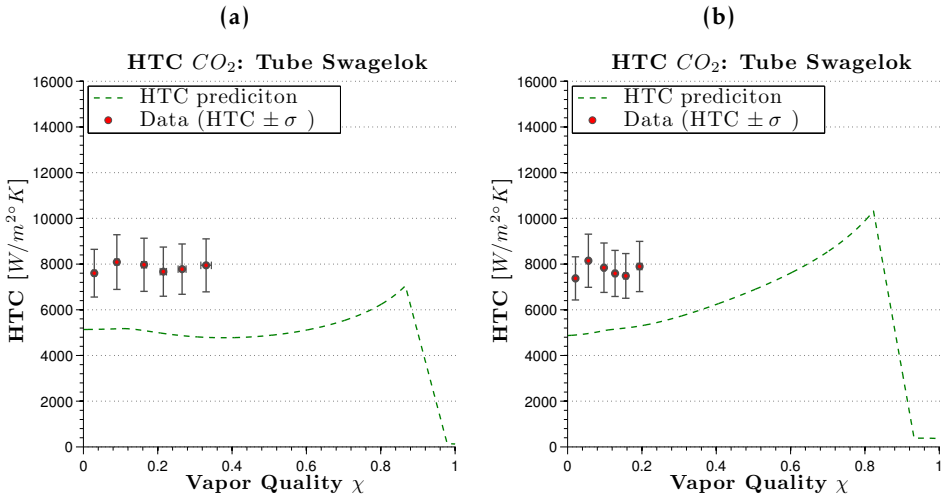

Figure 4.16: *Comparison of the predicted Heat Transfer Coefficients to the experimental data taken with the SS swagelok of D_i = 4.57 mm for medium applied heat flux while varying the mass velocity and saturation temperature. In 4.16a G = 140.5 kg/m^2s, q = 9.9 kW/m^2 and T_{sat} = −27.5 °C. In 4.16b G = 239 kg/m^2s, q = 10 kW/m^2 and T_{sat} = −33 °C. The data falls outside the theoretical prediction, which is expected from the stratified wavy flow in the tube.*

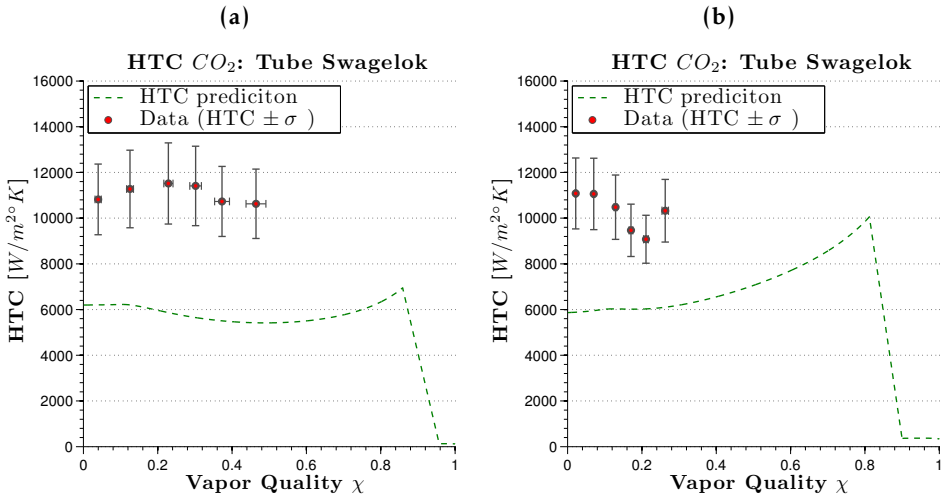

Figure 4.17: *Comparison of the predicted Heat Transfer Coefficients to the experimental data taken with the SS swagelok of D_i = 4.57 mm for medium applied heat flux and varying the mass velocity and saturation temperature. In 4.17a G = 137 kg/m^2s, q = 13.6 kW/m^2 and T_{sat} = −27.1 °C. In 4.17b G = 235.6 kg/m^2s, q = 13.8 kW/m^2 and T_{sat} = −32.8 °C. Although again a deviation between prediction and experimental data is visible the shape of the prediction can also be found in the data.*

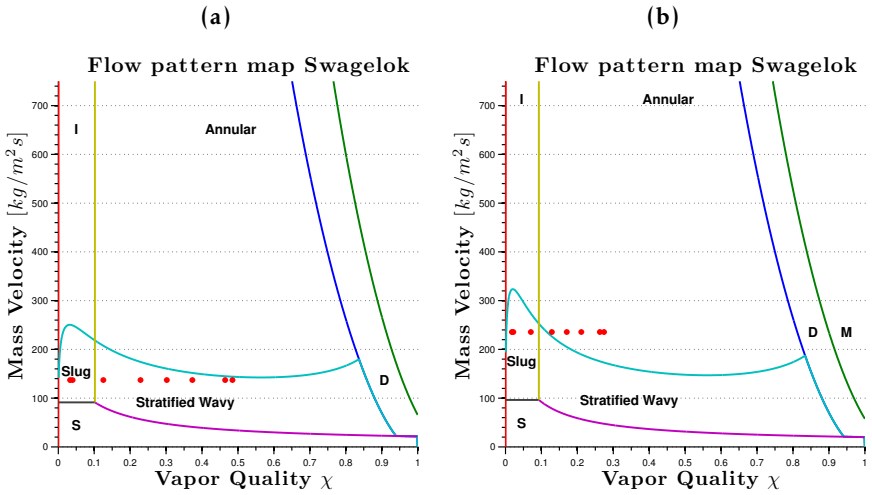

Figure 4.18: *Flow maps corresponding with 4.17a (4.18a) and 4.17b (4.18a). Annular flow is not reached in 4.18a and only barely in 4.18b. The mass velocity is thus too low to guarantee that the whole inside wall of the tube will be covered with liquid.*

In the figures the measured heat transfer coefficient surpasses the theoretical value. This was expected, as explained in the introduction of this section. At low heat flux, Figure 4.15, the results almost correspond with the model. When a higher heat flux is applied the deviation increases, but also follows the profile of the green line. When 4.16b and 4.17b are compared with each other a small decline of the maximum heat transfer coefficient is found. The changing parameter is the applied heat flux.

The two flow maps in Figure 4.18 are the corresponding maps with the heat transfer coefficient graphs of Figure 4.17. It is visible that the patterns predict that annular flow is only barely reached at the used mass velocities. Therefore, stratified flow will be dominant. Liquid will stay on the bottom side because its density is high: vapor with a much lower density will form on top.

Data Ti RW-14

The Ti RW-14 tube has the same characteristics as the SS RW-14 tube, except that it is made out of titanium instead of stainless steel. Therefore, first a comparison between the both tubes is made. The same results should be produced, because in the calculation of the heat transfer coefficient the influences of the wall has been corrected for. Secondly, data that compares the influence of the applied heat flux, mass velocity and temperature is presented.

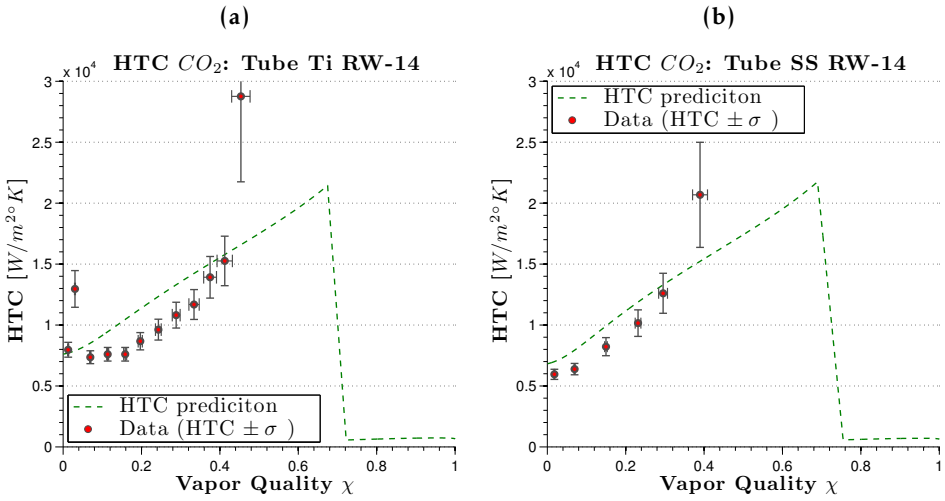

Figure 4.19: *Comparison of the predicted Heat Transfer Coefficients to the experimental data taken with the Ti RW-14 and SS RW-14 tube both with D_i = 1.6 mm. Although the experimental values differ slightly: for 4.19a G = 556.9 kg/m^2s, q = 20.7 kW/m^2 and T_{sat} = −31.2 °C; while for 4.19b G = 546.4 kg/m^2s, q = 17.5 kW/m^2 and T_{sat} = −32.5 °C. In both graphs the measured data corresponds with the predicted model, although in both graphs a preemptive incline in the heat transfer coefficient is visible.*

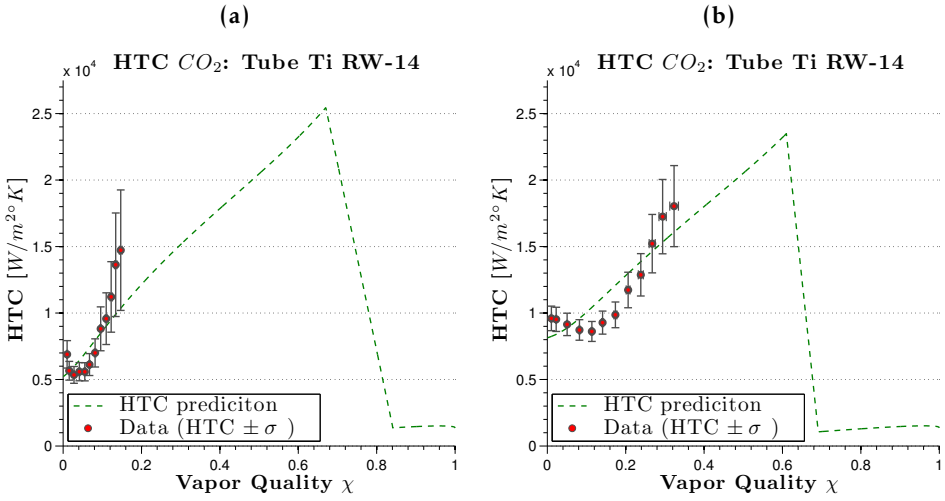

Figure 4.20: *Comparison of the predicted Heat Transfer Coefficients to the experimental data taken with the Ti RW-14 of D_i = 1.6 mm for low and high applied heat flux. In 4.20a G = 792.1 kg/m^2s, q = 8.73 kW/m^2 and T_{sat} = −24.7 °C. In 4.20b G = 792.2 kg/m^2s, q = 19.9 kW/m^2 and T_{sat} = −23.8 °C.*

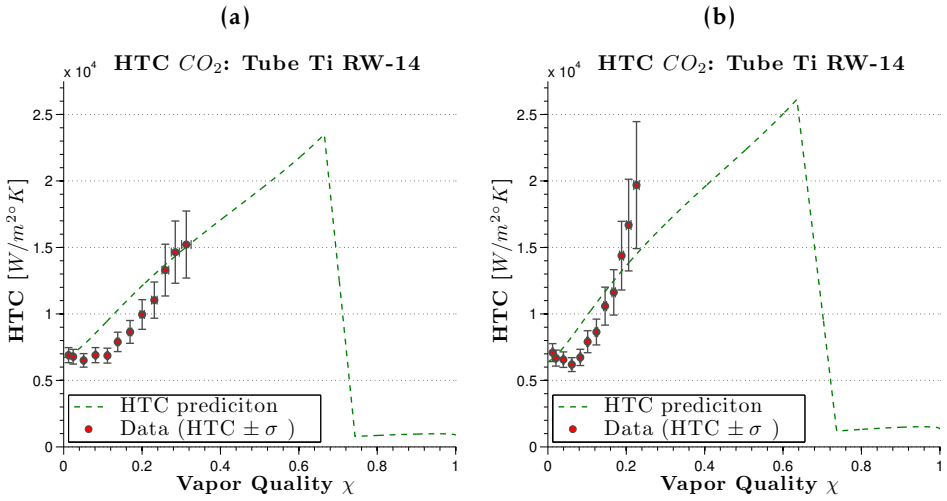

Figure 4.21: *Comparison of the predicted Heat Transfer Coefficients to the experimental data taken with the Ti RW-14 of $D_i = 1.6$ mm for different mass velocities. In 4.21a $G = 646.6\ kg/m^2s$, $q = 16.4\ kW/m^2$ and $T_{sat} = -31.2\ °C$. In 4.21b $G = 802.5\ kg/m^2s$, $q = 14.4\ kW/m^2$ and $T_{sat} = -30\ °C$.*

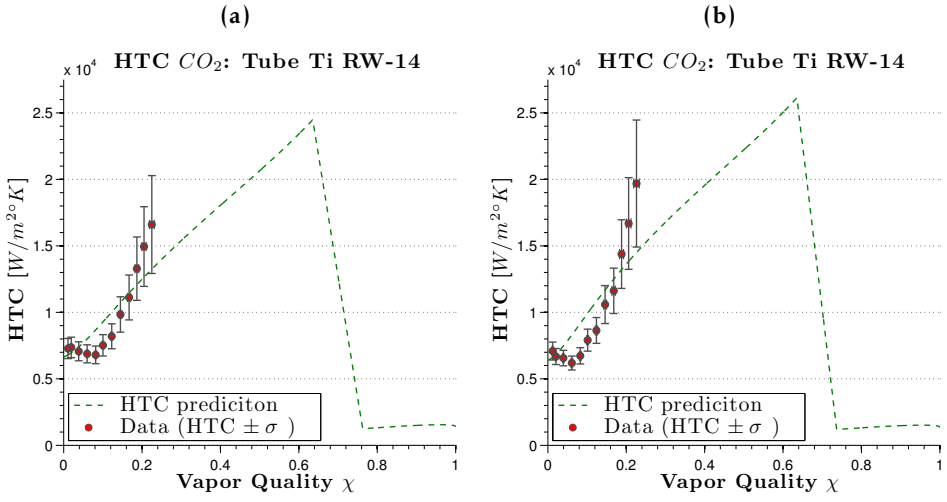

Figure 4.22: *Comparison of the predicted Heat Transfer Coefficients to the experimental data taken with the Ti RW-14 of $D_i = 1.6$ mm for different saturation temperatures. In 4.22a $G = 801.9\ kg/m^2s$, $q = 13.8\ kW/m^2$ and $T_{sat} = -24.3\ °C$. In 4.22b $G = 802.5\ kg/m^2s$, $q = 14.4\ kW/m^2$ and $T_{sat} = -30\ °C$.*

As expected no deviation due to the tubes material is visible in Figure 4.19, this implies that Titanium is the more suitable material to use

because of its favorable thermal conductivity. On the opposite side stands the welding problem. In the experiments the connectors at the inlet and outlet of the tube are glued to the Titanium tube, while the connectors on the stainless steel tubes have been welded. The latter provides a better and more solid solution, making stainless steel an easier material to handle.

In Figure 4.20 the influence of the heat flux is investigated. The measurement again confirms the behavior of the heat transfer coefficient of CO_2. When the heat flux increases the average heat transfer coefficient increases while the maximum coefficient declines and is found at a lower vapor quality.

In Figure 4.21 the influence of different mass velocities is investigated. The influence is mainly visible in the increase of the maximum heat transfer coefficient. Furthermore the vapor quality at which dry-out occurs decrease slightly.

In Figure 4.22 the influence of different saturation temperatures is investigated. When the saturation temperature becomes lower than the maximum heat transfer coefficient increases while the start value at zero vapor quality and the point of dry-out remains the same.

If the tubes are mutually compared then the influence of the tubes diameter becomes visible. A smaller tube results in a higher heat transfer coefficient if all the experimental values stay the same. This is because in a smaller tube the mass velocity increases, which is not a problem because in the total picture less material is needed (reduction in the tubes material) reducing the chance of multiple scattering.

4.2.4 Summary CO_2 results

The *Thome model* seems to predict the heat transfer coefficient for CO_2 at low saturation temperatures in small diameter tubes adequately.

The implications of this model are:

1. Higher heat fluxes result in a higher average heat transfer coefficient, especially at low vapor quality the increase can be a factor of two. The maximum heat transfer coefficient, at point of dry-out, decreases while the point of dry-out is reached at a lower vapor quality.

2. Higher mass velocity results in a higher heat transfer coefficient, therefore the vapor quality at the outlet decreases. This is for a part compensated because the dry-out point starts at a lower vapor quality. The maximum heat transfer coefficient is not influenced.

3. Lower evaporation temperature results in a higher heat transfer coefficient, without influencing the maximum coefficient and the start of the dry-out.

4. Thinner tubes result in a higher heat transfer coefficient for CO_2 compared with thicker tubes at the same mass flow, saturation temperature and applied heat flux.

4.3 Temperature Gradient

The temperature gradient along the tube has to be stable (within 3 $°C$ [10]), therefore the temperature difference has been measured. The results are presented below for all tubes at different heat fluxes. Because CO_2 is evaporating, the fluctuations on the temperature difference between wall and fluid translate directly back to the temperature gradient along the tube.

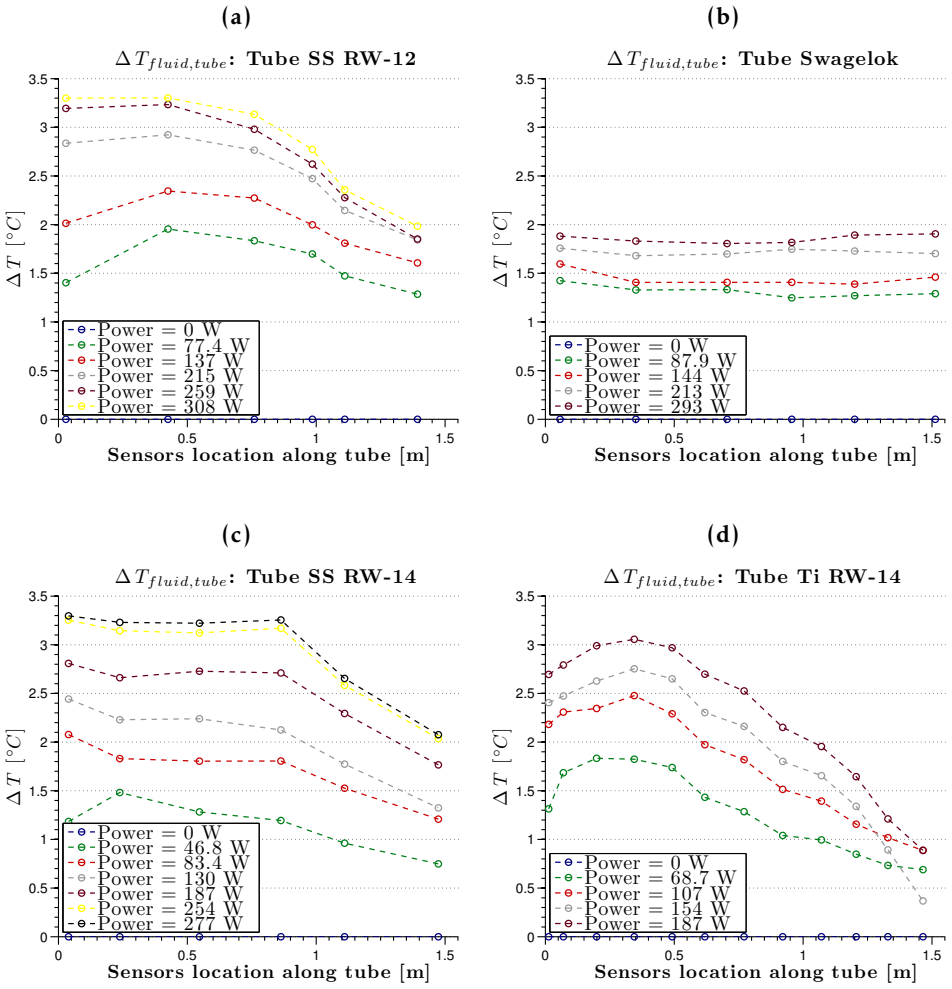

Figure 4.23: *Temperature difference between the fluid and outer wall of the tube. Visible in all graphs is the small temperature decline over the tube. which is caused by an increasing heat transfer coefficient and the pressure drop along the tube. In 4.23a* $\dot{m} = 1.8$ *g/s and* $T_{sat} = -34$ *to* -24 *(from low to high Q), in 4.23b* $\dot{m} = 2.3$ *g/s and* $T_{sat} = -30$*, in 4.23a* $\dot{m} = 1.5$ *g/s and* $T_{sat} = 28$ *and in 4.23a* $\dot{m} = 1.6$ *g/s and* $T_{sat} = -28$*. The influence of the tube its material, as far as can be seen from only one single graphs, is negligible.*

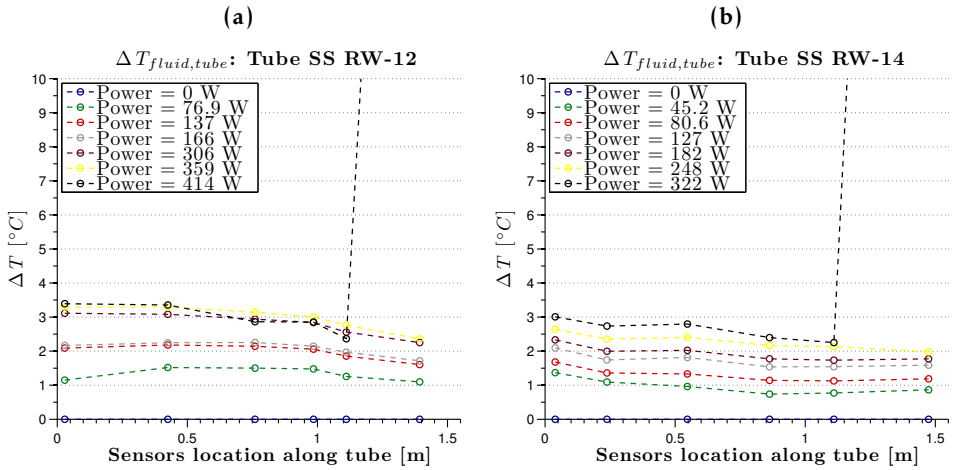

Figure 4.24: *Two graphs which show the temperature difference between the fluid and outer wall of the tube. In both graphs dry-out is reached: the black line, which represents a high heat flux, rises rapidly. The cooling at that point is not sufficient enough anymore, resulting in a rapid incline of the local temperature. In 4.23a* $\dot{m} = 2$ *g/s and* $T_{sat} = -30$ *to* -24 *(from low to high Q), in 4.23b* $\dot{m} = 1.3$ *g/s and* $T_{sat} = -13$.

Hence, CO_2 has a very small temperature gradient along tubes. For tubes of 1500 *mm* a temperature difference between inlet and outlet of 1.5 $°C$ has been measured. This is lower than the design specification and it also implies that for the phase I upgrade, where the tubes are 840 *mm*, this is even lower (shorter tube equals less pressure drop, hence a lower temperature drop). Furthermore, it can be concluded that at higher heat fluxes the gradient along the tube increases until dry-out is reached. Then the temperature on the wall explodes. For the phase II upgrade this implies that the measurements confirm that the design of the staves lies on the outer range where CO_2 can be used as coolant.

4.4 Pressure Drop

The pressure drop along the tube is for a large part accountable for the temperature drop along the tube. The pressure drops have been measured and are presented in Figure 4.25 for the SS RW-14 and Ti RW-14 tubes, in which the influence of the material is observed, and in Figure 4.26 the pressure drops in the other two tubes can be found.

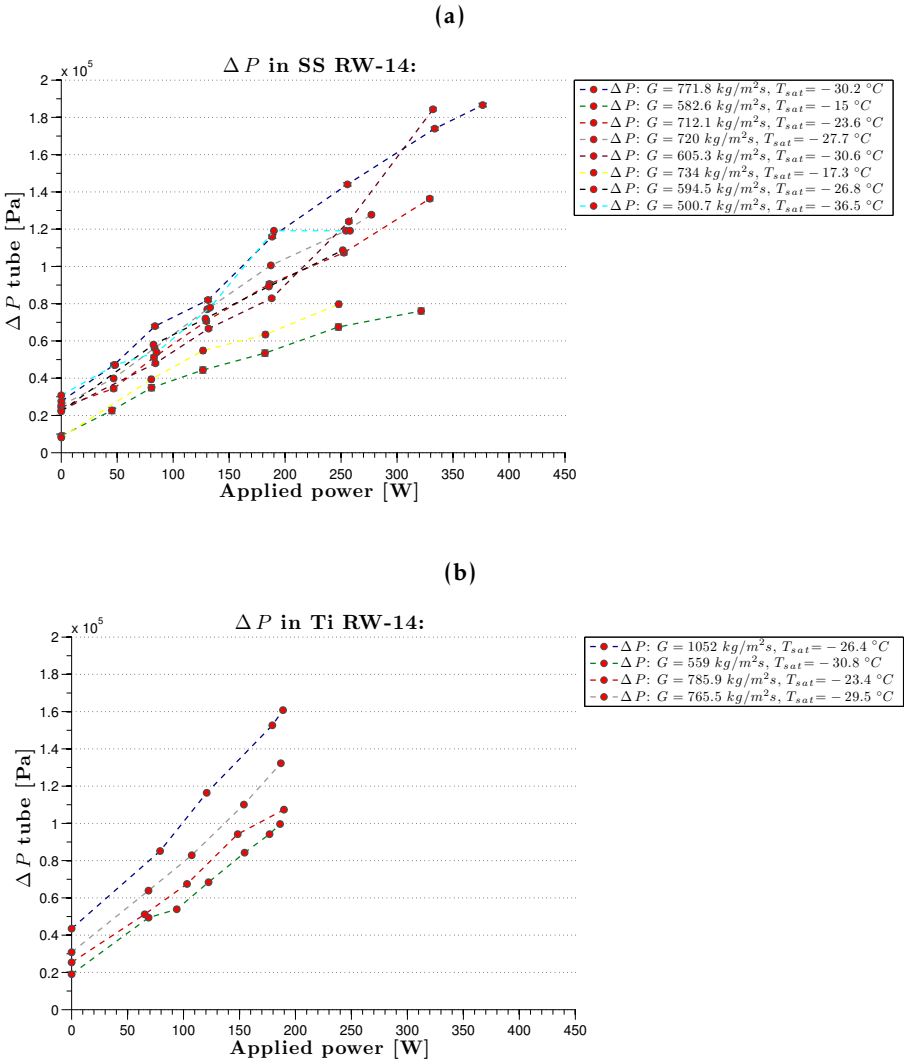

Figure 4.25: *In 4.25a (SS RW-14) and 4.25b (Ti RW-14) the pressure drop in the tube is plotted against the applied effective power. All data points taken for both tubes are plotted. The blue (4.25a) and the gray line (4.25b) can be compared directly with each other: no influence between the two different tube materials have been found.*

The results in Figure 4.25 show large similarities. The values of the blue (4.25a) and the grey line (4.25b) for example can be compared because they are measured under the same mass velocity and heat flux. The have the same slope and pass through the same data points. The other values also show no noticeable deviations. Hence, no influence of the tubes material has been found.

The pressure drop is influenced by the saturation temperature and the mass velocity. When the saturation temperature of the coolant becomes

twice as cold the pressure drop almost doubles. This is visible in 4.25a when the green and black line are compared. The strong influence on the pressure drop by the mass velocity is visible when the black line in 4.25a is compared with the blue line in 4.25b. There, at $T_{sat} \approx 26.5\ ^{\circ}C$, the mass velocity doubles, and as a result the pressure drop almost becomes twice as high. Furthermore, the increase is linear with an offset depending only on the mass velocity, while the slope depends on the mass velocity and the saturation temperature.

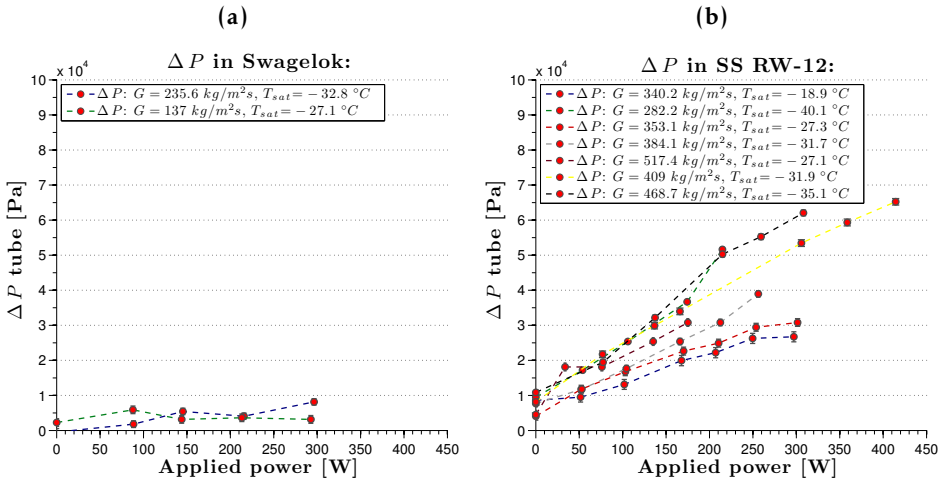

Figure 4.26: *In 4.26a and 4.26b the pressure drop in the tube of the Swagelok and SS RW-12 tube, is plotted against the applied effective power, respectively. The influence of the tube its diameter is clearly visible; a thinner tube results in a higher pressure drop.*

Comparing the results from Figure 4.26 is difficult because the diameter of the tubes are different. However, the different cross-sections of the tube also influences the tube clearly. A tube with smaller inner diameter has a higher pressure drop. The cross-section of the tubes are 2.01, 3.80, 16.42 mm^2 for the SS RW-14 and Ti RW-14; SS RW-12 and SS Swagelok tube, respectively. Although not enough data has been gathered to compare the tubes' cross-section to determine if there is relationship between the cross-section and the pressure drop, a factor of three is found between the green line in 4.26b and the black line in 4.25a. This data has been taken at almost the same mass velocity and saturation temperature.

Summary

Overall, the results show a small temperature drop over the tube due to the pressure drop. In the region −40 to −20 $^{\circ}C$ the temperature drop is $\sim 1\ ^{\circ}C\ Bar^{-1}$, see Figure 3.15. The low drop is due to the low viscosity of the liquid

CO_2 at low vapor quality. When a heat flux is applied the pressure drop increases because the vapor quality increases. This results in a larger temperature drop along the tube, especially when dry-out is reached, because only then vapor is leaving the tube. The highest pressure drop measured is, 1.9 *Bar*. This data has been taken when an effective power of 370 W was applied at a mass velocity of 771.8 kg/m^2s at a saturation temperature of $-30.2\ ^\circ C$ in the SS RW-14 tube. The resulting saturation temperature drop along the tube due to the pressure drop is $1.9\ ^\circ C$. One preferable consequence is that the temperature decreases along the tube, hence the coolant temperatures are not negatively compromised by this effect.

4.5 Infrared Camera

To see what happens with the coolant and a small diameter tube while applying a power on the tube an infrared camera has been position above the test area. Subsequently, a measurement has been done with the isolation box open. A movie has been made of the period in which water at $T = 15\ ^\circ C$ starts flowing, subsequently a power has been applied, then the coolant flow is interrupted, and finally the coolant flow is resumed. In Figure 4.27 four pictures showing these situations are presented.

(a) Tube with the coolant flowing.

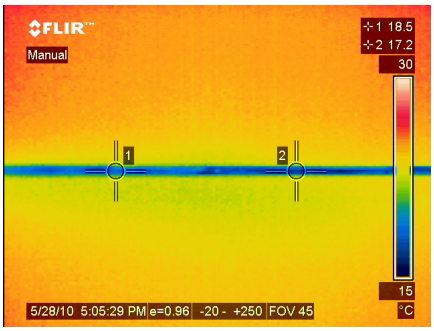

(b) Tube with coolant flowing with 330 *W* applied.

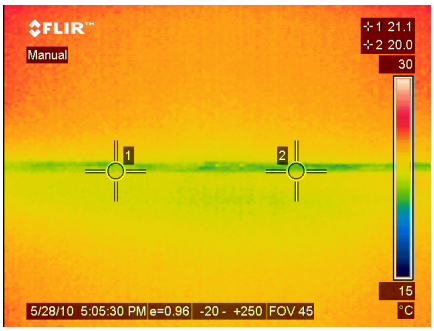

(c) Tube not cooled while 330 *W* is applied.

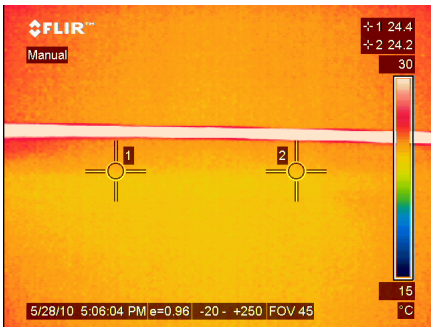

(d) Tube with 330 *W* applied, the cooling is resumed.

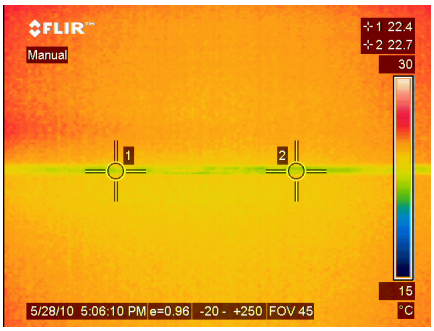

Figure 4.27: *Four snapshot from a infrared camera movie, where first a tube is cooled with water. Subsequently,* 330 *W is applied, then the cooling is paused, and finally the cooling is put back on. The cross 1 and 2 measure the temperature in degrees Celsius and the legend to the right of each picture couples the colors to a temperature scale.*

The first picture, 4.27a, shows a clear uniform cooling of the tube. When a heat is applied (4.27b) the temperature of the tube increases, but stays uniform. Due to the 330 *W* the temperature on the tubes wall increases with 3 °*C*. When the coolant stops flowing a rapid increase of the tubes wall takes place (4.27c). A displacement is also visible: the heat lets the tube expand. Within seconds after the cooling is resumed everything is back to normal (4.27d) and the tubes temperature is the same as in 4.27b.

5 Simulations

5.1 Introduction

Using the results from subsection 4.2.3, which confirm the model of *Thome et al.*, a prediction for the minimum coolant temperature needed in the phased upgrades can be made. Following subsection 3.4.1 the total temperature difference can be calculated using Equation 5.1.

$$q = \frac{Q}{A} = \frac{\Delta T}{\sum R} = \frac{\Delta T_{s,f}}{R_{CF} + R_w + R_f} \tag{5.1}$$

The value for the thermal impedance of the Carbon Foam (R_{CF})is discussed in subsection 4.1.1. The contribution of the tube walls its thermal impedance (R_w) can be found in Equation 3.1, and the relationship between the thermal impedance with the heat transfer coefficient is $R_f = \frac{1}{hA}$. It is then possible to calculate the sensor temperature using Equation 5.2, when the stave is cooled with CO_2 at a specific saturation temperature while a certain heat flux is applied.

$$T_s = Q \cdot \left[\frac{R_{CF}}{w \cdot l} + \frac{\ln r_o/r_i}{2\pi k l} + \frac{1}{h_{CO_2} \pi D_i l} \right] + T_f \tag{5.2}$$

5.2 Refrigerant Temperature for the Phased Upgrade

The tables in the next two sections contain various options to reach a certain sensor temperature for the specific stave: an effective power is used while varying the saturation temperature of CO_2 and the mass flow, which finally results in the sensor temperature. Also the mass velocity, average heat transfer coefficient, vapor quality at the outlet, χ_O, of the tube and the distance, $\Delta\chi_{DO,O}$, between the vapor quality dry-out point and the vapor quality at the outlet can be found in the tables. This represents a value that indicates if the combination of mass flow and saturation temperature for the tube diameter at an effective power can be used to refrigerate the tube. If $\Delta\chi_{DO,O} < 0.1$ then the dry-out point is too close, or in the case $\Delta\chi_{DO,O} < 0$ would already have been reached. The sensor temperature is then represented with $--$ to indicate that this combination is not a usable option. The margin of 0.1 is used because from the experiments it is known that fluctuations arise, being too close to the dry-out point thus would result in an unstable system that risks dry-out. Something that cannot happen in the detectors.

5.2.1 IBL stave for the phase I upgrade

The characteristics of the staves are: $Q_{nom} = 120\ W$, $Q_{max} = 120\ W$, $D_i = 2\ mm$, $D_o = 2.2\ mm$, $l = 840\ mm$, $w = 20\ mm$, $T_s < -15\ °C$ and $1.0 < \dot{m} < 2.0\ g/s$. The titanium tube has a thermal coefficient $k_{tube} = 21.9\ W/m°K$. The thermal impedance of the Carbon Foam has been measured at $R_{CF} = 11.62\ °Kcm^2/W$, however, the value aimed for is $R_{CF} = 5\ °Kcm^2/W$. Therefore, In the tables simulations for both values have been made.

Q $[W]$	T_{sat} $[°C]$	$\dot{m}$ $[g/s]$	**G** $[kg/m^2]$	$\Delta\chi$	$\Delta_{\chi_D - \chi_{max}}$	$< h_{CO_2} >$ $[W/m^{2°}K]$	$T_s\ [°C]$ $R = 11.62$	$T_s\ [°C]$ $R = 5$
80	-25	1.0	318.3	0.473	0.300	8882	-17.69	-20.85
80	-25	1.5	477.5	0.382	0.335	10417	-17.95	-21.10
80	-25	2.0	636.6	0.336	0.335	11973	-18.13	-21.29
80	-30	1.0	318.3	0.564	0.310	9085	-22.73	-25.88
80	-30	1.5	477.5	0.376	0.343	10906	-23.01	-26.16
80	-30	2.0	636.6	0.332	0.342	12708	-23.21	-26.36
80	-35	1.0	318.3	0.455	0.320	9389	-27.79	-30.94
80	-35	1.5	477.5	0.370	0.350	11498	-28.08	-31.23
80	-35	2.0	636.6	0.328	0.347	13546	-28.28	-31.43

Table 5.1: *Simulation results for the IBL prototype stave. The sensor temperature has been calculated for different mass flows and saturation temperatures with CO_2 as refrigerant in a tube of $D_i = 2\ mm$, and a power dissipation of 80 W. Calculations have been done for the measured and the aimed value of the Carbon Foam's thermal impedance. It is assumed that the vapor quality at the inlet of the tube is $\chi_{In} = 0.2$, because then, at the used mass velocities, annular flow can be assumed. $\Delta\chi$ is the vapor quality increase between χ_{in} and χ_{Out} (χ at the inlet and outlet of the tube, respectively), while $\Delta_{\chi_D - \chi_{max}}$ the remaining vapor quality between χ_{Out} and the vapor quality dry-out point.*

For nominal power dissipation CO_2 seems to be an excellent coolant as can be seen in Table 5.1. Already at saturation temperatures of $-25\ °C$ and a mass flow of $1.0\ g/s$ sufficient cooling is reached.

Q $[W]$	T_{sat} $[°C]$	$\dot{m}$ $[g/s]$	**G** $[kg/m^2]$	$\Delta\chi$	$\Delta_{\chi_{D-\chi_{max}}}$	$< h_{CO_2} >$ $[W/m^{2\circ}K]$	T_s $[°C]$ $R = 11.62$	T_s $[°C]$ $R = 5$
120	-25	1.0	318.3	0.609	0.143	10528	-14.44	-19.17
120	-25	1.5	477.5	0.473	0.219	11863	-14.68	-19.41
120	-25	2.0	636.6	0.205	0.238	13266	-14.89	-19.62
120	-30	1.0	318.3	0.595	0.159	10601	-19.46	-24.18
120	-30	1.5	477.5	0.464	0.230	12219	-19.74	-24.47
120	-30	2.0	636.6	0.398	0.247	13872	-19.96	-24.69
120	-35	1.0	318.3	0.583	0.172	10790	-24.49	-29.22
120	-35	1.5	477.5	0.455	0.2401	12695	-24.81	-29.54
120	-35	2.0	636.6	0.392	0.254	14609	-25.04	-29.77

Table 5.2: *Simulation results for the IBL prototype stave. The sensor temperature has been calculated for different mass flows and saturation temperatures with CO_2 as refrigerant in a tube of $D_i = 2$ mm, and a power dissipation of 120 W. Calculations have been done for the measured and the aimed value of the Carbon Foam's thermal impedance. It is assumed that the vapor quality at the inlet of the tube is $\chi_{In} = 0.2$, because then, at the used mass velocities, annular flow can be assumed. $\Delta\chi$ is the vapor quality increase between χ_{in} and χ_{Out} (χ at the inlet and outlet of the tube, respectively), while $\Delta_{\chi_{D-\chi_{max}}}$ the remaining vapor quality between χ_{Out} and the vapor quality dry-out point.*

For maximum power dissipation again CO_2 is an excellent coolant. Although the first entry comes closer to dry-out the cooling is still sufficient. In Figure 5.1 the corresponding heat transfer coefficients of Table 5.3 are shown. With two dots the vapor quality at the inlet and outlet are visualized.

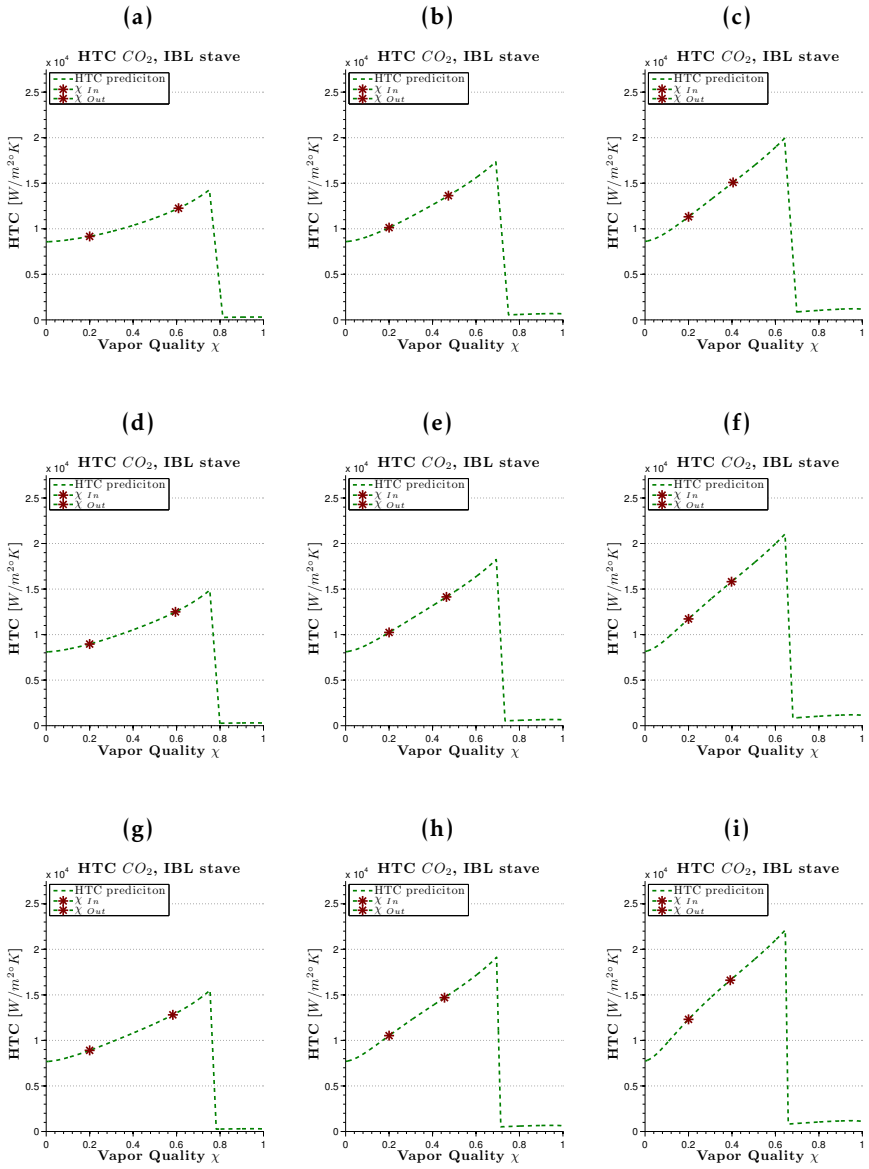

Figure 5.1: *Heat transfer coefficient graphs that correspond with Table 5.3. From top to bottom the temperature decreases in steps of* $-5\ ^{\circ}C$*, and from left to right the mass flow increases in steps of* $0.5\ g/s$*. The two dots represent the vapor quality at the inlet and outlet of the simulated stave.*

The heat transfer coefficient graphs show no dry-out in the operating range, it is therefore interesting to know if also a smaller tube can be used. This would mean a minimization of the material needed that will reduce multiple scattering. In Table 5.3 the situations of Figure 5.1 are repeated only now with a tube of $D_i = 1.5\ mm$.

Q $[W]$	T_{sat} $[°C]$	$\dot{m}$ $[g/s]$	**G** $[kg/m^2]$	$\Delta\chi$	$\Delta_{\chi_D-\chi_{max}}$	$< h_{CO_2} >$ $[W/m^{2\circ}K]$	T_s $[°C]$ $R = 11.62$	T_s $[°C]$ $R = 5$
120	-25	1.0	565.8	0.509	0.134	14067	-14.42	-19.14
120	-25	1.5	848.3	0.373	0.191	15677	-14.64	-19.36
120	-25	2.0	1131.8	0.305	0.196	17264	-14.81	-19.54
120	-30	1.0	565.8	0.495	0.142	14389	-19.46	-24.19
120	-30	1.5	848.3	0.364	0.184	16348	-19.72	-24.44
120	-30	2.0	1131.8	0.298	0.182	18225	-19.91	-24.64
120	-35	1.0	565.8	0.483	0.131	14864	-24.53	-29.26
120	-35	1.5	848.3	0.355	0.168	17180	-24.81	-29.53
120	-35	2.0	1131.8	0.292	0.162	19387	-25.01	-29.73

Table 5.3: *Simulation results for the IBL prototype stave. The sensor temperature has been calculated for different mass flows and saturation temperatures with CO_2 as refrigerant in a tube of $D_i = 1.5$ mm, and a power dissipation of 120 W. Calculations have been done for the measured and the aimed value of the Carbon Foam's thermal impedance. It is assumed that the vapor quality at the inlet of the tube is $\chi_{In} = 0.1$, instead of $\chi_{In} = 0.2$ to increase the region before dry-out. Annular flow can still be assumed. $\Delta\chi$ is the vapor quality increase between χ_{in} and χ_{Out} (χ at the inlet and outlet of the tube, respectively), while $\Delta_{\chi_D-\chi_{max}}$ the remaining vapor quality between χ_{Out} and the vapor quality dry-out point.*

Although the value of $\chi_{In} = 0.1$ is the interface between Intermittent and Annular flow, CO_2 is still an excellent coolant. Hence, it could be an option to reduce the refrigerant tube to 1.5 *mm*, because it meets all the criteria for the IBL upgrade.

5.2.2 Outer Pixel stave for the sLHC

For the sLHC upgrade simulation for the Outer Pixel staves can also be made using Equation 5.2. The characteristics of the prototype stave are: $Q_{nom} = 200\ W$, $Q_{max} = 300\ W$, $D_i = 2\ mm$, $D_o = 2.2\ mm$, $l = 1500\ mm$, $w = 40\ mm$, $T_s < -15\ °C$ and $1.0 < \dot{m} < 2.0\ g/s$. The tube and supporting structure material remain the same, that is, titanium and carbon foam respectively. Therefore $R_{CF} = 5\ °Kcm^2/W$ and $k_{tube} = 21.9\ W/m°K$. The value of R is the value that is reached with finite element methods. However, Carbon Foam at this quality is at the currently not yet fabricated. Because the phase II upgrade is still more than 10 years away it is assumed that R&D will solve the problems that arise at the moment with the fabrication of Carbon Foam and will succeed in lowering the thermal impedance to, or even below, $5\ °Kcm^2/W$.

Q $[W]$	T_{sat} $[°C]$	$\dot{m}$ $[g/s]$	**G** $[kg/m^2]$	$\Delta\chi$	$\Delta_{\chi_D-\chi_{max}}$	$< h_{CO_2} >$ $[W/m^{2\circ}K]$	T_s $[°C]$ $R = 5$
200	-30	1.5	477.5	0.539	0.209	11895	-26.46
200	-30	2.0	636.6	0.430	0.235	12985	-26.61
200	-30	2.5	795.77	0.364	0.244	14042	-26.73
200	-30	3.0	954.9	0.320	0.161	15066	-26.83
200	-35	1.5	477.5	0.526	0.222	12294	-31.51
200	-35	2.0	636.6	0.419	0.230	13577	-31.68
200	-35	2.5	795.77	0.355	0.245	14814	-31.81
200	-35	3.0	954.9	0.313	0.253	16012	-31.92
200	-40	1.5	477.5	0.514	0.174	12787	-36.58
200	-40	2.0	636.6	0.410	0.230	14288	-36.76
200	-40	2.5	795.77	0.348	0.247	15722	-36.89
200	-40	3.0	954.9	0.307	0.248	17093	-37.00

Table 5.4: *Simulation results for the Outer Pixel stave. The sensor temperature has been calculated for different mass flows and saturation temperatures when CO_2 is used as refrigerant in a tube $D_i = 2$ mm at a heat flux of 200 W. Calculations have been done for the aimed value of the Carbon Foam's thermal impedance. It is assumed that the vapor quality at the inlet of the tube equals $\chi_{In} = 0.1$. $\Delta\chi$ is the vapor quality increase between χ_{in} and χ_{Out} (χ at the inlet and outlet of the tube, respectively), while $\Delta_{\chi_D-\chi_{max}}$ the remaining vapor quality between χ_{Out} and the vapor quality dry-out point.*

At nominal effective power CO_2 seems to be an excellent coolant. Under all situations is it capable of cooling the sensors below $-15\ °C$ without reaching the dry-out point.

Q $[W]$	T_{sat} $[°C]$	$\dot{m}$ $[g/s]$	**G** $[kg/m^2]$	$\Delta\chi$	$\Delta_{\chi_D-\chi_{max}}$	$< h_{CO_2} >$ $[W/m^{2\circ}K]$	T_s $[°C]$ $R = 5$
300	-30	1.5	477.5	0.782	-0.123	11354	–
300	-30	2.0	636.6	0.612	-0.013	15079	–
300	-30	2.5	795.77	0.509	0.040	16544	–
300	-30	3.0	954.9	0.441	0.065	17511	–
300	-35	1.5	477.5	0.759	-0.122	11461	–
300	-35	2.0	636.6	0.594	-0.019	15244	–
300	-35	2.5	795.77	0.495	0.028	17216	–
300	-35	3.0	954.9	0.430	0.051	18370	–
300	-40	1.5	477.5	0.7386	-0.128	11469	–
300	-40	2.0	636.6	0.579	-0.033	15184	–
300	-40	2.5	795.77	0.483	0.011	18014	–
300	-40	3.0	954.9	0.419	0.031	19340	–

Table 5.5: *Simulation results for the Outer Pixel stave. The sensor temperature has been calculated for different mass flows and saturation temperatures when CO_2 is used as refrigerant in a tube $D_i = 2$ mm at a heat flux of 300 W. Calculations have been done for the aimed value of the Carbon Foam's thermal impedance. It is assumed that the vapor quality at the inlet of the tube equals $\chi_{In} = 0.1$. $\Delta\chi$ is the vapor quality increase between χ_{in} and χ_{Out} (χ at the inlet and outlet of the tube, respectively), while $\Delta_{\chi_D-\chi_{max}}$ the remaining vapor quality between χ_{Out} and the vapor quality dry-out point.*

In Table 5.5 simulation concerning a tube of 2 *mm* under an effective power of 300 *W* are presented. There are now no possible situation to effectively cool the sensors without reaching dry-out in the tube. This is visualized in Figure 5.2 where the twelve heat transfer coefficient graphs are shown, with the two dots marking the inlet and outlet vapor quality.

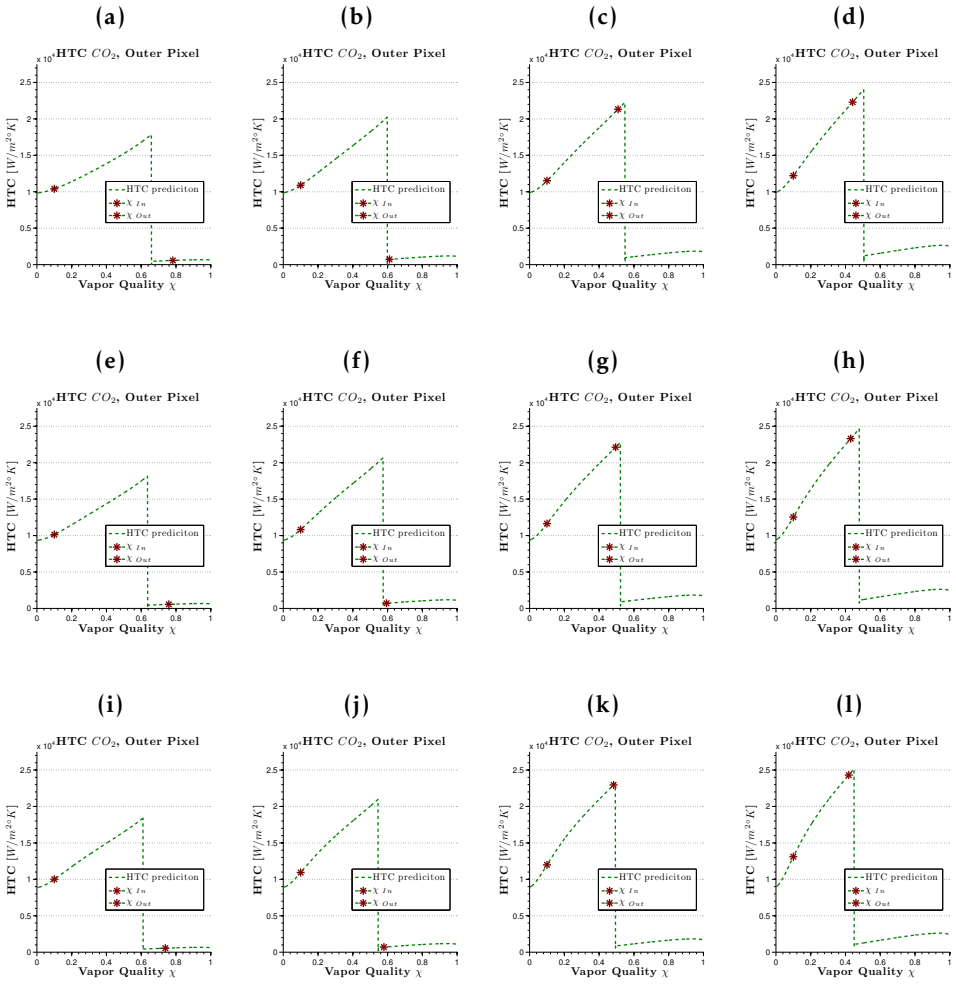

Figure 5.2: *Heat transfer coefficient graphs that correspond with Table 5.5. From top to bottom the temperature decreases in steps of* $-5\ °C$*, and from left to right the mass flow increases in steps of* $0.5\ g/s$*. The two dots represent the vapor quality at the inlet and outlet of the simulated stave.*

Because this tube size is not an option under the applied conditions the influence of a larger tube's diameter is investigated in Table 5.6 with $D_i = 2.5\ mm$.

Q $[W]$	T_{sat} $[°C]$	$\dot{m}$ $[g/s]$	**G** $[kg/m^2]$	$\Delta\chi$	$\Delta_{\chi_D-\chi_{max}}$	$< h_{CO_2} >$ $[W/m^{2\circ}K]$	T_s $[°C]$ $D_i = 2.5\ mm$
300	-30	1.5	477.5	0.782	-0.0290	10501	–
300	-30	2.0	636.6	0.612	0.101	11298	-25.1342
300	-30	2.5	795.77	0.509	0.167	11895	-25.25
300	-30	3.0	954.9	0.441	0.203	12496	-25.35
300	-35	1.5	477.5	0.759	-0.005	10767	–
300	-35	2.0	636.6	0.594	0.119	11452	-30.16
300	-35	2.5	795.77	0.495	0.180	12175	-30.30
300	-35	3.0	954.9	0.430	0.210	12905	-30.41
300	-40	1.5	477.5	0.7386	0.007	10895	–
300	-40	2.0	636.6	0.579	0.115	11706	-35.21
300	-40	2.5	795.77	0.483	0.168	12571	-35.36
300	-40	3.0	954.9	0.419	0.193	13424	-35.49

Table 5.6: *Simulation results for the Outer Pixel stave. The sensor temperature has been calculated for different mass flows and saturation temperatures when CO_2 is used as refrigerant in a tube $D_i = 2.5\ mm$ at a heat flux of $300\ W$. Calculations have been done for the aimed value of the Carbon Foam's thermal impedance. It is assumed that the vapor quality at the inlet of the tube equals 0.1, this the lowest quality were annular flow still can be assumed. $\Delta\chi$ is the vapor quality increase between χ_{in} and χ_{Out} (χ at the inlet and outlet of the tube, respectively), while $\Delta_{\chi_D-\chi_{max}}$ the remaining vapor quality between χ_{Out} and the vapor quality dry-out point.*

Hence, a tube with larger diameter could be a solution to the problem, although it is then a compromise between the used mass flow and the material needed for the tube. The same does not apply for smaller tubes, although the heat transfer coefficient then increases, the dry-out is reached in all situation, resulting in poor cooling performances.

6 Conclusions & Discussion

6.1 Conclusions

6.1.1 Blown system

The Blown System at SLAC that is used to characterize the heat transfer properties of CO2 has been improved. All the deficiencies of the system have been investigated and solved properly. The hardware and software used to take the data of the measurements has been simplified and upgraded: it is now possible to do repeatable measurements with more temperature sensors while connecting sensors has been simplified. An analyze program in Matlab has been developed that calculates the heat transfer coefficient from the data taken with the Labview data acquisition system and compares it with the analytic prediction models for CO_2. Beside the calculation of the CO_2 heat transfer coefficient a different program also has been written that analyzes the data concerning the thermal impedance of prototype staves.

6.1.2 Thermal impedance

The thermal impedance of the IBL prototype stave has been measured under different fluid temperatures using water as coolant. The result show that $R = 11.62\ ^\circ Kcm^2/W$, while the theoretical value calculated with finite element analysis is $R = 5\ ^\circ Kcm^2/W$. The discrepancy can be explained mainly by the defects introduced by the gluing process at the various interfaces; namely tube-foam and foam-sensor.

6.1.3 Heat transfer coefficient of CO_2

The heat transfer coefficient of CO_2 in bare, small diameter tube has been determined. The results show clear agreement with the CO_2 convection models from *Thome et al*. All the measurements taken with the SS RW-12, SS RW-14 and Ti RW-14 where dry-out has not been reached confirm the predictions within the margin of 30%.

The implications of the *Thome* model are:

1. Higher heat fluxes result in a higher average heat transfer coefficient, especially at low vapor quality the increase can be a factor of two. The maximum heat transfer coefficient, at point of dry-out, decreases while the point of dry-out is reached at a lower vapor quality.

2. Higher mass velocity results in a higher heat transfer coefficient, therefore the vapor quality at the outlet decreases. This is for a part com-

pensated because the dry-out point starts at a lower vapor quality. The maximum heat transfer coefficient is not influenced.

3. Lower evaporation temperature results in a higher heat transfer coefficient, without influencing the maximum coefficient and the start of the dry-out.

4. Thinner tubes result in a higher heat transfer coefficient for CO_2 compared with thicker tubes at the same mass flow, saturation temperature and applied heat flux.

The results taken with the SS Swagelok tube have a deviation with the predicted coefficient. This was hypothesized because the maximum mass velocity in the tube to reach full annular flow was not fulfilled. Because the shape of the data corresponds with the theoretical model and questions already arose concerning the measurement method, the theory is not contradicted by this data.

6.1.4 Temperature drop

The temperature drop measured for staves with a length of 1500 mm is 1.5 $°C$ when an effective power of 300 W is applied. This is half the value that is allowed. The pressure drop is largely responsible for the temperature gradient along tubes. The measurements show that the pressure drop over the tube can be up to 2 Bar when an effective power larger then 400 W is applied on a tube with $D_i = 1.6$ mm. This at the same time results in a temperature drop along the tubes, and thus staves. Moreover, there is an direct relation between the cross-section of the tube and the pressure tube. The SS Swagelok tube has a stable temperature profile along the stave. The SS RW-14 and Ti RW-14, which have the smallest cross-section have a the largest pressure drop over the tube and consequently the largest temperature gradient along the tube. As directive for the region -40 to -20 $°C$, the temperature drop is ~ 1 $°C\ Bar^{-1}$.

6.1.5 Staves for the phased upgrades

Phase I upgrade

The simulations that have been made based on the model by *Thome et al.* predict that when a tube of 2 mm is used for the phase I upgrade no problems should arise if $T_{sat} \leq -30$ $°C$ and $\dot{m} \geq 1.0$ g/s. Then a sensor temperature of -20 $°C$, or lower is to be guaranteed at all times.

Phase II upgrade

The simulation and measured data for the Outer Pixel show less promising results. When again a 2 mm tube is used, assuming the same sensor opera-

tion temperature, a power increase to 300 W (with safety factors), and the length of the tube becomes 1500 mm, the cooling performances of CO_2 are not adequate. The measurements show that dry-out arises before 300 W is applied on the tubes. To prevent dry-out in the tubes an option could be to increase the inner diameter of the tube to $D_i = 2.5\ mm$. Then, adequate cooling performances can be guaranteed if $T_{sat} \leq -30\ °C$ and $\dot{m} \geq 2.0\ g/s$ or better $\dot{m} \geq 2.5\ g/s$. Caution should be exercised because the cooling temperature that is reached is below $T_s = -25\ °C$, or even $T_s = -35\ °C$ in the case $T_{sat} = -40\ °C$. Depending on the operation region this could be too cold for the sensors and environment.

6.2 Discussion

6.2.1 Blown system

The limitations of the blown system become visible when the vapor quality becomes larger then the dry-out region. The heat transfer coefficient of CO_2 then reduces rapidly, as is predicted by the model. Consequently, the pre-cooling system stops working, because it uses the cold CO_2 to reduce the temperature of the warm CO_2 from the bottle, thus an increase of the inlet vapor quality is the result. The system then reaches a vicious circle and no stable equilibrium can be attained. Results where dry-out arose can therefore at the moment not be interpreted. When the pre-cooling would be accomplished by an external chiller this problem would be solved. Although already clear indications show that the model predicts the dry-out point correctly, the exact location of the dry-out point could then be determined.

A second limitation of the blown system is the maximum mass flow. This implies that larger tubes cannot be used in this blown system because the mass velocities are not sufficient to reach to right regions of flow. The problem arises because the CO_2 bottle of 50 pounds empties faster than reaching an equilibrium that would allow valid measurements.

Both problems could be solved by the development of a continuous system, which already have been started at SLAC. By placing an external chiller that allows cooling to $-40\ °C$ the influence of the pre-cooling with CO_2 is solved. Because in a continuous system the CO_2 is reused it does not matter how much CO_2 is used.

6.2.2 Heat transfer coefficient

The accuracy of with which the measurement has been carried out can be improved when better temperature sensors are used. The large systematic error of the sensors in combination with the used data acquisition system are responsible for most of the inaccuracies. Although calibration points

were available, making it possible to correct the measurements, it would be better if this was not necessary, because more accurate measurement can then be achieved.

Theoretically it is also possible to determine the heat transfer coefficient with the prototype stave when all the variables concerning the stave are known. This is the case when the thermal impedance is determined. This, however, did not allow to measure the heat transfer coefficient of CO_2 accurately enough. Because the temperature difference between fluid and inner tube wall is small and the corrections that have to be made from the measured temperature difference between the fluid and sensor that is placed on the dummy heater have relative large errors no acceptable results were measured. For example, it was obvious that the system was cooling the stave while a negative heat transfer coefficient was measured.

6.2.3 Simulations

The calculation concerning the simulation for the phased upgrade can be made more precise if the real values of the heat transfer coefficient are used. Furthermore, at the moment the calculation does not incorporate the pressure and thus pressure drop. A temperature drop of 1 $^{\circ}C$ leads to a slight increase in the heat transfer coefficient and thus increases the amount of heat that can be absorbed.

6.2.4 Recommendations

Further research

To confirm the model made by *Thome et al.* in all detail and to understand the behavior of CO_2 is small diameter tubes better, more research is needed. A larger database can be developed by variating the saturation temperature, mass velocities, heat fluxes, and, length and diameter of the tubes. A closed loop CO_2 system can accomplish this more accurately and in a shorter time span than a blown system, thus the developments of such a system is highly recommended. If such a system is available more parameters are interesting. The research could for example be focussed on the exact point of dry-out and the kind of flow inside the tubes at a certain mass velocity are interesting to know. Furthermore, when this cooling plant would be used to do research for large institutes as CERN it is recommended to change the sensors and read out system to that of those institutes to prevent later problems when data is compared and to increase the reliability of the measurements.

Detectors

R&D that focusses on the development of the detectors is of major importance. This possible could reduce the amount of power that has to be applied and therefore reduce cooling requirements. Then it could be possible to use the 2 *mm* tubes in the Outer Pixel staves as is preferred.

Infrared measurements show that dry-out is a dangerous situation that has to be taken into account. Would this happen in the detectors, then the reaction time to prevent serious damage is extremely short. Backup systems and fast safety electronics that can interrupt the power supply are therefore a necessity to limit accidents.

Prototypes

Only one prototype stave has been analyzed, which was also damaged. It is recommended that more staves will be analyzed to determine the thermal impedance and remaining characteristics of the improved carbon foam. Beside improving the foam, R&D concerning the glue process that attaches the tube, carbon foam and sensors to each other is highly recommended. Finally, it would be a good step when full length prototype staves with different inner diameters for the phase II upgrade would be developed. The simulation made in this thesis can then be validated and cooling performances could be optimized.

Bibliography

[1] (2010 May). CERN in a Nutshell. Retrieved May 28th 2010, from http://public.web.cern.ch/public/en/About/About-en.html.

[2] CERN-Press-office (2009 November 30th). LHC sets new world record. Retrieved June 8th, 2010, from http://press.web.cern.ch/press/PressReleases/Releases2009/PR18.09E.html.

[3] CERN-Press-office (2010 March 30th). LHC research programme gets underway. Retrieved May 29th, 2010, from http://press.web.cern.ch/press/PressReleases/Releases2010/PR07.10E.html.

[4] ATLAS-Collaboration (2010). ATLAS Fact Sheet. Technical report, CERN, Geneva. Retrieved May 26th, 2010, from http://www.atlas.ch/.

[5] Darbo, G. (2010 February). The ATLAS IBL project. Slides.

[6] Flick, T. (2009 September). IBL - ATLAS Pixel Upgrade. *Proceedings of Science*.

[7] Capeans, M., & Einsweiler, K. (2010 March 3th). ATLAS Insertable B-layer Technical Design Repor. *To be submitted to: LHCC*.

[8] Oriunno, M., Battistin, M., David, E., et al. (2007). Design and prototype studies of the TOTEM Roman pot detectors. *Nuclear Instruments and Methods in Physics Research A*, *581*, 499–503.

[9] Attree, D., & et al. (2008 July). The evaporative cooling system for the ATLAS inner detector. *Institute of Physics Publishing and Sissa*.

[10] Viehhauser, G. (2009). ATLAS upgrade ID cooling system requirements. Technical Report 3, ATU Thermal Management. ATLAS Tracker Upgrade (ATU).

[11] Verlaat, B. (2002). Feasibility Demonstration of a Mechanically Pumped Two-Phase CO2 Cooling Loop for the AMS-2 Tracker Experiment. *Conference on Thermophysics in Microgravity, in the Space Technology & Applications International Forum (STAIF-2002)*. Albuquerque, NM, USA.

[12] Verlaat, B. (2007). Controlling a 2-phase CO2 loop using a 2-phase accumulator. *International Congress of Refrigeration 2007*. Beijing.

[13] Cheng, L., Ribatski, G., Quibén, J. M., & Thome, J. R. (2008). New prediction methods for CO2 evaporation inside tubes: Part I – A two-phase flow pattern map and a flow pattern based phenomenological

model for two-phase flow frictional pressure drops. *International Journal of Heat and Mass Transfer*, (51), 111–124.

[14] Cheng, L., Ribatski, G., Quibén, J. M., & Thome, J. R. (2008). New prediction methods for CO2 evaporation inside tubes: Part II—An updated general flow boiling heat transfer model based on flow patterns. *International Journal of Heat and Mass Transfer*, (51), 125–135.

[15] Feld, L., Glessing, W., & Hammarström, R. (1998 February 23^{th}). Thermal Properties of the Silicon Microstrop Endcap Detector. *CMS Note*, *018*, 1–16.

[16] Pernegger, H. (2009). Sensor temperature and thermal run-away estimate IBL. Technical report, CERN.

[17] Kenney, C. (2006 April 5^{th}). Active Edge and 3D Sensors. International symposium on detector development, SLAC National Accelerator Laboratorium.

[18] Moser, H. (2002). SCT End-cap Module Components: Spines. Technical Report SCT-IS-EN-0009, CERN.

[19] Incropere, F., DeWitt, D., Bergman, T., & Lavine, A. (2007). *Fundamentals of Heat and Mass Transfer*. Hoboken, NJ: John Wiley and Sons, 6^{th} edition.

[20] Munson, B., Young, D., & Okiishi, T. (2006). *Fundamentals of Fluid Mechanics*. Hoboken, NJ: John Wiley and Sons, 5^{th} edition.

[21] Zürcher, O., Thome, J., & Favrat, D. (1999 February). Evaporation of Ammonia in a Smooth Horizontal Tube: Heat Transfer Measurements and Predictions. *Journal of Heat Transfer*, *Vol. 121*, 89–101.

[22] Kattan, N., Thome, J. R., & Favrat, D. (1998 February). Flow Boiling in Horizontal Tubes: Part 1 – Development of a Diabatic Two-Phase Flow Pattern Map. *Journal of Heat Transfer*, *Vol. 120*, 140–147.

[23] Kattan, N., Thome, J. R., & Favrat, D. (1998 February). Flow Boiling in Horizontal Tubes: Part 2 – New Heat Transfer Data for Five Refrigerants. *Journal of Heat Transfer*, *Vol. 120*, 148–155.

[24] Kattan, N., Thome, J. R., & Favrat, D. (1998 February). Flow Boiling in Horizontal Tubes: Part 3 – Development of a New Heat Transfer Model Based on Flow Pattern. *Journal of Heat Transfer*, *Vol. 120*, 156–165.

[25] Bejan, A., & Kraus, A. D. (2003). *Heat Transfer Handbook*. Chapter 9, Hoboken, NJ: John Wiley and Sons, 1^{st} edition.

[26] Wojtan, L., Ursenbacher, T., & Thome, J. R. (2005). Inverstigation of flow boiling in horizontal tubes: Part I–A new diabatic two-phase flow pattern map. *International Journal of Heat and Mass Transfer*, (48), 2955–2969.

[27] Fox, J. N. (1990). Temperature coefficient of resistance. *Phys. Educ*, *25*, 167–169.

[28] US_Secretary_of_Commerce (2008). NIST database. Retrieved between March and May 2010, from http://webbook.nist.gov/chemistry/fluid/.

[29] Deacon, C. G. (1992 Sept.). Error Analysis in the Introductory Physics Laboratory. *The Physics Teacher*, *30*, 368–370.

[30] de Wolf, E. (2009 September). Statistical Data Analysis. Printed.

[31] New England Small Tube. Http://www.nesmalltube.com/index.html. Litchfield Technology Park, 480 Charles Bancroft Hwy., Litchfield, NH 03052, U.S.A.

[32] Swagelok. Http://www.swagelok.com/default.aspx. Sunnyvale, CA 94089, 929 Weddell Court, U.S.A.

A Nomenclature

Normal

A = cross-sectional area, m^2
C_p = heat capacity, $J/kg°K$
D = tube diameter, m
f = volume flow, m^3/s
G = mass velocity, kg/sm^2
g = gravitational constant, m/s^2
h = heat transfer coefficient, $W/m^2°K$
I = current, A
l = length of tube, m
k = thermal conductivity, $W/m°K$
$\dot{m}$ = mass flow, kg/s
P = pressure, Pa
Q = power, W
q = power density, $q = Q/A$, W/m^2
R = thermal impedance, $°Kcm^2/W$
$R(T)$ = resistance, temperature dependent, Ω
r = radius, m
T = temperature, $°C$
U = voltage, V
w = width resistor, m
V = volume, m^3

Dimensionless Numbers

f = friction factor
Nu = Nusselt number $\left[\frac{0.23Re_D^{0.8}Pr^{0.3}k}{D_i}\right]$
Pr = Prandtl number $\left[C_p\mu/k\right]$
Re = Reynolds number $[4\dot{m}/\pi\mu D_i]$

Greek Symbols

α = temperature coefficient, $°K^{-1}$
κ = leakage current damage constant, A/cm
ρ = density, kg/m^3
σ = surface tension, N/m
Φ = particle fluence
μ = dynamic viscosity, $Pa \cdot s$
ν = kinematic viscosity, Ns/m^2
χ = vapor quality, %

Subscripts

CF = Carbon Foam
CO_2 = carbon dioxide
D = dimensionless
dep = depletion
f = fluid or coolant
i = inner
nom = nominal
max = maximum
o = outer
ref = reference
s = sensor
sat = saturation
Si = silicon
w = wall

B.1 Error propagation

When using multiple sensors to determine one specific value, error propagation is a necessary tool. The two subject that have been investigated in this thesis are the thermal impedance of Carbon Foam staves and the CO_2 heat transfer coefficient in small diameter tubes. Both values are measured indirectly as explained in chapter 3.

The GaussMarkov theorem, which is used in many textbooks and on universities [29][30], is presented in general form in Equation B.1. It is the bases of the error propagation used in this thesis calculations. Although the errors are systematic, this theory can be used because the results are calculated by combining a large number of variables that all have flat systematic errors. This result in a statistical prediction of the final value.

$$\sigma_f^2 = \sum_i \left(\frac{df(x_i)}{dx_i} \right)^2 \sigma_i^2 \tag{B.1}$$

B.2 Error overview

An overview of the sensors including there errors is presented in Table B.1, while other relevant errors are presented in Table B.2.

Sensors	Error
Absolute pressure sensors	±0.2% FS
Chiller	±0.1 °C
Flow meter	±0.10%
Gauge pressure sensors	< 0.7 bar: 0.15% FS, > 0.7 bar: 0.05% FS
Power supply (applying heat)	0.035% + 40 mV, 0.2% + 85 mA
Temperature sensors	$\pm(0.15 + 0.002T)$

Table B.1: *Overview of used electronic device that have relevant errors, with FS full scale and T the temperature* [°C].

Value	Error (σ^2)
Inner diameter tube (D_i)	$\sigma^2_{D_i} = (0.01 \cdot D_i)^2$
Length tube (L_t)	$\sigma^2_{L_t} = (0.01 \cdot L)^2$
Outer diameter tube (D_i)	$\sigma^2_{D_i} = (0.01 \cdot D_i)^2$
Resistance tube (R_{ohm})	$\sigma^2_{R_{ohm}} = (0.004 \cdot R_0)^2$
Width stave (W_t)	$\sigma^2_{W_t} = (0.01 \cdot W)^2$

Table B.2: *Overview of relevant errors.*

B.2.1 Thermal Impedance

To determine the error in the calculated thermal impedance R, first the errors in all the intermediate step have to be calculated. In this section this is done starting with the error calculation in the thermal impedance and ending with the known errors.

The error in the thermal impedance is formulated in Equation B.2,

$$\sigma_R^2 = \left(\frac{1}{q}\right)^2 \sigma_{\Delta T_{s-w}}^2 + \left(\frac{\Delta T_{s-w}}{q^2}\right)^2 \sigma_q^2 \tag{B.2}$$

with σ_q^2 as in Equation B.3 and $\sigma_{\Delta T_{s-w}}^2$ as in Equation B.4.

$$\sigma_{\Delta T_{s,w}}^2 = \sigma_{T_s}^2 + \sigma_{T_w}^2 + \sigma_{T_{fluid}}^2 \tag{B.3}$$

$$\sigma_q^2 = \left(\frac{1}{l \cdot w}\right)^2 \sigma_Q^2 + \left(\frac{Q}{l^2 \cdot w}\right)^2 \sigma_l^2 + \left(\frac{1}{l \cdot w^2}\right)^2 \sigma_w^2 \tag{B.4}$$

Here σ_Q^2 is formulated as Equation B.5.

$$\sigma_Q^2 = (2IR_{ohm})^2 \sigma_I^2 + \left(I^2\right)^2 \sigma_{R_{ohm}}^2 \tag{B.5}$$

B.2.2 Heat Transfer Coefficient

The error in the heat transfer coefficient is formulated in Equation B.6,

$$\sigma_h^2 = \left(\frac{1}{\pi D_i l \Delta T_{w,f}}\right)^2 \cdot \left[\sigma_Q^2 + \left(\frac{Q}{\Delta T_{w,f}}\right)^2 \sigma_{T_{w,f}}^2 + \left(\frac{Q}{D_i}\right)^2 \sigma_{D_i}^2 + \left(\frac{Q}{l}\right)^2 \sigma_l^2\right] \tag{B.6}$$

with σ_Q^2 as in Equation B.5, $\sigma_{D_1}^2$ and σ_l^2 as in Table B.2 and $\sigma_{\Delta T_{w,f}}^2$ as in Equation B.7.

$$\sigma_{\Delta T_{w,f}}^2 = \sigma_{T_s}^2 + \sigma_{T_{fluid}}^2 \tag{B.7}$$

B.2.3 Vapor Quality

The calculation of the error in the vapor quality is more extended than the two former ones, therefore only the final result is shown in Equation B.8.

$$\sigma_\chi^2 = \sigma_{\chi_{inlet}}^2 + \left(\frac{1}{\dot{m}}\right)^2 \sigma_Q^2 + \left(\frac{Q}{\dot{m}^2}\right)^2 \sigma_{\dot{m}}^2 \tag{B.8}$$

with $\sigma_{\chi_{inlet}}^2$ as in Equation B.9, σ_Q^2 as in Equation B.5 and $\sigma_{\dot{m}}^2$ as in Table B.1.

$$\sigma_{\chi_{in}}^2 = 2\left(\frac{1}{\Delta E}\right)^2 \sigma_{E_{in}}^2 + \left(\frac{E_{in} - E}{\Delta E^2}\right)^2 \sigma_{\Delta E}^2 \tag{B.9}$$

Here E the enthalpy $[kJ/m^2]$, ΔE the enthalpy difference between vapor quality 0 and 1, and E_{in} the corresponding value of enthalpy belonging to the vapor quality that enters the tube. The enthalpy is read out from the NIST database when the temperature and pressure of the fluid is known, therefore the errors are: $\sigma_{E_{in}}^2 \leq 2$ and $\sigma_{\Delta E}^2 \leq 4$.

C Overview measurements

This appendix presents the characteristics of the tubes that have been used to determine the heat transfer coefficient of CO_2. Furthermore, in section C.3 an overview of the used mass flow, saturation temperature and applied heat at which measurements have been taken place is presented.

C.1 Stave properties

Properties	IBL stave
Tube's material	Ti
Stave's material	Carbon Foam
Inner Diameter $[mm]$	2.0
Outer Diameter $[mm]$	2.2
Resistance $[\Omega]$	20.5
Length tube $[m]$	0.85
# Resistors	16
Length resistor $[m]$	0.04
Width resistor $[m]$	0.02
Thermal cond. $[Wm^{-1}\,{}^{\circ}K^{-1}]$	21.9
$\alpha\ [{}^{\circ}K^{-1}]$	$4.0 \cdot 10^{-3}$

Table C.1: *Characteristics of the IBL prototype stave.*

C.2 Tube properties

Properties	SS RW-12	SS RW-14	Ti RW-14	SS Swagelok
Inner Diameter $[mm]$	2.16	1.6	1.6	4.57
Outer Diameter $[mm]$	2.77	2.16	2.16	6.35
Resistance $[\Omega]$	0.479	0.799	0.602	0.119
Length tube $[m]$	1.525	1.525	1.524	1.550
Length resistor $[m]$	1.50	1.50	1.50	1.500
Therm. cond. $[Wm^{-1}\,{}^{\circ}K^{-1}]$	16.3	16.3	21.9	9.4
$\alpha\ [{}^{\circ}K^{-1}]$	$9.0 \cdot 10^{-4}$	$9.0 \cdot 10^{-4}$	$3.5 \cdot 10^{-3}$	$9.0 \cdot 10^{-4}$

Table C.2: *Characteristics of the tubes used to determine the heat transfer coefficient of CO_2. SS implies a stainless steel tube, while Ti means that the tube is made out of titanium. The first three tubes are order from New England Small Tube [31], while the last tube is order from Swagelok [32].*

C.3 Measurement Characteristics

C.3.1 SS RW-12

#	T_{sat} [°C]	**Mass flow** [g/s] (Massflux [kg/m^2s])	**Applied heat** [W]
1	−25	1.89 (515.78)	34.29, 77.18, 137.02, 173, 7, 177.23
2	−30	1.8 (518.51)	77.55, 137.82, 167.58, 309.6, 363.33, 420.38
3	−36	1.89 (491.22)	77.93, 138.31, 216.61, 261.55, 311.26
4	−18.5	1.5 (515.78)	76.43, 136.02
5	−28	1.35 (409.35)	53.26, 104.82, 172.92, 213.61, 257.83
6	−35	1.35 (368.41)	53.27, 105.52, 168.15, 215.11, 259.62
7	−26	1.35 (368.41)	52.82, 103.77, 163
8	−23	1.35 (368.41)	52.7, 103.85, 171.22, 211.49, 255.23
9	−42	1.5 (409.35)	53.95, 106.32, 175.27, 216.49

Table C.3: *Experimental values of the heat transfer coefficient measurements on the SS RW-12 tube. Values are the aimed saturation temperature, the average mass flow and the total applied heat.*

C.3.2 SS RW-14

#	T_{sat} [°C]	**Mass flow** [g/s] (Massflux [kg/m^2s])	**Applied heat** [W]
1	−35	1.6 (795.77)	83.65, 130.95, 188.26, 255.76, 334.1, 376.86
2	−18	1.25 (621.70)	46.05, 81.85, 128.19, 184.2, 250.34, 325.91
3	−25	1.5 (746.04)	46.65, 82.75, 129.56, 186.3, 253.31, 330.9
4	−30	1.45 (721.17)	46.6, 83.25, 130.32, 187.36, 254.71, 277.59
5	−35	1.0 (497.36)	83.75, 131.07, 187.96, 256.29, 333.3
6	−20	1.3 (646.57)	81.85, 128.44, 184.66, 250.86
7	−28	1.4 (696.30)	81.65, 129.44, 186.3, 253.14
8	44	1.0 (497.36)	47.55, 84.35, 131.95, 189.3, 257.3

Table C.4: *Experimental values of the heat transfer coefficient measurements on the SS RW-14 tube. Values are the aimed saturation temperature, the average mass flow and the total applied heat.*

C.3.3 Ti RW-14

#	T_{sat} $[°C]$	**Mass flow** $[g/s]$ (Massflux $[kg/m^2s]$)	**Applied heat** $[W]$
1	−26	2.0 (994.72)	82.08, 124.72, 185.5, 195.39
2	−30	1.3 (646.57)	70.73, 96.67, 126.12, 159.75, 183.97, 192.17
3	−25	1.55 (770.91)	69.08, 108.29, 155.59, 198.02
4	−30.4	1.55 (770.91)	70.58, 110.44, 158.97, 193.93

Table C.5: *Experimental values of the heat transfer coefficient measurements on the Ti RW-14 tube. Values are the aimed saturation temperature, the average mass flow and the total applied heat.*

C.3.4 Swagelok

#	T_{sat} $[°C]$	**Mass flow** $[g/s]$ (Massflux $[kg/m^2s]$)	**Applied heat** $[W]$
1	−32	4.0 (243.65)	95.37, 157.28, 234.38, 324.18
2	−28	2.4 (146.32)	94.98, 156.55, 233.07, 325.18

Table C.6: *Experimental values of the heat transfer coefficient measurements on the Swagelok tube. Values are the aimed saturation temperature, the average mass flow and the total applied heat.*

The DAQ for the setup is done with National Instruments devices and labVIEW software. A NI cDAQ 9172 with 8 slots is the main box, containing one NI 9205 unit and seven NI 9217 units. The former is used to read out the pressure sensors and mass flow, the latter is used to read out up to 28 temperature sensors.

D.1 NI device

In Figure D.1 the two blocks that are mounted in the NI cDAQ are shown including the connection scheme for the temperature sensors.

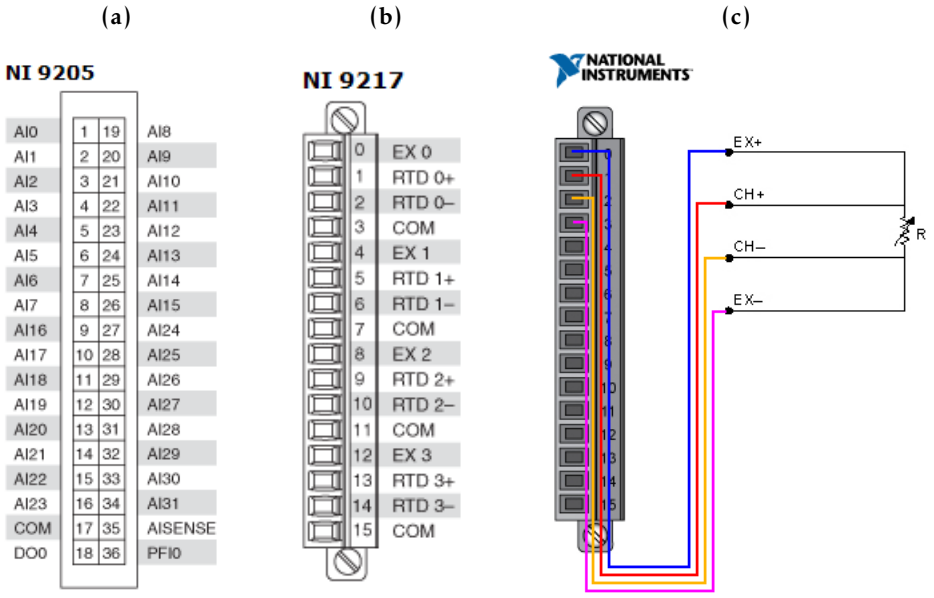

Figure D.1: *Labview blocks, NI 9205 and NI 9217, that are mounted in the NI cDAQ 9172. In D.1a and D.1b the pin numbering of the blocks are shown while in D.1c the 4–wire connection scheme for a temperature sensor is depicted.*

D.2 DAQ connections

In Table D.1 an overview of the connections is presented. It shows which sensors is connected to which connection point in the blocks. Furthermore, it contains the way the read-out is accomplished.

NI instr	NI Mod - CH	#	Sensor	Name	Type
NI 9205	I - ai0	0	Temperature [°C]	Mass/Flow	Current
NI 9205	I - ai1	1	Mass [g/s]	Mass/Flow	Current
NI 9205	I - ai2	2	Ground	Not in use	Voltage
NI 9205	I - ai3	3	Ground	Not in use	Voltage
NI 9205	I - ai4	4	Pressure [Bar]	Pre-Hexx	Current
NI 9205	I - ai5	5	Pressure [Bar]	Pre-Buck	Current
NI 9205	I - ai6	6	Humidity [%]	Voltage	Voltage
NI 9205	I - ai7	7	Pressure [Bar]	P in	Voltage
NI 9205	I - ai16	8	Pressure [Bar]	P out	Voltage
NI 9205	I - ai17	9	Ground	Not in use	Voltage
NI 9205	I - ai18	10	Ground	Not in use	Voltage
NI 9205	I - ai19	11	Not in use	Not in use	-
NI 9205	I - ai20	12	Not in use	Not in use	-
NI 9205	I - ai21	13	Not in use	Not in use	-
NI 9205	I - ai22	14	Not in use	Not in use	-
NI 9205	I - ai23	15	Not in use	Not in use	-
NI 9217	II - ai0:ai3	16	Temperature [°C]	T Ambient I	Voltage
NI 9217	II - ai4:ai7	17	Temperature [°C]	T Pre-Needle	Voltage
NI 9217	II - ai8:ai11	18	Temperature [°C]	T in	Voltage
NI 9217	II - ai12:ai15	19	Temperature [°C]	T out	Voltage
NI 9217	III - ai0:ai3	20	Temperature [°C]	T1	Voltage
NI 9217	III - ai4:ai7	21	Temperature [°C]	T2	Voltage
NI 9217	III - ai8:ai11	22	Temperature [°C]	T3	Voltage
NI 9217	III - ai12:ai15	23	Temperature [°C]	T4	Voltage
NI 9217	IV- ai0:ai3	24	Temperature [°C]	T5	Voltage
NI 9217	IV - ai4:ai7	25	Temperature [°C]	T6	Voltage
NI 9217	IV - ai8:ai11	26	Temperature [°C]	T7	Voltage
NI 9217	IV - ai12:ai15	27	Temperature [°C]	T8	Voltage
NI 9217	V - ai0:ai3	28	Temperature [°C]	T9	Voltage
NI 9217	V - ai4:ai7	29	Temperature [°C]	T10	Voltage
NI 9217	V - ai8:ai11	30	Temperature [°C]	T11	Voltage
NI 9217	V - ai12:ai15	31	Temperature [°C]	T12	Voltage
NI 9217	VI - ai0:ai3	32	Temperature [°C]	T13	Voltage
NI 9217	VI - ai4:ai7	33	Temperature [°C]	T14	Voltage
NI 9217	VI - ai8:ai11	34	Temperature [°C]	T15	Voltage
NI 9217	VI - ai12:ai15	35	Temperature [°C]	T16	Voltage
NI 9217	VII - ai0:ai3	36	Temperature [°C]	T17	Voltage
NI 9217	VII - ai4:ai7	37	Temperature [°C]	T18	Voltage
NI 9217	VII - ai8:ai11	38	Temperature [°C]	T19	Voltage
NI 9217	VII - ai12:ai15	39	Temperature [°C]	T20	Voltage
NI 9217	VIII - ai0:ai3	40	Temperature [°C]	T21	Voltage
NI 9217	VIII - ai4:ai7	41	Temperature [°C]	T22	Voltage
NI 9217	VIII - ai8:ai11	42	Temperature [°C]	T23	Voltage
NI 9217	VIII - ai12:ai15	43	Temperature [°C]	T24	Voltage

Table D.1: *Connection table with location and purpose of used sensors that are connected to the NI device and are read-out by the Labview program. (T means temperature sensor.)*

E MATLAB DAQ Program Manual

E.1 Adding a New Measurement

When a new file is recorded with Labview, open it with a plain text program like Notepad. Remove the header and save the file. Subsequently import the file in Excel and save it as a windows comma separated file (extension .csv). Save this file in the data map of MATLAB.

Depending if the new measurement has been done with water or CO_2 open: *water_info_tubes.m* or *co2_info_tubes.m*. For each tube there is a case which contains the specific data. Fill the file name of the new measurement in $files = \{\}$, use ' at the start and end of the file name. Furthermore, fill in all the details as inner tube diameter, outer tube diameter, location of the sensors (do not forget to includes the in and outlet sensors (they are placed at 0 and at the length of tube) and total resistance of the tube. Save the file and open *New_DAQ.m*. Run the file and follow the options in the terminal: Choose first which kind of analyze has to be done and secondly which tube/stave has to be used, the interface is shown in Listing E.1.

Listing E.1: *Interface Matlab program*

```
Which program do you want to run?
- 1 is Thermal Impedance (IBL stave)
- 2 is Thermal Impedance incl HTC (IBL stave)
- 3 is Bare stave water measurement
- 4 is Bare stave HTC
- 5 is HTC simulation
run program:

For which tube do you want this program to run?
- 1 is IBL stave
- 2 is LBNL stave
- 3 is SS RW-12 IBL
- 4 is SS RW-12 sHLC
- 5 is SS RW-14 IBL
- 6 is SS RW-14 sHLC
- 7 is Ti RW-14 IBL
- 8 is Ti RW-14 sHLC
- 9 is Swagelok 1/4"
Tube:
```

In this main file it is also possible to choose which graphs have to be shown or saved: 0 means no graphs, 1 show this graphs, 2 show and save the graphs, 3 save and close the graphs. To run a simulations of a certain tube the file: *co2_simulation_setup.m* has to be filled and option 5 has to

be chosen as program. Modifications to the graphs layout can be made in *set_graphs.m*.